UNIVERSITÀ
di VERONA

UNIVERSITY OF VERONA

DEPARTMENT OF COMPUTER SCIENCE

GRADUATE SCHOOL OF NATURAL SCIENCES AND ENGINEERING
DOCTORAL PROGRAM IN COMPUTER SCIENCE

Cycle XXXIII, 2017

Doctoral Thesis

Microstructure informed tractography with anatomical priors

S.S.D ING/INF-06

Verona, Italy, May 2021

Author:

Mario Alberto Ocampo Pineda

Certified by:

Prof. Alessandro Daducci
Thesis Tutor

Accepted by:

Prof. Massimo Merro
Chairman of the PhD School Council

Microstructure informed tractography with anatomical priors
Mario Alberto Ocampo Pineda
Ph.D. Thesis
Verona, Italy, date of submission to U-GOV University Research Catalogue
ISBN code

Abstract

It is known from brain anatomy that axons in the white matter are structured and organized in groups, called fascicles or bundles. Historically, these white matter structures have been studied in detail using invasive techniques, such as dissection, with the aim to elucidate their organization and possible effects of neurological diseases on brain connectivity. With the advent of magnetic resonance imaging, which is a noninvasive acquisition modality, today it is possible to perform "virtual dissections" using tractography. In fact, this technique allows estimating in vivo the macroscopic trajectory of these fascicles using 3D polylines called streamlines, and this unique ability opened a number of exciting possibilities to study the anatomy of the brain noninvasively and to characterize alteration in its structure due to pathology. However, tractography is not perfect and some limitations have recently been pointed out in many studies and received a lot of attention in the scientific community. One of the major problems is the high number of invalid white matter structures reconstructed, i.e., false-positive connections between cortical and subcortical regions, which were shown to potentially bias the characterization of brain connectivity.

The main objective of this thesis is to investigate and propose new strategies to improve the anatomical accuracy of tractography. In particular, we extended a microstructure informed tractography framework by introducing the important anatomical prior that axons are organized in groups and using this information as a constraint to reduce ambiguities in the reconstructions. We tested different solutions and showed that it is possible to improve the specificity of connectivity estimates without affecting their sensitivity, both in numerical simulations and real brain data. We implemented a pipeline using a supervised tractography segmentation tool to extract bundles and evaluate the performance of our proposals using in vivo data. In the first proposal, we introduced the possibility of using the definition of groups of streamlines as a constraint in the optimization problem, which produces a big improvement in the connectivity generated with the reconstructions. Later in the second strategy, we extended the framework to use as a constraint a multilevel hierarchical organization of streamlines, which is able to reproduce the connectivity results removing implausible streamlines that are inside the groups that create the connections. Finally, we proposed a robust augmentation to the cost function of the framework that adjusts for the reliability of the original measurements. With the research performed in

this thesis, we proved that adding information on the organization of the white matter benefits reconstructions made with tractography. Our proposals represent an additional step forward to improve the anatomical accuracy of tractography and our understanding of how different brain regions are interconnected.

Keywords: Tractography, white matter structure, hierarchical organization, microstructure informed tractography, Diffusion-Weighted Magnetic Resonance Imaging.

Sommario

È noto dall'anatomia cerebrale che gli assoni nella materia bianca sono strutturati e organizzati in gruppi, chiamati fascicoli o bundles. Storicamente, queste strutture di materia bianca sono state studiate in dettaglio utilizzando tecniche invasive, come la dissezione, con lo scopo di chiarirne organizzazione e possibili effetti delle malattie neurologiche sulla connettività cerebrale. Con l'avvento della risonanza magnetica, che è una modalità di acquisizione non invasiva, oggi è possibile eseguire "dissezioni virtuali" utilizzando la trattografia. Infatti, questa tecnica permette di stimare in vivo la traiettoria macroscopica di questi fascicoli utilizzando polilinee 3D chiamate streamlines, e questa capacità unica ha aperto una serie di interessanti possibilità per studiare l'anatomia del cervello in modo non invasivo e per caratterizzare l'alterazione nella sua struttura dovuta alla patologia. Tuttavia, la trattografia non è perfetta e alcuni limiti sono stati recentemente evidenziati in molti studi e hanno ricevuto molta attenzione da parte della comunità scientifica. Uno dei maggiori problemi è l'elevato numero di strutture di materia bianca non valide ricostruite, cioè connessioni false positive tra regioni corticali e sottocorticali, che hanno dimostrato di influenzare potenzialmente la caratterizzazione della connettività cerebrale.

L'obiettivo principale di questa tesi è di indagare e proporre nuove strategie per migliorare l'accuratezza anatomica della trattografia. Abbiamo esteso un framework di trattografia informata sulla microstruttura introducendo l'importante precedente anatomico che gli assoni siano organizzati in gruppi e utilizzando queste informazioni come un vincolo importante per ridurre le ambiguità nelle ricostruzioni. Abbiamo testato diverse soluzioni e dimostrato che è possibile migliorare la specificità delle stime di connettività senza influire sulla loro sensibilità, sia nelle simulazioni numeriche che nei dati del cervello reale. Abbiamo implementato una pipeline utilizzando uno strumento di segmentazione della trattografia supervisionato per estrarre i bundle e valutare le prestazioni delle nostre proposte utilizzando dati in vivo. Nella prima proposta, abbiamo introdotto la possibilità di utilizzare la definizione di gruppi di streamlines come vincoli nel problema di ottimizzazione, che produce un grande miglioramento nella connettività generata con le ricostruzioni. Successivamente, nella seconda strategia, abbiamo esteso il framework per utilizzare come vincoli un'organizzazione gerarchica a più livelli di streamline, che è in grado di riprodurre i risultati di connettività rimuovendo streamline non plausibili che sono all'interno dei gruppi che creanno le connezione. Infine,

abbiamo proposto un rafforzamento della funzione di costo del framework che si adegua all'affidabilità delle misurazioni originali. Con la ricerca svolta in questa tesi, abbiamo dimostrato che l'aggiunta di informazioni sull'organizzazione della sostanza bianca avvantaggia le ricostruzioni fatte con la trattografia. Le nostre proposte rappresentano un ulteriore passo avanti per migliorare l'accuratezza anatomica della trattografia e la nostra comprensione di come le diverse regioni del cervello sono interconnesse.

Parole chiave: Trattografia, struttura della materia bianca, organizzazione gerarchica, trattografia informata sulla microstruttura, risonanza magnetica pesata in diffusione.

Acronyms

ACT	Anatomically Constrained Tractography
AD	Axial Diffusivity
ADC	Apparent Diffusion Coefficient
CC	Corpus Callosum
CHARMED	Composite Hindered And Restricted Model Of Diffusion
COMMIT	Convex Optimization Microstructure Informed Tractography
CSF	Cerebrospinal Fluid
DODF	Diffusion Orientation Distribution Function
DPDF	Diffusion Probability Density Function
DSI	Diffusion Spectrum Imaging
DTI	Diffusion Tensor Imaging
DW-MRI	Diffusion-Weighted Magnetic Resonance Imaging
FA	Fractional Anisotropy
FACT	Fiber Assignment By Continuous Tracking
FAST	FMRIB's Automated Segmentation Tool
FISTA	Fast Iterative Shrinkage-Thresholding Algorithm
FODF	Fiber Orientation Distribution Function
GM	Gray Matter
HARDI	High Angular Resolution Diffusion Imaging
HCP	Human Connectome Project
IASF	Intra-axonal Signal Fraction
IB	Invalid Bundles
IC	Invalid Connections
LiFE	Linear Fascicle Evaluation
MD	Mean Diffusivity
MRI	Magnetic Resonance Imaging
NMR	Nuclear Magnetic Resonance
NNLS	Non-negative Least Squares
NODDI	Neurite Orientation Dispersion And Density Imaging
ODF	Orientation Distribution Function
PDD	Primary Diffusion Direction

PGSE	Pulse Gradient Spin Echo
RD	Radial Diffusivity
RF	Radio Frequency
RMSE	Root Mean Square Error
ROI	Region Of Interest
SCIL	Sherbrooke Connectivity Imaging Laboratory
SH	Spherical Harmonics
SIFT	Spherical-deconvolution Informed Filtering Of Tractograms
SLF	Superior Longitudinal Fasciculus
SLR	Streamline-based Linear Registration
SMT	Spherical Mean Technique
SNR	Signal To Noise Ratio
TE	Echo Time
VB	Valid Bundles
VC	Valid Connections
WM	White Matter

Contents

Acronyms **7**

1 Introduction **17**

2 Background **23**

2.1 The human brain and neural tissue 23

2.2 Measuring water diffusion in the human brain 26

2.2.1 Signal acquisition 28

2.2.2 Modeling diffusion in the brain 34

2.3 Microstructure models 43

2.3.1 Multi-Gaussian model 43

2.3.2 Ball and stick model 44

2.3.3 Neurite orientation dispersion and density imaging . . . 45

2.3.4 Multi-compartment microscopic diffusion model based on the Spherical Mean Technique 47

2.4 Tractography 49

2.4.1 Local tracking 50

2.4.2 Global tracking 52

2.4.3 Limitations of tractography 55

2.5 Microstructure informed tractography 57

2.5.1 Spherical-deconvolution Informed Filtering of Tractograms 58

2.5.2 Linear Fascicle Evaluation 64

2.5.3 Convex Optimization Modeling for Microstructure Informed Tractography 65

2.6 Comprehensive map of neural connections in the brain 68

3 In vivo tractography evaluation methodology **73**

3.1 RecobundlesX 74

3.2 Creation of true- and false-positive bundle models 76

3.3 Bundle segmentation 81

4 Injecting priors about brain anatomy and its organization 91
4.1 Materials and methods . . . 91
4.1.1 Synthetic phantom description and processing . . . 93
4.1.2 Evaluation criteria . . . 95
4.1.3 In vivo data processing . . . 97
4.2 Results . . . 98
4.2.1 Optimization of the regularization parameter . . . 98
4.2.2 Sensitivity and specificity of the new formulation on simulated data . . . 99
4.2.3 Comparison to state-of-the-art filtering techniques . . . 100
4.2.4 Comparison to other basic filtering procedures . . . 102
4.2.5 Qualitative evaluation on in vivo human brain data . . . 103
4.3 Discussion . . . 105

5 Refinement based on the hierarchical organization of fibers 111
5.1 Materials and methods . . . 112
5.1.1 Illustrative toy example. . . . 113
5.1.2 Data and experiments . . . 115
5.2 Results . . . 116
5.2.1 Quantitative evaluation on synthetic data . . . 116
5.2.2 Qualitative evaluation on in vivo data . . . 117
5.3 Discussion . . . 124

6 Outlier adjusted tractogram weighting 129
6.1 Materials and Methods . . . 130
6.1.1 Weighted minimization . . . 130
6.1.2 Data and experiments . . . 132
6.2 Results and discussion . . . 133

7 Conclusion 137

List of Figures

2.1 Gray and white matter of the brain 24
2.2 Structure of a Neuron 25
2.3 Lobes of the brain 26
2.4 Association, commissural, and projection white matter fibers . . 27
2.5 Scheme of a spin 29
2.6 Example of a T1-weighted MRI 32
2.7 Scheme of the Pulse Gradient Spin Echo sequence 33
2.8 Example of DW-MRI 35
2.9 Tensors as ellipsoids 38
2.10 Examples of q-space sampling 39
2.11 Visual representation of real spherical harmonics 40
2.12 Examples of fODFs 42
2.13 Streamlines generated with local tractography algorithms 53
2.14 Example of the filtering performed by the SIFT algorithm on synthetic data 61
2.15 Comparison of the filtering performed by the SIFT2 and SIFT algorithms on in vivo data 64
2.16 Example to illustrate the COMMIT framework 69
2.17 Workflow to map the structural connectivity of the brain 71

3.1 Bundle models used as true-positive models, association fibers . 77
3.2 Bundle models used as true-positive models, commissural fibers 78
3.3 Bundle models used as true-positive models, projection fibers . . 79
3.4 Process to create a false-positive bundle model 79
3.5 Bundle models used as false-positive models 80
3.6 True-positive bundles segmented with RecobundlesX 86
3.7 False-positive bundles segmented with RecobundlesX 87
3.8 Connectome comparison: Raw tractogram, and segmented true- and false-positive bundles 89

3.9 Binary operations of connectomes created with segmented true- and false-positive bundles 90

4.1 Injecting priors about brain anatomy and its organization. . . . 93
4.2 Quantitative evaluation of the proposed method 94
4.3 Sensitivity and specificity of the connectomes in two phantoms . 96
4.4 Impact of adding the bundle-wise anatomical priors to COMMIT on the quality of the reconstructions. 99
4.5 Comparison with state-of-the-art filtering techniques 101
4.6 Comparison with basic filtering procedures 104
4.7 Effect of thresholding on the estimated connectomes 105
4.8 Qualitative evaluation of the proposed method with in vivo data 106
4.9 Comparison of connectomes estimated on the HCP data 107

5.1 Possible improvement over the COMMIT2 formulation 112
5.2 Visual comparison between the COMMIT, COMMIT2, and COMMIT2$_{\text{tree}}$ formulations 114
5.3 Illustrative toy example of the COMMIT2$_{\text{tree}}$ formulation 116
5.4 Quantitative comparison on synthetic data between COMMIT2 and COMMIT2$_{\text{tree}}$ 118
5.5 Impact of the distance metric on the quality of the tractograms filtered with COMMIT2$_{\text{tree}}$ 119
5.6 True- and false-positive bundles estimated in one HCP subject, comparison between COMMIT2 and COMMIT2$_{\text{tree}}$ 121
5.7 Visual inspection of two representative bundles across the ten HCP subjects 123
5.8 Connectomes estimated in one HCP subject, comparison between COMMIT2 and COMMIT2$_{\text{tree}}$ 124
5.9 Impact of the group size on the quality of the tractograms filtered with COMMIT2$_{\text{tree}}$ 128

6.1 Description of the synthetic fiber phantom 131
6.2 Streamline contributions in the numerical simulations 133
6.3 Whole-brain RMSE evaluation of the HCP subject 134
6.4 Whole-brain intra-axonal and isotropic signal fraction evaluation of the HCP subject 135

List of Tables

2.1 Comparison of a T1-weighted and T2-weighted image 31

3.1 Names of the bundle models used as true positives 83
3.2 Parameter configuration used in RecobundlesX per bundle of panel a) 84
3.3 Parameter configuration used in RecobundlesX per bundle of panel b) 85

5.1 Stability across the ten HCP subjects 120
5.2 Quantitative comparison across the ten HCP subjects of the sub-bundles presented in Figure 5.7 122

Publications

Journal papers

- Ocampo-Pineda, M., Schiavi, S., Rheault, F., Girard, G., Petit, L.,Descoteaux, M., and Daducci, A. (2021). Hierarchical Microstructure Informed Tractography. Brain Connectivity

- Schiavi, S., Ocampo-Pineda, M., Barakovic, M., Petit, L., Descoteaux, M., Thiran, J.-P., and Daducci, A. (2020). A new method for accurate in vivo mapping of human brain connections using microstructural and anatomical information. Science Advances, 6(31).

- Schilling, K. G., Nath, V., Hansen, C., Parvathaneni, P., Blaber, J., Gao, Y., Neher, P., Aydogan, D. B., Shi, Y., Ocampo-Pineda, M., Schiavi, S., Daducci, A., Girard, G., Barakovic, M., Rafael-Patino, J., Romascano, D., Rensonnet, G., Pizzolato, M., et al. (2019). Limits to anatomical accuracy of diffusion tractography using modern approaches. NeuroImage, 185:1 – 11.

- Schilling, K. G., Rheault, F., Petit, L., Hansen, C. B., Nath, V., Yeh, F.-C.,Girard, G., Barakovic, M., Rafael-Patino, J., Yu, T., Fischi-Gomez, E., Pizzolato,M., Ocampo-Pineda, M., Schiavi, S., Canales-Rodríguez, E. J., Daducci, A.,Granziera, C., et al. (2020). Tractography dissection variability: what happenswhen 42 groups dissect 14 white matter bundles on the same dataset? NeuroImage, 243:118502.

Proceedings

- Battocchio, M., Girard, G., Barakovic, M., Ocampo, M., Thiran, J.-P., Schiavi, S., and Daducci, A. Improving graph-based tractography plausibility using microstructure information. Computational Diffusion MRI. MICCAI 2019. Mathematics and Visualization. Springer, Cham. https://doi.org/10.1007/978-3-030-05831-9_29

- Hernandez-Gutierrez, E., Ramirez-Manzanares, A., Marroquin, J. L., Ocampo-Pineda, M., and Daducci, A. (2019). Cuda Parallelization of COMMIT Framework for Efficient Microstructure-Informed Tractography. In 2019 IEEE 16th International Symposium on Biomedical Imaging (ISBI 2019), pages 1606–1609.

Posters and presentations

- SANDI-AMICO: an open-source toolbox for fast Soma And Neurite Density Imaging (SANDI) with AMICO. Accepted for a poster presentation during the 2021 OHBM Annual Meeting. Palombo et al.

- Cleaning up tractography, driven by microstructure and hierarchical white matter structures. Poster. XI congresso Associazione Italiana di Risonanza Magnetica in Medicina (AIRMM), 2020. ISMRM Italian Chapter. Ocampo-Pineda et al.

- Is it feasible to directly access the bundle's specific myelin content, instead of averaging? A study with Microstructure Informed Tractography. Poster. International Society for Magnetic Resonance in Medicine (ISMRM) 27th Annual Meeting, 2019. Schiavi et al.

- Reducing false-positive connections using hierarchical microstructure informed tractography. Poster. International Society for Magnetic Resonance in Medicine (ISMRM) 27th Annual Meeting, 2019. Ocampo-Pineda et al.

- Reducing false-positive connections using hierarchical microstructure informed tractography. Presentation. SCIL/ISMRM workshop, 2019.

- Quantifying diameter overestimation of undulating axons from synthetic DW-MRI. Power Pitch. International Society for Magnetic Resonance in Medicine (ISMRM) 26th Annual Meeting, 2018. Ramirez-Manzanares et al.

- Tackling false positives in tractography with convex optimization and anatomical priors. Poster. Data Science Summer School (DS3) 2018.

Training

- Participation in: Brainhack Micro2Macro 2021. Project: Implementation of soma and neurite density imaging (SANDI) in the accelerated microstructure imaging via convex optimization (AMICO) framework.

- Internship as visiting PhD student at the Sherbrooke Connectivity Imaging Laboratory (SCIL) in the Computer Science Department of the Science Faculty of University of Sherbrooke from January to May 2019.

- Participation in: 3-D Validation of Tractography with Experimental MRI (3D VoTEM) ISBI 2018 Challenge. First Place in the Macaque Validation Challenge.

Chapter 1

Introduction

Currently is possible to study the white matter (WM) of the brain, in vivo and in a noninvasive way, mapping it to 3D reconstructions called tractography (Mori et al., 1999; Conturo et al., 1999; Jones et al., 1999; Basser et al., 2000; Poupon et al., 2000). Unfortunately, these representations are not perfect, and in most cases have poor anatomical accuracy and contain spurious elements (Thomas et al., 2014; Maier-Hein et al., 2017). In this work we propose strategies, considering information from the tissue microstructure and structural organization of the WM, to remove wrong elements and improve the quality of tractography. These reconstructions, also known as tractograms, can map and represent WM tissue that is formed mostly by axons, which are fiber structures surrounded by layers of myelin that run or cross all the brain. The reconstructions have been used to perform virtual in vivo dissections of WM (Catani et al., 2002), surgical planning (Essayed et al., 2017), to study potential alterations due to neurodegenerative diseases (Jeurissen et al., 2017; Yeh et al., 2020), or to describe and investigate the structural connectivity of the brain (Hagmann, 2005; Sporns et al., 2005) and alterations of this due to neurological conditions (Griffa et al., 2013). Due to these relevant applications, it is important to generate the best possible reconstructions.

Diffusion-Weighted Magnetic Resonance Imaging (DW-MRI) is a noninvasive technique used to study the brain and obtain information required to perform tractography (Stejskal and Tanner, 1965; Basser et al., 1994b). DW-MRI is able to measure the diffusion or displacement of the water molecules. This information can be used to infer structural properties of the tissue (Panagiotaki et al., 2012; Novikov et al., 2019; Alexander et al., 2019), in the case of the axons it is possible to infer the orientation of groups of axons (Basser and Pierpaoli, 1996). Tractography algorithms

use and follow these orientation descriptions to create long pathways called streamlines (see review in (Jeurissen et al., 2017)) that should be associated with a group of axons and not a single fiber (Jones et al., 2013; Schiavi et al., 2020). The streamlines can be grouped in bundles that represent WM fascicles (Mandonnet et al., 2018), which are groups of axons that run from one region of the brain to another defining WM structures.

Despite the opportunities the application of DW-MRI and tractography can provide, these have limitations (Thomas et al., 2014). The image generation is contaminated with noise and artifacts and there are restrictions in the resolution of the images that can be achieved with the actual hardware. Besides technical restrictions, the exposition to high magnetic fields can cause pain and discomfort, and an excess amount of radio-frequency radiation can cause thermal effects (burns) and harm the subjects (Formica and Silvestri, 2004; Sammet, 2016; Tsai et al., 2015). Tractography by itself is limited as the problem that is trying to solve is an ill-posed problem because multiple solutions can be obtained from the actual data sets (Jeurissen et al., 2017). Another limitation is that up to now, there is no ground truth to validate the reconstructions of an in vivo acquisition (Dyrby et al., 2007; Côté et al., 2013). This research area is quite recent, in the last 20 years has improved significantly and there is a big effort to continue improving it (Wende et al., 2020). During this time, different studies have been performed to validated and evaluate tractography (Thomas et al., 2014; Drakesmith et al., 2015; Zalesky et al., 2016; Maier-Hein et al., 2017; Schilling et al., 2019; Girard et al., 2020; Rheault et al., 2020b). These works have confirmed advantages and potential of different tractography approaches, as well, their anatomical inaccuracies and limitations. It is clear that there is no tractography algorithm that can produce perfect reconstructions for different scenarios, but advantages and disadvantages, limitations, and strengths of different algorithms have been identified (Jeurissen et al., 2017). This allows generating specific reconstructions for the type of problem to be solved or available data, knowing or having an idea in advance of the possible problems that the reconstructions can have (Thomas et al., 2014).

One of the major problems that all the tractography algorithms present are the false-positive streamlines, it has been shown that all tractography algorithms reconstruct a high number of those (Drakesmith et al., 2015; Girard et al., 2020; Maier-Hein et al., 2017; Rheault, 2020; Schilling et al., 2019; Thomas et al., 2014; Zalesky et al., 2016). These streamlines have

implausible trajectories and can create implausible connections. These wrong representations bias the studies performed with the tractography reconstructions, and it has been investigated the negative effect of these wrong connections in connectivity studies (Zalesky et al., 2016). This is the problem that is addressed in this work, where we have developed strategies that remove invalid streamlines from tractography reconstructions. We combined microstructural information and anatomical priors using a microstructural informed tractography framework to improve tractography reconstructions.

Microstructural informed tractography is a research area that links tractography and microstructural properties (Kreher et al., 2008; Sherbondy et al., 2009; Daducci et al., 2016) to enhance the reconstructions. The idea is to create tractography reconstructions that not only are according to local diffusion orientations inside each voxel but also to structural properties, such that the signal volume fraction that corresponds to WM (Kaden et al., 2016a; Zhang et al., 2012; Panagiotaki et al., 2012). In most cases this type of algorithm follows a global approach (Reisert et al., 2011, 2014; Konopleva et al., 2018; Kreher et al., 2008; Christiaens et al., 2015; Mangin et al., 2013), that is, they try to reproduce the whole signal and create or select all the streamlines at the same time, which requires high computational resources. It is possible to identify two main approaches to apply, a bottom-up and a top-down approach. The first one starts with small segments of the streamlines distributed in the WM volume, that are changed, e.g., rotated, translated, and elongated, in such a way that in combination with signal models they reproduce the observed signal, at the same time the segments are linked together to create the pathways that cross the brain (Reisert et al., 2011; Konopleva et al., 2018), this type of algorithms are especially computationally demanding because the high number of segments and variables to use. The second type takes as input tractography reconstructions, which can be created with a fast and non computationally demanding procedure, like local tracking, but that is susceptible to inaccuracies in the local modeling (Jeurissen et al., 2017). In the optimization process, it tries to identify the subset of streamlines that best describes the observed data. Some algorithms try to remove redundant streamlines and those that do not reproduce the signal properly along all its trajectory (Smith et al., 2013) and others also assign a contribution of each streamline to the observed data (Smith et al., 2015a; Pestilli et al., 2014; Daducci et al., 2013, 2015; Schiavi et al., 2020; Ocampo-Pineda et al., 2021).

Nowadays, there are different algorithms that use the top-down approach

designed to assign streamline contribution or removing redundant streamlines, but ineffective in removing invalid connections or invalid bundles in the reconstructions, as they were not designed for this purpose (Schiavi et al., 2020). We extended the Convex Optimization Microstructure Informed Tractography (COMMIT) framework (Daducci et al., 2013, 2015) to remove bundles of invalid streamlines. We decided to work with this framework because it has effectively simplified the tractography problem in a linear formulation, which is possible to extend and improve. The observed signal is explained by the weighted sum of elements of a matrix, that is formed by combining streamlines and signal forward models. The problem is efficiently solved using a non-negative least squares approach that allows the incorporation of information about the reliability of the data and regularization terms that constrain and stabilize the problem in such a way it is possible to find a unique solution to the ill-posed problem (Daducci et al., 2015).

We designed and added a regularization term to the COMMIT formulation that incorporates information about the structural organization of the streamlines and allows the effective removal of groups of implausible streamlines. Our hypothesis is that the axons are likely organized in groups (Udin and Fawcett, 1988), this organization can be reproduced by the streamlines, which are grouped to represent bundles that can be valid or invalid. It has been shown that the invalid streamlines also form dense and structured bundles (Maier-Hein et al., 2017). We used groups of streamlines as restrictions in the linear model, the definition of the groups can be done in different ways, we focused on two and proposed two strategies to use this regularization term. In the first strategy, the streamlines are grouped based on the endpoints and the cortical and subcortical regions their intersect, i.e. all the streamlines that connect the same pair of cortical regions were assigned to a group, as in a connectome (Hagmann, 2005; Sporns et al., 2005), this strategy was focused on improving the connectivity maps reconstructed from the tractograms. In the second strategy, the groups were divided into subgroups using a clustering strategy based on the trajectory of the streamlines (Garyfallidis et al., 2012) and were added as a second level in a hierarchical structure, this strategy adds information about the geometry of the streamlines, complementing the connectivity information to further improve the tractograms, removing groups of implausible streamlines inside bundles that form valid connections.

We used a synthetic phantom and in vivo data to test the strategies

developed. The phantom mimics WM configurations found in a real brain, like bending and crossing of fibers (Caruyer et al., 2014). Of this one, we know the ground-truth tractography and connectivity map. We used the Human Connectome Project (HCP) in vivo data (Essen et al., 2013) to test our proposals. To evaluate the generated reconstructions we decided to use a method that automatically segments bundles using models as reference (Garyfallidis et al., 2018; Rheault, 2020). The models correspond to known valid bundles and some implausible bundles that have been found in tractography reconstructions (Maier-Hein et al., 2017). The results indicated that the implemented strategies improve tractography reconstructions by removing false-positive streamlines. On the synthetic phantom, more than 90% of invalid connections were removed without affecting the valid connections, e.g., for a probabilistic tractography that reconstructed 441 invalid connections, after filtering we kept 15. This result overcame the original formulation that was able to remove only the 10% of invalid connections, keeping 393. On in vivo data, by using the proposed strategies the implausible bundles were reduced and in some cases completely removed, and the valid bundles were not considerably affected, e.g., their volume after filtering was in the range of 50% and 90% of the volume of the raw tractogram. As it has been investigated, the microstructure informed tractography is able to remove ambiguity in the reconstructions and add quantitative meaning to the streamlines (weight or contribution) (Daducci et al., 2015, 2016). With our results, we proved that considering the structural organization of WM allows our method to remove groups of implausible streamlines, which will help to describe more accurately the WM structures of each person.

We proposed a robust augmentation to the cost function used in COMMIT that adjusts for the reliability of the original measurements. The COMMIT framework estimates a contribution of each streamline to a predicted signal. Contributions are iteratively updated based on a chosen cost function until implausible streamlines are filtered out and the algorithm converges to a prediction that is the closest to the original measurements by minimizing the root mean square error (RMSE). If the contribution of a streamline becomes zero, the corresponding streamline will be rejected as not compatible with the measured signal. Minimization approaches based on RMSE are suited only for voxels that can be correctly described by the chosen microstructural model. If a streamline traverses a voxel that partially or fully consists of gray matter (GM) or data is partially unreliable, the microstructural model for WM would

be incorrect to predict the corresponding signal in that voxel. This would cause the algorithm to converge to an incorrect solution as GM contamination is not directly modeled. The reliability can be estimated with respect to the microstructural model used or to the overall quality of the data which could be decreased by outliers or artifacts (Sairanen et al., 2018).

This thesis presents in Chapter 2 the context and motivation of this work, basic concepts about the brain and its anatomy, DW-MRI, and tractography, the limitations and current strategies to improve it. Chapter 3 describes the method used to qualitative and quantitative evaluate the tractography reconstructions of in vivo data sets. In Chapter 4, the first strategy proposed is presented, where groups of streamlines are introduced in the COMMIT formulation to filter out streamlines that create invalid connections in the connectivity matrix. In Chapter 5 the second strategy is described, where a multilevel hierarchical structure is used to add more information about the structural organization of the streamlines, to remove groups of implausible streamlines inside bundles that are part of valid connections. In Chapter 6 we described our proposed cost function that is robust to unreliable measurements. And Chapter 7 contains a summary of the work presented, the discussion about the obtained results, and the possible future work.

Chapter 2

Background

2.1 The human brain and neural tissue

The human brain is the main element of the central nervous system, it is in charge of controlling and directing the actions and functions of the body and it is one of the most complex and efficient structures in the universe (Hofman, 2014). It controls our behavior, processes the stimuli we receive from outside transforming them into sensations, generates our movements, thoughts and allows us to communicate and interact with our surroundings, it is the center of our abilities and intelligence (Colom et al., 2010). It has been studied for many years (Wickens, 2014), and although recently a great advance has been made in its understanding and the scientific community has a better idea of how it works, there are still many aspects about it which we do not know or understand (Lam, 2016; Tompa, 2019), but with the advances of new technologies and methods, we will be able to describe them (Fan, 2021).

Broadly speaking, the brain consists of two hemispheres which have gray and white matter tissue, see Figure 2.1. The gray matter, located in the outer layer, also called the cortex, and in the inner part, called nucleus or subcortical regions. The gray matter receives and processes the visual, somatosensory, auditory, gustatory, and olfactory information, enables the control of the movement, memory, and emotions (Mercadante and Tadi., 2020). This information travels through the white matter that connects different brain regions (Fields, 2010).

The brain is made up of different types of cells and tissues, one of those cells is the neurons. There are around 100 billion neurons and each one of them can communicate with thousands of other cells through electrical impulses (Lovinger, 2008). Most neurons are made up of a cell body, dendrites,

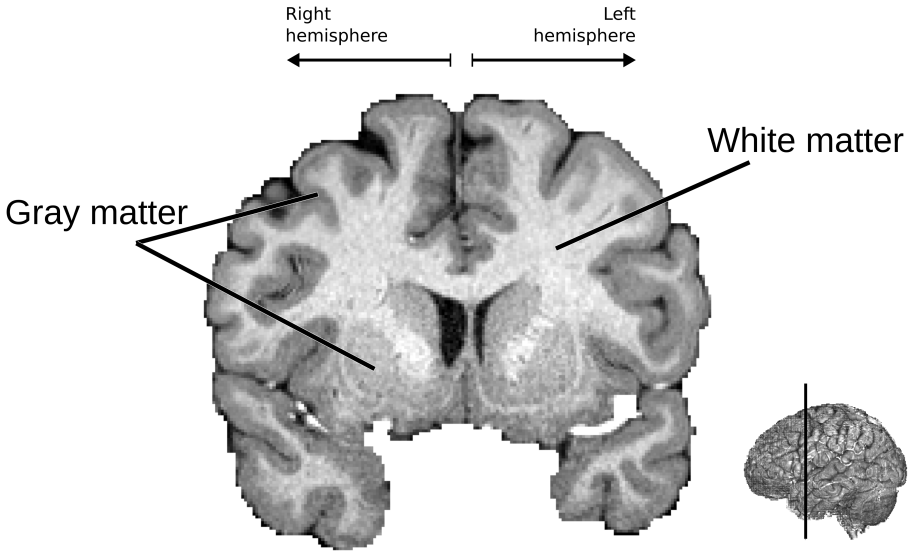

Figure 2.1: **Gray and white matter of the brain.** Coronal cross-section of a T1-weighted MRI of a human brain showing white and gray matter areas.

and an axon, a representative drawing is presented in Figure 2.2. Dendrites have the function of receiving neuronal signals and axons are in charge of transmitting these impulses to other neurons in different parts of the brain or body (Rockland, 2002). Axons can be described as micro-tubes covered by fat myelinated Schwann cells, in charge of maintaining and keeping the axon in good condition. The axons are grouped into tracts or bundles of fibers and connect different regions of the cortex, the fat that covers them gives them the white appearance. The cortex is formed by folds or undulations called gyri surrounded by sulci. The cortex of the hemispheres can be divided into four parts called lobes: frontal, parietal, temporal, and occipital (Gray and Lewis, 1918), see Figure 2.3.

Different bundles of white matter fibers have been identified and classified. One of these bundle classifications is based on the connections formed, having the types commissural, association, and projection, Figure 2.4 displays an illustration of this classification. The commissural fibers connect one hemisphere with the other, the bundles pass through the commissure regions, like corpus callosum; association tracts connect different regions within the same hemisphere, connecting different gyri within a single lobe or different lobes; and projection tracts are fibers that run from the cortex to the internal gray matter regions. Specific bundles of fibers have been identified and named depending on the regions they connect and the trajectory that they describe (Martino and Brogna, 2011; Wycoco et al., 2013). Examples of

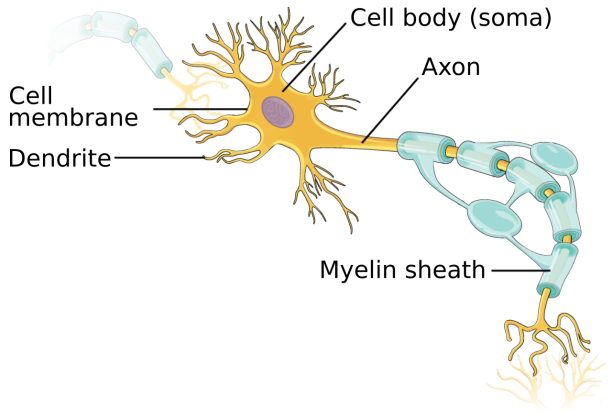

Figure 2.2: **Structure of a Neuron**. Diagram of the main components of a neuron. The cell bodies are found in gray matter while white matter is formed by axons. Adapted from Neurons and glial Cells of OpenStax College, Biology (CC BY 4.0)

these bundles are the corpus callosum that connects the two hemispheres, the longitudinal superior fasciculus that goes along each hemisphere, and the corticospinal tract that passes through a region called brainstem and connects the brain with the neurons that go to the extremities of the body, i.e. arms and legs.

The amount and complexity of neural connections are immense, these connections allow the creation of thoughts, memory storage, learning new skills, and control of all our limbs. It is extremely complex and interesting trying to understand how all this happens (Bassett and Gazzaniga, 2011). In recent decades, the development of noninvasive imaging techniques such as Diffusion-Weighted Magnetic Resonance Imaging (DW-MRI) allows the study of tissue in vivo and, in combination with image processing techniques, it has been possible to generate 3D reconstructions of white matter called tractography (Mori et al., 1999; Conturo et al., 1999; Jones et al., 1999; Basser et al., 2000; Poupon et al., 2000), allowing the study of structural connectivity of the brain in vivo (Hagmann, 2005; Sporns et al., 2005; Griffa et al., 2013), perform virtual dissections (Catani et al., 2002), diagnose patients (Jeurissen et al., 2017; Yeh et al., 2020), or plan surgeries (Catani and Dell'Acqua, 2011; Essayed et al., 2017). This thesis work aims to help the study of the brain, by proposing techniques to improve the tractography reconstructions of white matter.

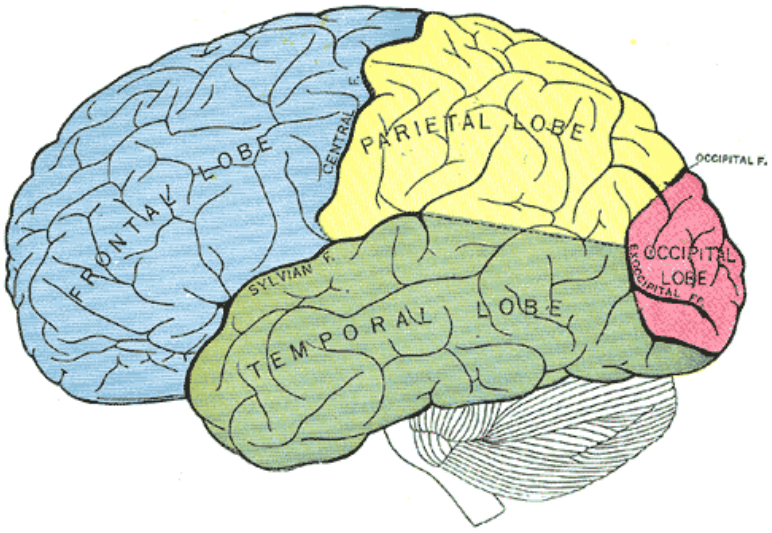

Figure 2.3: **Lobes and main sulci and boundaries of the brain**. The cortex of the brain contains undulations formed by gyri and sulci that are used as references for the analysis of the structure of the brain. Each hemisphere of the cortex can be divided into lobes: frontal, parietal, temporal, and occipital. Taken from (Gray and Lewis, 1918)

2.2 Measuring water diffusion in the human brain

Diffusion is a concept related to the random movement of particles. At the molecular level, the particles move randomly, colliding with each other in a fluid medium, that is described as Brownian movement. This movement was first observed and described by Brown (1828) who noticed the continuous and random motion of pollen grains.

At the macroscopic level, this movement can be described by Fick's first law (Fick, 1855). This says that the movement of the particles is affected by the concentration gradient of the particles, such that after a certain time the concentration of the particles tends to be uniform throughout the available space. This displacement is described by the equation

$$\mathbf{J}(\mathbf{r}, t) = -D\nabla c(\mathbf{r}, t), \tag{2.1}$$

where J is the number of particles passing through a unit area in a unit of time (flux), $\nabla c(\mathbf{r}, t)$ is the derivative with respect to the position of the particle concentration at time t and D is the diffusion coefficient, with units mm^2s, which depends on the temperature and viscosity of the medium and the size

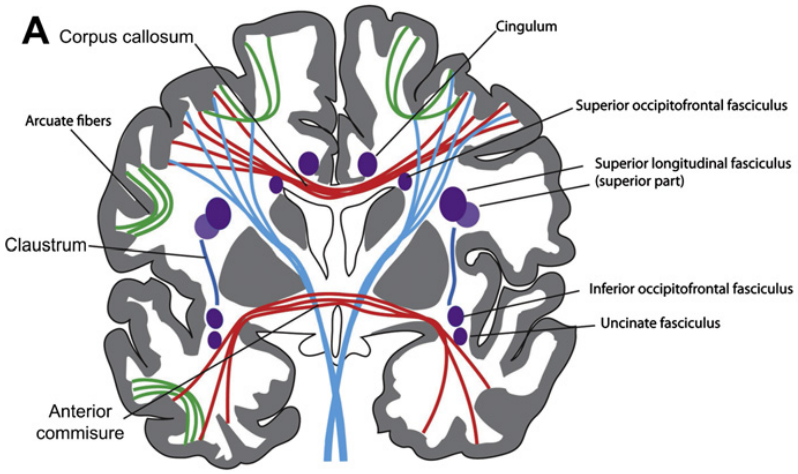

Figure 2.4: **Association, commissural, and projection white matter fibers.** Illustration of a coronal section of the brain presenting association (short fibers in green and long fibers as purple ovals), commissural (red), and projection (blue) white matter fibers. Taken from (Wycoco et al., 2013).

of the particles (Price, 1997). Fick's law describes that diffusion occurs from a region of high concentration to one of low concentration.

Einstein (1905) identified that Brownian motion is associated with the particle flux explained by Fick's law, but that does not require a macroscopic concentration gradient. The molecules experiment a self-diffusion process generated by local fluctuations of concentration. This movement can be described with a probability distribution $p(\mathbf{r}, t)$, where $\mathbf{r} = r_1 - r_0$ is the particle displacement from r_0 to r_1, the initial and final positions respectively, and t is the diffusion time (Jones, 2010).

In the absence of obstacles, the particles experiment *free diffusion*, where this is isotropic, and the displacement presents a Gaussian distribution

$$p(\mathbf{r}, t) = \frac{1}{\sqrt{(4\pi t)^3 D}} \exp\Big(- \frac{\mathbf{r}^T \mathbf{r}}{4tD} \Big). \tag{2.2}$$

Einstein generated an expression to know the mean square displacement in any direction in a medium with a diffusion coefficient D at time t. In one dimension this is

$$\langle r^2 \rangle = 2Dt, \tag{2.3}$$

and in three dimensions is

$$\langle \mathbf{r}^2 \rangle = 6\mathbf{D}t \tag{2.4}$$

where $\mathbf{D}$ is a diffusion tensor, a positive-definite symmetric matrix. The

diffusion tensor models the diffusion as a 3D Gaussian distribution, which can only have positive values in its eigenvalues, that describe the amount of diffusion in each axis of the Gaussian distribution, that in 3D can be represented as an ellipse. In the case of isotropic diffusion, the tensor will be a diagonal matrix with all the same eigenvalues. When the medium in which the molecules move has barriers, the diffusion is restricted or hindered (Le Bihan et al., 1993; Basser et al., 1994a). The first occurs when the molecules are completely surrounded by barriers and are enclosed in one region, the second when the particles are not completely enclosed and can surround the barriers. Depending on the diffusion time t, the particles will interact, or feel, the barriers to a greater or lesser extent, affecting the diffusion coefficient in some direction (Basser et al., 1994a). In this case, the eigenvalues of the diffusion tensor won't be equal and the diffusion experimented is called apparent diffusion coefficient (ADC).

2.2.1 Signal acquisition

Magnetic Resonance Imaging (MRI) (Mansfield, 1977; Lauterbur, 1973) is a noninvasive technique that manipulates the magnetic moments of protons to generate images, a description of the process is presented in (Grover et al., 2015; Hoult and Bhakar, 1997). The atoms that can be manipulated are the ones that have non-zero spin, which can absorb and emit electromagnetic radiation and experience resonance when placed in a magnetic field (Roberts, 1959). One example of these elements is hydrogen (a single proton in the nucleus), which is one of the most abundant elements in the human body (Lipton, 2008). The images are generated from the Nuclear Magnetic Resonance (NMR) (Rabi et al., 1938; Lauterbur, 1973; Mansfield, 1977) phenomenon, which describes how some nuclei of atoms absorb and release energy at specific radiofrequency. When this occurs the nucleus is in resonance, and it is possible to sense this energy and create images with contrasts that vary due to the properties of the tissue (see review in (Berger, 2002)).

NMR was first described by Isidor Isaac Rabi in 1938 (Rabi et al., 1938). In 1945 Felix Bloch (Bloch, 1946) and Edward Mills Purcell (Purcell et al., 1946) used the technique in liquids and solids respectively independently. In 1949 E. L. Hahn (Hahn, 1950) discovered the phenomenon known as "Free Induction Decay" which is the generated NMR signal. In 1971 Paul Lauterbur (Lauterbur, 1973) and 1976 Peter Mansfield (Mansfield, 1977) use the NMR to generate magnetic resonance images.

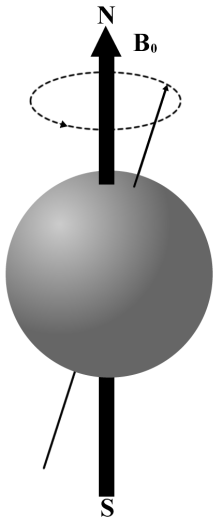

Figure 2.5: Scheme of a spin precessing around the magnetic field $\mathbf{B_0}$

Atomic nuclei, made up of protons and neutrons, have an intrinsic spin property. Atoms with an odd atomic number have a non-zero spin. They rotate with angular momentum and generate a magnetic field parallel to the axis of rotation, named magnetic momentum. This respects the right-hand rule and it has a north and a south pole, it behaves similarly to magnets (Grover et al., 2015). In presence of a large static magnetic field $\mathbf{B_0}$, the particles present a precession movement around the orientation of $\mathbf{B_0}$. Figure 2.5 is a schematic representation of the precession of one particle. The precession frequency depends on the magnitude of the magnetic field $\mathbf{B_0}$ and on the gyro-magnetic constant (γ) whose units are MHz/T. This is different for each element of the periodic table, so the frequency at which an atom precesses can be used to identify it (Bitar et al., 2006). This frequency is known as the Larmor Frequency (Larmor, 1897; Weishaupt et al., 2006)

$$\omega_0 = \gamma \mathbf{B}. \tag{2.5}$$

A greater proportion of the particles align in the direction parallel to the direction of $\mathbf{B_0}$ than antiparallel. This difference creates a net magnetization $\mathbf{M}$. The parallel particles are in low energy states and the antiparallel are in high energy states. Due to $\mathbf{M}$ is aligned and added with $\mathbf{B_0}$ it is not possible to measure it directly, and it has to be oriented in another direction. To do this, another magnetic field $\mathbf{B_1}$ is applied as electromagnetic radiation or radio frequency (RF) pulse with the same frequency ω_0 and in the perpendicular direction to $\mathbf{B_0}$. This process is called resonance and has two effects. First,

it creates a perturbation in the proton alignment, some low energy parallel protons flip to a high energy state, decreasing longitudinal magnetization. The second effect is that protons start to be synchronized and precess in phase, and the angle between some of their magnetic moment and $\mathbf{B_0}$ increases. This produces that the net magnetization vector turns towards the transverse plane. This is known as transverse magnetization, and this can induce a signal in an RF coil, that is the measured signal. When $\mathbf{B_1}$ is turned off, the protons resume their normal states, a process called relaxation.

The changing magnetic field generated by the realignment induces a current in the RF coil that generates a signal that changes as the magnetic field changes. From this signal, two phenomena can be observed. The spin-lattice relaxation time (T1), that describes how the longitudinal magnetization ($\mathbf{M}_{z,t}$) comes back to the original value. And the spin-spin relaxation time (T2) describes how the transverse magnetization ($\mathbf{M}_{xy,t}$) goes to zero. These relaxations are described by the expressions:

$$\begin{aligned} \mathbf{M}_{z,t} &= M(1 - \exp(-t/T1)) \\ \mathbf{M}_{xy,t} &= M_{xy,0t} \exp(-t/T2). \end{aligned} \tag{2.6}$$

Different tissues have different T1 and T2 properties, generating different signal values for the same time t. These different values create different contrast in the images that provide information about the tissue. For example, Table 2.1 contains a comparison between a T1-weighted and T2-weighted image, highlighting the differences between white matter (WM), gray matter (GM), cerebrospinal fluid (CSF). At first glance it can be noted that the contrasts are opposite, tissue that has a bright signal in one has a dark signal in the other and vice versa. Depending on the acquisition process, this contrast varies, allowing to highlight or identify different types of tissue, as well as pathological conditions. Examples of other types of contrast that allow to identify different properties of the tissue are presented in (Bitar et al., 2006; Mikulis and Roberts, 2007).

The magnetic field $\mathbf{B_0}$ is static and uniform, but the true magnetic field that the particles experiment is not the same for all of them. The magnetic field of each spin interacts with the magnetic fields of its neighbors, generating inhomogeneities on the magnetic field. This makes the spins precess at different frequencies, causing a faster dephase and the main reason for loss signal. This can be reversed by applying an RF pulse of 180° that inverts the magnetic spin vectors and which, while still exposed to inhomogeneities in the magnetic field,

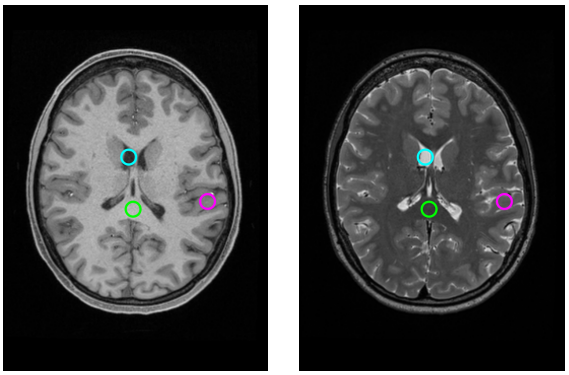

Tissue	T1-Weighted	T2-Weighted
Cerebrospinal fluid	Dark	Bright
White matter	Light	Dark Gray
Gray matter	Gray	Light Gray
Fat (within bone marrow)	Bright	Light

Table 2.1: **Comparison of a T1-weighted and T2-weighted image**. Example of two types of MRI to probe different properties of the tissues. Different tissues can present different signal intensities in images generated with different contrasts. Software used to display the MRI data: MRview of MRtrix (Tournier et al., 2019).

are rephased and the signal can be measured. The realignment or refocusing is called spin echo (Hahn, 1950; Stejskal and Tanner, 1965), and it occurs at echo time (TE), when the signal is measured.

To generate an image, that is a 3D volume of information formed by voxels (element of a regular 3D grid), some extra steps have to be done to localize and measure the signal in every voxel (Bitar et al., 2006). To do this, three magnetic field gradients are applied. A magnetic field gradient is a magnetic field that varies in space. These gradients are slice-selection, frequency-encoding, and phase-encoding. The slice-selection gradient is applied in the same direction of $\mathbf{B_0}$ field (z-axis), this allows the use of different Larmor Frequencies along the z-axis to interact with a specific slice. The other two gradients are used to generate the signal in the Fourier space, creating the *k-space* matrix, where the frequency-encoding direction is along one axis, and the phase-encoding direction along the other axis. By performing a 2D Fourier transform on the k-space matrix the MR image can be obtained for one slice. This process is done for every slice to obtain the 3D volume that can be visualized from different planes (axial, sagittal, or coronal) and also as a 3D object, as is

presented in Figure 2.6.

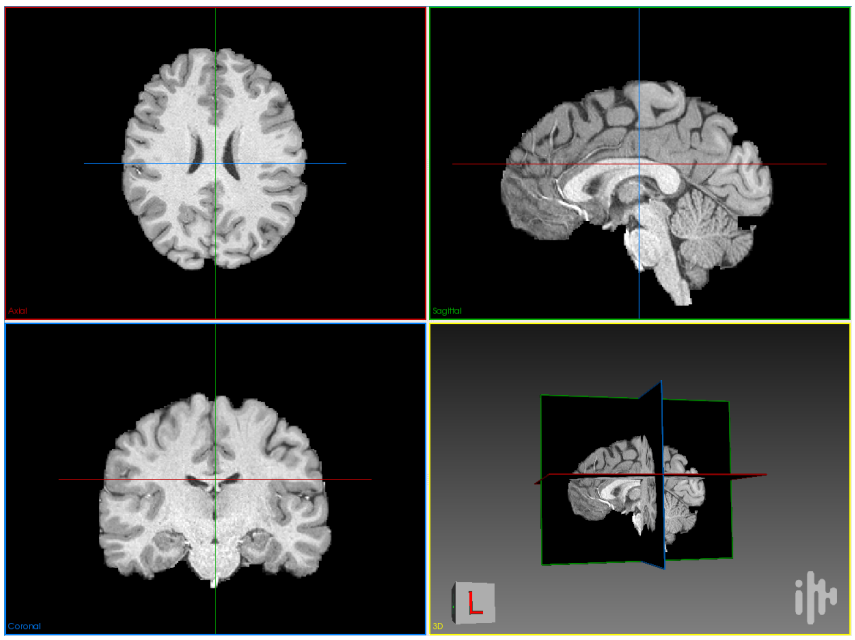

Figure 2.6: **Example of a T1-weighted MRI** visualized from three different planes (axial, sagittal, or coronal) and as a 3D object. Software used: MI-Brain[1]

Magnetic Resonance Imaging is a very complex and interesting research area, the theory and the technology developed around it are really fascinating. I think this because it lets us get information about the tissue (all the tissue, not only the brain) by sensing the atoms in the molecules that form it, and in a noninvasive way. To do this different protocols and sequences have been developed, more information about the MR pulse sequences can be found in (Bitar et al., 2006; Mikulis and Roberts, 2007). This section presented two examples of the different types of images that can be generated. There are more types of acquisitions that are adapted and optimized to detect specific tissue (like WM, GM, or CSF) and properties, like the diffusion of the molecules. This type of imaging is the most important for this thesis, and it will be described in the next section.

Diffusion-Weighted Magnetic Resonance Imaging

In a Diffusion-Weighted Magnetic Resonance Imaging (DW-MRI) the contrast is generated by the local particle diffusion (Stejskal and Tanner, 1965; Basser et al., 1994a). To measure diffusion, sequences of electromagnetic pulses and gradients are used, which magnetically label the particles, generating a signal that depends on their displacement (Grebenkov, 2007).

An electromagnetic gradient is a magnetic field that varies in space and can be applied in a specific angular direction. Figure 2.7 displays one of these sequences, the Pulse Gradient Spin Echo (PGSE), initially described by Stejskal and Tanner (1965), that is used to measure the particulars displacement along one direction. The first 90° pulse puts the spin in-phase and makes the net magnetization vector perpendicular to the $\mathbf{B_0}$ field. Then, an electromagnetic gradient G is turned on for a time δ, what generates a phase change in the spin, which depends on the magnitude of the gradient sensed by the particle according to its position. Then, in the middle of the sequence, a pulse of 180° is applied to reverse the effect of local inhomogeneities in the magnetic field. Then the gradient G is turned on again, that in this case, generates a reversed effect on the phase change. If a spin does not move, the second gradient reverses the effect of the first and there will be no change in the phase of the spin. At the end of the sequence, the signal is measured at echo time (TE).

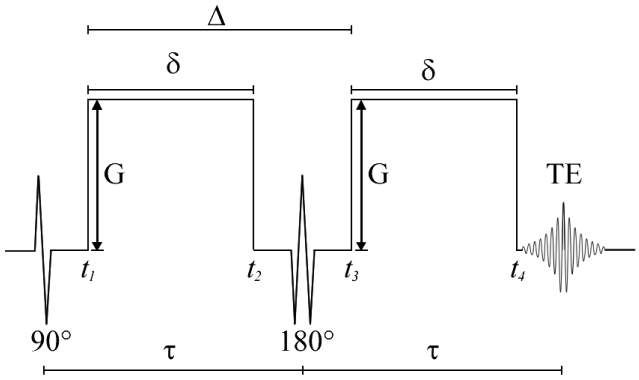

Figure 2.7: **Scheme of the Pulse Gradient Spin Echo sequence.** The sequence starts with a 90° pulse, then an electromagnetic gradient G is applied for δ time. At the middle of the sequence, a 180° pulse is applied. After this, a second gradient is applied at Δ time after the first. Finally, the signal is measured at echo time TE.

The resulting signal depends on the particle's movement, described with diffusion coefficient (D), along the direction of the gradient G. The Stejskal-Tanner equation describes the diffusion-weighted signal along the direction G

$$S = S_0 \exp(-bD), \tag{2.7}$$

where S_0 is the standard T2 signal intensity acquired with the same sequence PGSE but without the application of the gradient G, and b is the diffusion weighting (Stejskal and Tanner, 1965; Le Bihan et al., 1986), also knowing as

b-value. This b-value is proportional to the strength of G, and depends on the time δ that G is applied and the time interval Δ between the gradients:

$$b = \gamma^2 G^2 \delta^2 (\Delta - \delta/3), \tag{2.8}$$

with units s/mm^2, the inverse of the diffusion units, making the operation bD unit free. In brain tissue, as the diffusion experimented is not free, it is also called as apparent diffusion coefficient (ADC).

The configuration of these parameters tunes or indicates the displacement that we want to measure. Different parameter configurations will give us different information. Due to the strength of G can be fixed or restricted by hardware limitations, the b-value is modified changing the time that the diffusion is sensed, which also has limitations. It is important to keep in mind that the signal attenuation is described by an exponential decay and this can be affected by the signal to noise ratio (SNR) (Edelstein et al., 1986). In Figure 2.8 there are examples of DW-MRI acquisitions of three different b-values ($b \approx \{1000, 2000, 3000\}$s/mm^2) and three gradients G with directions approximately to the axis x, y and z. The data is from subject 100307 of the Human Connectome Project (Essen et al., 2013). We can see different patterns or structures highlighted in every gradient direction, this is due to the WM tissue hindered the displacement of the water molecules in an anisotropic way. We can see also different levels of contrast for the different b-values and different levels of noise, the different b-values are due to the different configurations of the acquisition protocol (Stejskal and Tanner, 1965; Burdette et al., 2001; Kingsley and Monahan, 2004).

Another important concept is the q-space (Callaghan, 1996; Hagmann et al., 2006). This is a 3D space where the diffusion information can be represented, the position of each diffusion value is defined with the q-vector

$$\mathbf{q} = \gamma \delta \mathbf{G}/2\pi, \tag{2.9}$$

that is related to the b-value in the way $b = t|\mathbf{q}|$, where $t = \Delta - \delta/3$. The gradient G defines the direction and the b-value is related to its length.

2.2.2 Modeling diffusion in the brain

The human brain, like all biological tissue, contains hydrogen molecules, present in water and fat. Due to this, it is possible to generate magnetic

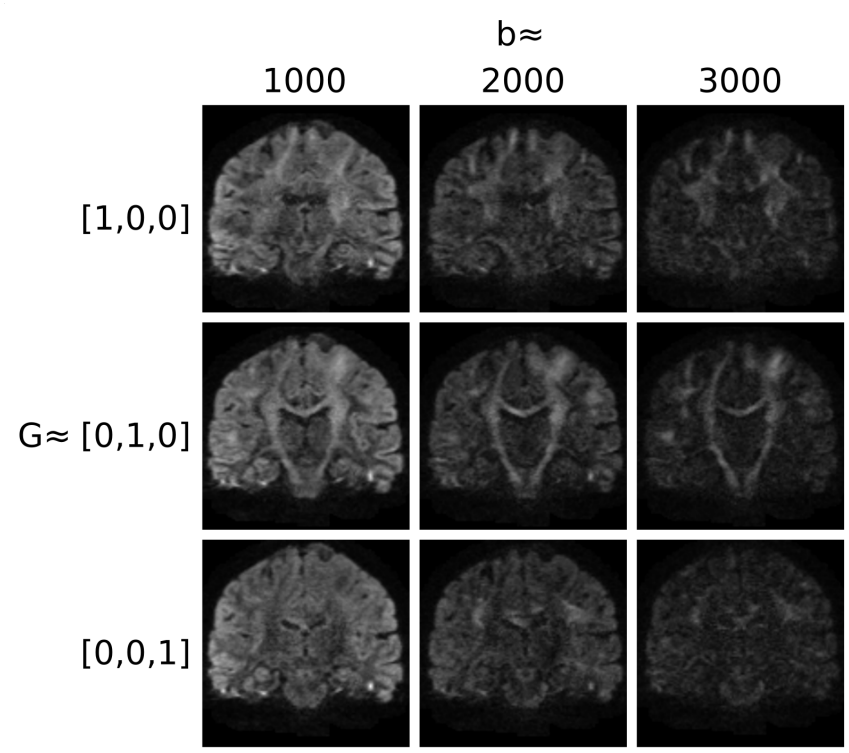

Figure 2.8: **Example of DW-MRI** acquired with different b-values ($b \approx \{1000, 2000, 3000\}$s/mm^2) and gradients G. Different structures can be appreciated by measuring the diffusion in different directions, while the b-value used changes the contrast in the images.

resonance images to noninvasively observe the tissue (Le Bihan and Iima, 2015), and depending on the contrast procedure used different properties of the tissue can be highlighted. DW-MRI is sensitive to the movement of molecules of water (Stejskal and Tanner, 1965; Basser et al., 1994a), that is affected by the tissue that can be seen like boundaries. If there are no boundaries, as in CSF, the diffusion is the same in all directions. In GM, cells and tissue structures block the movement of the particles and the diffusivity is limited in all directions. While in WM, composed mostly of axons, the water diffuses more in direction parallel to the axons bundles than in perpendicular direction. By processing the signal is possible to distinguish the type of tissue, and infer properties like the direction of the axon bundles (Tournier et al., 2011), which is one of the most important information for this work.

The displacement of the molecules is described by the diffusion propagator $p(\mathbf{r}, t)$, that is a probability function of any displacement $\mathbf{r}$ in the diffusion time t, it is also called diffusion probability density function (dPDF). This probability is related to the signal attenuation $E(\mathbf{q}, t) = S(\mathbf{q}, t)/S_0$ measured

in the position described in $\mathbf{q}$ in the q-space by the equation

$$E(\mathbf{q}, t) = \int_{\mathbb{R}^3} p(\mathbf{r}, t) \exp(-2\pi i \mathbf{q}^T \mathbf{r}) d\mathbf{r}. \tag{2.10}$$

This relation is the Fourier transform when the diffusion gradient is infinitely small, and the full q-space is sampled (Callaghan et al., 1988), which is not possible to do. Non-infinitely time is required to generate the gradients, these are no Dirac pulses, and to sample a full q-space, infinite and null gradient strength are required, which is not possible to have. Because of these limitations, it is not possible to compute the true diffusion propagator, and simple models of diffusion have been proposed. One of the firsts models, that is still widely used, is the diffusion tensor model (Basser et al., 1994b), which uses a covariance matrix to describe the probability of displacement with a Gaussian distribution, which in most cases is far to represent the diffusion propagator (Mori and Tournier, 2014). More complex models try to generate a more accurate representation of this diffusion propagator by computing an ensemble average propagator, which shares the angular profile of the diffusion propagator (Cory, 1990), this using the Fourier transform relationship between the signal attenuation and the diffusion propagator. The next sections present the diffusion tensor model (Diffusion tensor imaging) and other more complex approaches (High angular resolution diffusion imaging) to describe the dPDF. The general idea of these approaches is to use different samples of the q-space (different directions and b-values) to recover the dPDF.

Diffusion Tensor Imaging

Diffusion Tensor Imaging (DTI) uses a second-order symmetric and positive-definite matrix (tensor) to model the diffusion in biological tissues (Basser et al., 1994b; Pierpaoli et al., 1996):

$$\mathbf{D} = \begin{pmatrix} D_{xx} & D_{xy} & D_{xz} \\ D_{yx} & D_{yy} & D_{yz} \\ D_{zx} & D_{zy} & D_{zz} \end{pmatrix} \tag{2.11}$$

This matrix can be estimated using different measurements of the signal and generates a system of equations from the Stejskal-Tanner diffusion

equation, which for a direction of gradient G_i is

$$\ln\left(\frac{S_i}{S_0}\right) = -b\mathbf{G_i}^T\mathbf{D}\mathbf{G_i}, \tag{2.12}$$

where S_i/S_0 is also known as signal attenuation and corresponds to the DW-MRI (S_i) normalized by the MRI measured without diffusion weighting (S_0), that is a T2 weighted image. To derive the complete diffusion tensor, at least six measurements in non-co-linear directions $\mathbf{G_i}$ and one S_0 have to be taken. However, since many factors affect the quality of acquisitions like noise, distortions, and artifacts, more signals are used to over-fit the tensor (Giannelli et al., 2010).

The diffusion tensor can be visualized as a 3D ellipsoid. The eigenvectors $[\hat{e}_1, \hat{e}_2, \hat{e}_3]$ of $\mathbf{D}$ define the main axes of the ellipsoid and the eigenvalues $\lambda_1 \geq \lambda_2 \geq \lambda_3$ of the matrix corresponds to the apparent diffusion coefficient in each direction and define the shape of the tensor. Figure 2.9 illustrates some forms of the tensor, that can have different interpretations. The prolate diffusion ($\lambda_1 \gg \lambda_2 \simeq \lambda_3$) appears to be cigar-shaped, while oblate diffusion ($\lambda_1 \simeq \lambda_2 \gg \lambda_3$) appears to be plate-shaped and the isotropic diffusion ($\lambda_1 \simeq \lambda_2 \simeq \lambda_3$) is a sphere.

The eigendecomposition of the tensor allows the computation of diffusion properties, like the axial (AD), radial (RD), and Mean Diffusivity (MD), and the Fractional Anisotropy (FA), see description in (Alexander et al., 2007; O'Donnell and Westin, 2011). The axial diffusivity is the magnitude of diffusion along the eigenvector $\hat{e}_1$ and its value is λ_1, that in the case of one fiber population this is parallel to the fibers. Changes in the AD may reflect axonal changes, like axonal injury, less coherent orientation, or reduced axonal caliber. The radial diffusivity is the average diffusivity perpendicular to $\hat{e}_1$ and its value is $(\lambda_2 + \lambda_3)/2$. In the case of one fiber population, it represents the diffusion perpendicular to the fibers. An increase of RD may reflect myelin loss or reduced axonal packing density. The MD characterizes the overall mean-squared displacement of the water molecules, it is the average magnitude of the diffusion along the three eigenvectors. The increment of MD can be due to axonal degradation that reduces the integrity of WM. It can be calculated by taking the sum of eigenvalues or the trace of the tensor:

$$MD = \frac{1}{3}(\lambda_1 + \lambda_2 + \lambda_3) = \frac{1}{3}Tr(\mathbf{D}). \tag{2.13}$$

FA describes the overall directionality of water diffusion, it is the fraction of diffusion that is directionally dependent (anisotropic). A value of zero means that diffusion is equally restricted in all directions (isotropic). High values mean that diffusion occurs mostly anisotropic. Changes in FA might reflect changes in axonal packing density or enlarged axonal diameter. It can be computed as:

$$FA = \sqrt{\frac{3}{2}}\sqrt{\frac{(\lambda_1 - MD)^2 + (\lambda_2 - MD)^2 + (\lambda_3 - MD)^2}{\lambda_1^2 + \lambda_2^2 + \lambda_3^2}}. \tag{2.14}$$

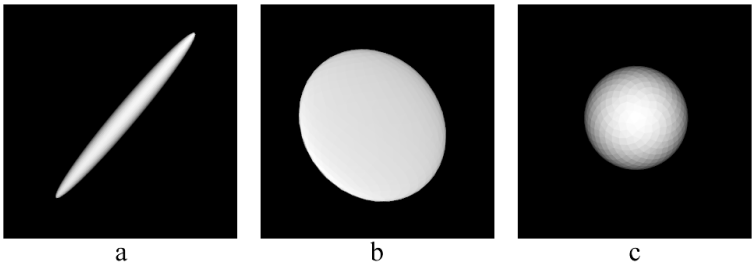

Figure 2.9: **Tensors as ellipsoids.** Examples of the representation of tensors as ellipsoids. a) prolate, b) oblate, and c) isotropic diffusion.

Up to now DTI is highly used in clinical applications because of its small acquisition time and easy parameter configuration. It is a good tool for visualizing and assessing microstructure information of brain tissue, but it suffers from a significant limitation, the assumption of Gaussian diffusivity (Tournier et al., 2011). Only one fiber population can be modeled using a tensor. This is an important limitation when there is more than one fiber population per voxel and has been estimated that in 90% of the voxels there are crossing fibers (Jeurissen et al., 2013) and this is an important limitation to perform tractography.

High Angular Resolution Diffusion Imaging

High Angular Resolution Diffusion Imaging (HARDI) (Frank, 2001) is a research area that overcome the limitations of DTI, see reviews in (Descoteaux, 2008, 2015; Tournier et al., 2011; Mori and Tournier, 2014). It uses more descriptive diffusion models for fiber crossing, but it requires more data: a greater number of diffusion directions of DW-MRI and with a higher gradient weighting. The idea is to have many samples of the q-space to reconstruct the real diffusion propagator function also called dPDF.

Different algorithms that use the HARDI approach have been developed, which can be classified in model-free and model-based techniques (Descoteaux, 2015). In both cases the number of measurements and acquisition requirements will depend on the application or algorithm objective, two examples of these approaches to acquire the signal are: 1) sampling the whole q-space or 2) sampling shells defined by b-values. Figure 2.10 displays three examples of measures acquired on the q-space. Each point represents the direction of measurement and the distance to the center, where no diffusion is measured (b-value=0), is related to the b-value magnitude. The first image is a dense sampling of the space, this sampling scheme is associated with Diffusion Spectrum Imaging (DSI) (Callaghan et al., 1988). In the second image, the measurements are at the same distance to the center, like in a surface of a sphere, which is also called *shell*. The third image presents a multi-shell sampling, in the example the measurements are taken at three different b-values, creating three spheres.

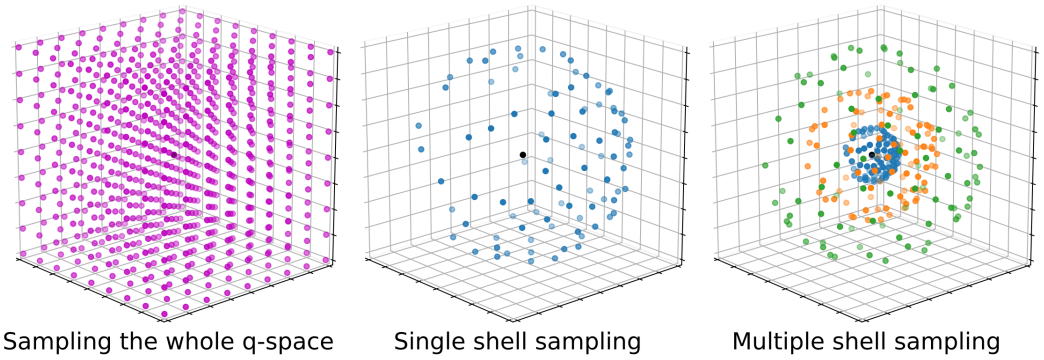

Figure 2.10: **Examples of q-space sampling.** Dense sampling and two sparse sampling performed in one shell and in multiple shells. The black dot represents the sample where no diffusion is measured (b-value=0).

The reconstruction of the real dPDF is a difficult task, but some properties of it can be computed and represented in mathematical objects. One of the most important of these objects is the diffusion orientation distribution function (dODF). The dODF has the same angular profile of the dPDF (Cory, 1990), and is defined as the radial integral of the diffusion propagator in spherical coordinates. It can be represented as a spherical function on the unit sphere using a mesh in which every vertex is proportional to the value of the dODF on the sphere. Another mathematical tool to represent functions on the sphere is the decomposition on an orthonormal basis called spherical harmonics (SH) (Frank, 2002; Alexander et al., 2002). The SH are frequency-space

complex functions that can be denoted with parameters: harmonic order l and phase factor m. They are well-suited for describing the directional changes (Tournier et al., 2004, 2007). The SH can be used to represent orientation distribution functions (ODFs) and DW-MRI signals, which are real and symmetric functions. Because of this characteristic, a truncated series of SH and only real and even terms are used. Figure 2.11 presents a visual representation of examples of SH, those are presented as spherical plots with radius as function of the signal. The geometrical representations have negative (black) and positive (white) values. The functions with order even are antipodal symmetrical and with order odd are antisymmetrical (Minati and Węglarz, 2007), that is, the symmetric values have opposite signs. As the functions to represent are symmetric, those odd-order SHs are not used. Something to note is that the angular frequency (degree) increases as the harmonic order increases.

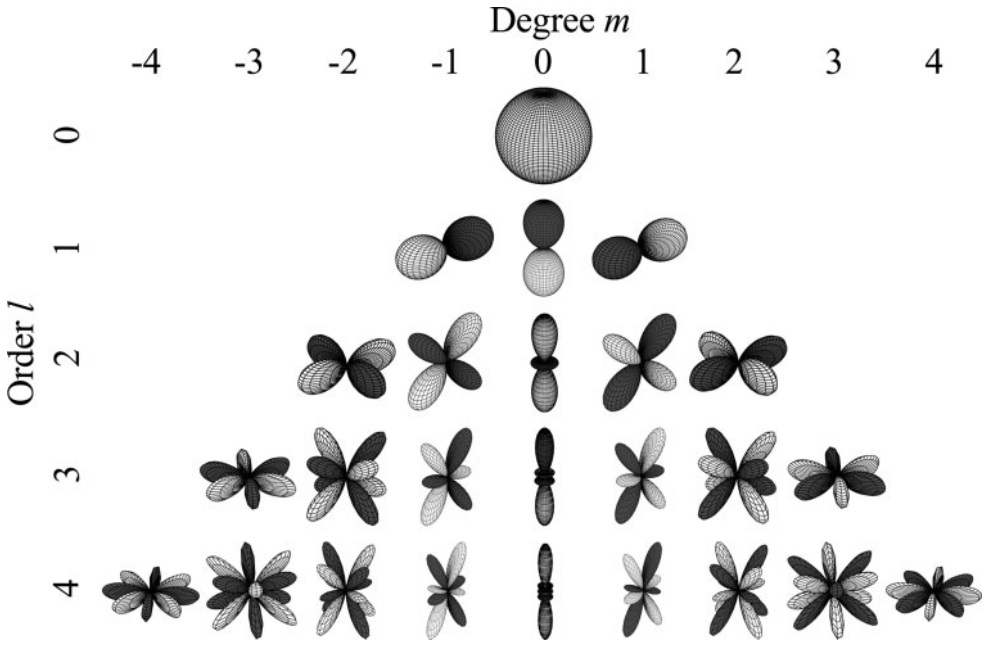

Figure 2.11: **Visual representation of some real spherical harmonics.** The dark regions represent negative values and the white regions positive ones. The functions with order (l) even are antipodal symmetric and the ones with order odd are antisymmetric, that is, the symmetric values have opposite signs, the degree $m \in [-l, l]$ increases with the order l. Taken from (Minati and Węglarz, 2007).

One of the first attempts to describe crossing fiber configurations was computing the apparent diffusion coefficient (ADC) by taking the natural logarithm of the signal to reconstruct a dODF. In the case of a single-fiber population, the maximum ADC is aligned to the fiber population orientation,

similar to the tensor model. But when multiple-fiber populations are present in the voxel, the ADC profile does not agree with the fiber orientations, i.e. the maximum values of ADC are not aligned with the fiber populations (Tuch et al., 2002; von dem Hagen and Henkelman, 2002).

One solution proposed to reconstruct a dODF aligned to the fiber populations is the Q-ball imaging (Tuch, 2004) that reconstructs a smoothed version of the true dODF from single-shell measurements. It uses the Funk-Radon transform, which computes integrals over circles defined over the unit sphere. The Funk-Radon transformation works in the case of crossing of multiple fiber populations, but if the angle at which they cross (angular resolution) is big enough. When the angular resolution starts to be small ($< 60°$) the maximal diffusion is not anymore aligned to the fiber populations. This is not the best information to perform tractography, it is required an object that supports bigger angular resolution, like a fiber orientation distribution (Descoteaux et al., 2009).

A fiber orientation distribution function (fODF) is a function on the sphere like the dODF but sharper. It is possible to represent and identify fiber populations more clearly even at an angular resolution of 45° and it can be computed by performing a Spherical deconvolution (Tournier et al., 2004, 2007).

The Spherical deconvolution is a method that estimates the underlying fODF suited to tractography in the living human brain (Dell'Acqua and Tournier, 2019). It assumes that the signal associated with a crossing of fiber populations can be created by the convolution of a single fODF function (also called response function) and the direction of the fiber populations (Tournier et al., 2004, 2007). The response function, used as deconvolution kernel, can be generated using diffusion models for a single fiber or it can be estimated from the data from a region where it is known that there is only one fiber population. Usually, a region with FA>0.7 is considered to have one fiber population, and it is used to compute the response function. If the convolution theorem is used with the spherical harmonics, the problem can be defined as the multiplication in spherical harmonics space: $\mathbf{S} = \mathbf{RF}$, where $\mathbf{S}$ is the signal generated from the multiplication of the response function $\mathbf{R}$ and the fiber distribution orientation $\mathbf{F}$, that in our case is what we want to know. This can be estimated using a least-squares formulation ($\mathbf{F} = (\mathbf{R}^T\mathbf{R})^{-1}\mathbf{S}$), but the direct solution is not stable, generates negative values (the spherical harmonics contain negative values) and false spurious peaks (Tournier et al.,

2004; Alexander, 2005). To deal with this, constraints that regularize the problem need to be added to ensure stability and positivity (Tournier et al., 2007; Ramirez-Manzanares et al., 2007), and a constrained spherical deconvolution is performed to compute the fODF. Figure 2.12 displays examples of fODF estimated with the multi-shell, multi-tissue constrained spherical deconvolution algorithm (Jeurissen et al., 2014) on a brain. The fFODs are presented as spherical polar plots with radius as function of the signal, it is possible to see one (a), two (b), and three (c) main orientations in the first three cases, but in the case of (d) is not as clear or easy to interpret the structure as in the others.

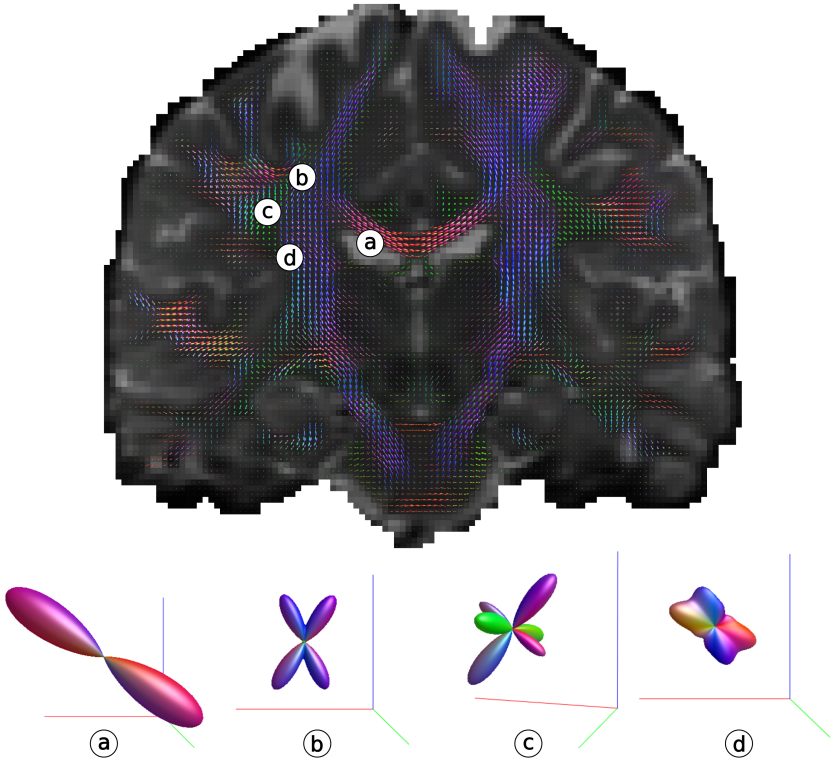

Figure 2.12: **Examples of fODFs** estimated in voxels in different parts of a brain. The fODFs have different shapes that represent the possible structure of the fiber population in the voxels. It is possible to see one main orientation (**a**) and the crossing of two (**b**) and three (**c**). In the case of (**d**) is not as clear as the others to interpret the fODF.

HARDI has some limitations in fiber crossing configurations, as many voxels configurations can lead to the same diffusion profile (Descoteaux, 2015). Inside a voxel the fibers can curve, fan, cross, merge, kiss, branch, join, bottleneck, and combinations of the previous that produce a similar fODF. The exact diffusion profile of these configurations is unknown and ambiguous (Savadjiev et al., 2008).

2.3 Microstructure models

This section presents some examples of multi-compartment model formulations for describing properties of the brain tissue. As it was described in Section 2.2.1, DW-MRI of in vivo tissue is created from the movement of water molecules within the tissue, that can be inside and outside the axons, and other microstructures like the body of neurons and other cells like glia. The water in all these different micro-environments experiments different diffusion phenomenons that contribute to the signal measured, which has been modeled using multi-compartment approaches, see reviews in (Panagiotaki et al., 2012; Jelescu and Budde, 2017; Novikov et al., 2019; Alexander et al., 2019). The multi-compartment models represent different tissue microstructures and make biological assumptions about the tissue and the water diffusion in it. These models can be used to infer information of the anatomical structure of the tissue (Assaf and Basser, 2005; Jelescu et al., 2016; Szczepankiewicz et al., 2015; Coronado-Leija et al., 2017) inside a voxel like fiber orientation (Ramirez-Manzanares et al., 2007; Kaden et al., 2008), volume fraction (Zhang et al., 2012; Kaden et al., 2016a), or axonal diameter (Alexander et al., 2010; Assaf et al., 2008; Huang et al., 2015; Veraart et al., 2020) depending on the model and the signal acquisition used. The use of multi-compartment models to consider different signal sources can improve the estimation of the fiber orientation density and create a better representation of the tissue and anatomy, but their integration and interpretation are not simple (Cercignani and Bouyagoub, 2018). This information can be also used for diagnosis and detection of white matter degeneration (Szczepankiewicz et al., 2016).

2.3.1 Multi-Gaussian model

One idea to model the multiple fiber populations that can be in a voxel is to use multiple tensors (Tuch et al., 2002; Parker and Alexander, 2003), also called Multi-Gaussian model. The idea is to use a sum of independent tensors to reproduce the signal

$$\frac{S}{S_0} = \sum_i f_i \exp(-D_i), \tag{2.15}$$

where f_i is the volume fraction of the tensor D_i.

Different approaches have been proposed to solve the problem, to find a set of tensors and the corresponding volume fractions. Some assumptions

are imposed to try to make the problem more stable or simpler, like considering radial symmetry (Alexander, 2008) with a zeppelin shape ($\lambda_2 = \lambda_3$), constraining the value of the eigenvectors, or imposing a ratio among them. This problem has been solved using a set of diffusion basis functions (Ramirez-Manzanares et al., 2007), generated using the tensor diffusion models distributed as uniformly possible in the 3D space of orientations. Their eigenvalues are selected according to prior information about the longitudinal and transversal diffusivity. By fixing these properties of the tensor, the degree of freedom of the problem is reduced, and only the volume fraction parameters have to be estimated, to find the best linear combination of basis functions that reproduce the signal.

2.3.2 Ball and stick model

The ball and stick mixture model (Behrens et al., 2003, 2007) considers two types of diffusion: isotropic (free water) and anisotropic (inside and around the axons), without diffusion exchange, which assumes the diffusion experimented in each compartment is independent. The simplest model uses an isotropic tensor to model the free water and assumes that the fibers that pass through a voxel have all the same orientation, modeling the diffusion only in the fiber direction with an anisotropic tensor (Behrens et al., 2003). This model was extended to multiple fiber orientations, where the signal is split into an anisotropic compartment for each fiber orientation and a single isotropic component (Behrens et al., 2007). The diffusion signal for each direction is modeled as:

$$S_i = S_0\left(\left(1-\sum_{j=1}^{N} f_j\right)\exp(-b_i d) + \sum_{j=1}^{N} f_j \exp\Big(-b_i d G_i^T R_j A R_j^T G_i\Big)\right), \quad (2.16)$$

where S_0 is the signal without diffusion weighting, d is the diffusivity, b_i and G_i are the b-value and the gradient associated with the ith measurement, f_j and $R_j A R_j^T$ are the signal fraction and the anisotropic diffusion tensor of the jth fiber orientation, N is the maximum number of fibers. The anisotropic diffusion tensor, with diffusion only in the axial direction, has the shape of a stick and it is described as:

$$A = \begin{pmatrix} 1 & 0 & 0 \\ 0 & 0 & 0 \\ 0 & 0 & 0 \end{pmatrix}, \quad (2.17)$$

R_j rotates A to the jth fiber orientation.

The problem is solved with a Bayesian approach called automatic relevance determination. Something that the authors recommend is to infer multiple fiber populations where there is evidence in the data that is the case, because when the data only supports a single fiber population fitting a more complex model may lead to a poor estimation of the true fiber orientation, allowing second fiber orientations when they do not exist, that will affect the tractography reconstructions.

2.3.3 Neurite orientation dispersion and density imaging

The Neurite Orientation Dispersion and Density Imaging (NODDI) (Zhang et al., 2012) is an MRI technique for estimating the microstructural complexity of neurites (dendrites and axons) in vivo on clinical MRI scanners. It combines a three-compartment tissue model with a two shell HARDI protocol optimized for clinical feasibility. It computes indices of neurites related to their density and orientation dispersion (angular variation of neurites). The authors explained that the orientation dispersion can be estimated with a single HARDI shell and neurite density requires at least two shells. The tissue model used by NODDI considers three types of microstructural environments: intra-cellular, extra-cellular, and CSF compartments. The full normalized signal S is written as:

$$S = (1 - v_{iso})(v_{ic}S_{ic} + (1 - v_{ic})S_{ec}) + v_{iso}S_{iso}, \tag{2.18}$$

where S_{ic} and v_{ic} are the signal and volume fraction of the intra-cellular compartment, S_{ec} is the signal of the extra-cellular compartment, and S_{iso} and v_{iso} are the normalized signal and volume fraction for the CSF compartment.

The intra-cellular compartment is related to the space that is inside the neurites, this is modeled as a set of sticks (Behrens et al., 2003) that can be parallel or dispersed. This to model the full spectrum of neurites orientation patterns observed in the brain, like in white matter the highly coherently oriented (e.g., corpus callosum), bending and fanning axons (e.g., centrum semiovale), and the gray matter structures characterized by dendrites in all directions. The normalized signal is:

$$S_{ic} = \int_{\mathbb{S}^2} f(\mathbf{n}) \exp^{-bd_{\parallel}(\mathbf{G}\cdot\mathbf{n})^2} d\mathbf{n}, \tag{2.19}$$

where $\mathbf{G}$ and b are the gradient and b-value of the measurement respectively. $f(\mathbf{n})d\mathbf{n}$ gives the probability of finding sticks along orientation $\mathbf{n}$ (modeled with a Watson distribution), $\exp^{-bd_{\parallel}(\mathbf{G}\cdot\mathbf{n})^2}$ is the signal attenuation along a stick with intrinsic diffusivity $d_{\parallel}$ and orientation $\mathbf{n}$. The orientation distribution function f is modeled with a Watson distribution, that is the simplest orientation distribution that can capture the dispersion in orientation, the formula used is:

$$f(\mathbf{n}) = M\Big(\frac{1}{2}, \frac{3}{2}, \kappa\Big)^{-1} \exp(\kappa(\mu\mathbf{n})^2), \tag{2.20}$$

where M is a confluent hypergeometric function, μ is the mean orientation, and κ is the concentration parameter that measures the extent of orientation dispersion about μ.

The extra-cellular compartment is the space around the neurites, where can be different types of structures like glial cells and, in gray matter, cell bodies. This is modeled as Gaussian anisotropic diffusion

$$logA_{ec} = -b\mathbf{G}^T\Big(\int_{\mathbb{S}^2} f(\mathbf{n})D(\mathbf{n})d\mathbf{n}\Big)\mathbf{G}, \tag{2.21}$$

where $D(\mathbf{n})$ is a cylindrical symmetric tensor (zeppelin) with principal diffusion direction $\mathbf{n}$, and diffusion coefficients $d_{\parallel}$ and $d_{\perp}$ parallel and perpendicular to $\mathbf{n}$ respectively. $d_{\parallel}$ is the same as the one in the intra-cellular compartment. $d_{\perp}$ is computed with a tortuosity model (Szafer et al., 1995) as $d_{\perp} = d_{\parallel}(1 - v_{ic})$, where v_{ic} is the intra-cellular volume fraction.

The CSF compartment models the diffusion in the cerebrospinal fluid as an isotropic Gaussian distribution with diffusivity d_{iso}.

The indices computed by the method are estimated from the volume fraction v_{ic} (density) and the concentration parameter κ used in the Watson distribution (dispersion). This last is mapped with the function

$$OD = \frac{2}{\pi}\arctan(1/\kappa), \tag{2.22}$$

to have it in ranges from 0 to 1.

An optimized acquisition protocol was generated for the NODDI tissue model. This protocol has two HARDI shells with b-values of 711 and 2855s/mm^2, that can be achieved by clinical systems. For the first value, 30 measurements are acquired, 60 for the second, and 9 $b = 0$. The reason the second gradient has more measurements than the first one is to account for the higher signal variation over the sphere due to its sensitivity to complex

microstructure configuration.

One limitation of the model is that by describing the axon orientation distribution with a single Watson distribution it does not account for fiber crossings and assumes a single fixed intrinsic diffusivity over the whole brain and across MRI protocols, subjects with different age or neurological conditions, what can be a source of overestimation of the CSF compartment in WM (Kaden et al., 2016a).

2.3.4 Multi-compartment microscopic diffusion model based on the Spherical Mean Technique

The method called Multi-compartment microscopic diffusion imaging estimates the microscopic features specific to the intra- and extra-neurite compartments in the brain unconfounded by the effects of fiber crossings and orientation dispersion (Kaden et al., 2016a). This method is based on the Spherical Mean Technique (SMT) (Kaden et al., 2016b), that factors the neurite orientation distribution and provides direct estimates of the microstructure of the brain tissue. It requires two HARDI shells that can be acquired in clinical scan times.

For this method, it is assumed that the macroscopic diffusion signal is a product of the macroscopic diffusion process and the neurite orientation distribution. Thus, to recover the microscopic tissue features in the brain, the intra-voxel fiber orientation distribution has to be removed for consideration. The method uses the diffusion anisotropy mapping based on the SMT (Kaden et al., 2016b). Where, for any fixed b-value (gradient magnitude and time), the spherical mean of the diffusion signal over the gradient directions is in function of the voxel-average microscopic diffusion process and not on the microdomain orientation distribution, making it independent of the fiber orientation distribution. Kaden et al. (2016a) extends this method, and introduces a multi-compartment model that considers the presence of multiple tissue compartments to map the neurite density and compartment-specific diffusivities without been affected by the effects of the fibers crossing and orientation dispersion. This is done without assumptions about the neurite distribution, like single or multiple orientations or spherical harmonics dictionary. After modeling the diffusion signal, it is possible to estimate the fiber orientation distribution using spatial varying multi-compartment response functions in a spherical deconvolution approach.

The Spherical Mean Technique assumes that the microscopic tissue

geometry is rotationally symmetric around $\omega \in S^2$. Using a diffusion weighting factor $b \geq 0$ and an unite gradient g the direction of measurement in a fixed time, the microscopic diffusion signal is:

$$h_b(g, \omega) = h_b(\langle g, \omega \rangle) \tag{2.23}$$

that depends only on the spherical distance $\langle g, \omega \rangle \in [-1, 1]$. Using this diffusion model (Kaden et al., 2016b) proved that the spherical mean of the diffusion signal over the gradient directions is not affected by the neurite orientation distribution. For a fixed b-value in the acquisitions, the mean diffusivity signal is

$$\bar{e}_b = \int_0^{\pi/2} h_b(\cos(\theta)) \sin(\theta) d\theta, \tag{2.24}$$

where θ encodes the angle between the gradient direction and microdomain orientations.

In (Kaden et al., 2016a) the microscopic diffusion model uses two Gaussian compartments to describe the brain tissue. An intra-neurite compartment, that represents the dendrites and axons, that may be surrounded by myelin sheaths (that for long sufficient times does not significantly contribute to the measured signal), with cylindrical geometries. The second compartment is the extra-neurite, that represents neurons, glial cells, astrocytes, and extra-cellular space. The diffusion signal is decomposed as follows:

$$h_b(g, \omega) = v_{\text{int}} h_b^{\text{int}}(g, \omega) + (1 - v_{\text{int}}) h_b^{\text{ext}}(g, \omega), \tag{2.25}$$

where h_b^{int} and h_b^{ext} are the signal from the intra- and extra-neurite compartment, and $v_{\text{int}} \in [0, 1]$ is the intra-neurite volume fraction. With the assumption of not exchange between compartments and with the intention of using low b-values, that are suitable for clinical scan times, and from which the signal perpendicular to the neurites is not detectable, a model with zero transverse diffusivity (Behrens et al., 2003) is used to describe the intra-neurite compartment:

$$h_b^{\text{int}}(g, \omega) = \exp(-b \langle g, \omega \rangle^2 \lambda), \tag{2.26}$$

where $0 \leq \lambda \leq \lambda_{\text{free}}$ is the diffusion coefficient parallel to the neurites with the upper bound the free-water diffusivity λ_{free}. The signal for the extra-neurite component is modeled with a rotationally symmetric tensor, computed with

the multiplication of the longitudinal and transverse component:

$$h_b^{\text{ext}}(g.\omega) = \exp(-b\langle g,\omega\rangle^2\lambda)\exp(-b(1-\langle g,\omega\rangle^2)\lambda_\perp^{\text{ext}}), \tag{2.27}$$

where the transverse extra-neurite diffusion coefficient is computed from the tortuosity model $\lambda_\perp^{\text{ext}} = (1 - v_{\text{int}})\lambda$.

The mean diffusion signal for the multi-compartment microscopic model, for a fixed b-value, is computed as:

$$\bar{e}_b = v_{\text{int}}\bar{e}_b^{\text{int}} + (1 - v_{\text{int}})\bar{e}_b^{\text{ext}}, \tag{2.28}$$

where

$$\bar{e}_b^{\text{int}} = \frac{\sqrt{\pi}\text{erf}(\sqrt{b\lambda})}{2\sqrt{b\lambda}} \tag{2.29}$$

and

$$\bar{e}_b^{\text{ext}} = \exp(-b\lambda_\perp^{\text{ext}})\frac{\sqrt{\pi}\text{erf}(\sqrt{b(\lambda-\lambda_\perp^{\text{ext}})})}{2\sqrt{b(\lambda-\lambda_\perp^{\text{ext}})}} \tag{2.30}$$

are the spherical mean signals for the intra- and extra-neurite compartments, respectively, b is the diffusion weighting factor, and erf is the error function

$$\text{erf}(x) = \frac{2}{\pi}\int_0^x \exp(-t^2)dt, \tag{2.31}$$

that is a complex function that for real arguments has real value. The parameters to be estimated are the intra-neurite volume fraction $v_{\text{int}} \in [0, 1]$ and the diffusion coefficient λ.

2.4 Tractography

Tractography is a research area that is able to generate 3D reconstructions of the major neural tracts in the WM of the brain, in vivo and noninvasively (Mori et al., 1999; Conturo et al., 1999; Jones et al., 1999; Basser et al., 2000; Poupon et al., 2000). It uses DW-MRI data that provides information on the diffusion of water molecules within brain tissue. Tractography generates polylines, called streamlines, aligned to the orientations of maximal diffusivity that approximate large sets of axon trajectories and describes the structure and connectivity of the brain (Hagmann, 2005; Sporns et al., 2005). It is important to note that tractography is able to map large axonal bundles, a single streamline represents

a group of axons and not only one (Jones et al., 2013; Schiavi et al., 2020). Tractography reconstructions allow us to study brain function and development (Assaf et al., 2019), to study neurological diseases (Jeurissen et al., 2017; Yeh et al., 2020; Griffa et al., 2013), to perform virtual dissections (Catani et al., 2002) for neurosurgical applications (Catani and Dell'Acqua, 2011; Essayed et al., 2017), because of these and other applications in neuroscience it is worth studying and developing tractography.

The pipeline to perform tractography is long, complicated, and plenty of big and interesting research areas, like signal acquisition and postprocessing to remove artifacts and noise, diffusion modeling, and microstructure reconstruction (Jeurissen et al., 2017). Technical limitations (Thomas et al., 2014) and practicals, like pain and discomfort in the subjects (Formica and Silvestri, 2004; Tsai et al., 2015; Sammet, 2016) affect the signal acquisition needed to perform tractography. There are many strategies to perform tractography (Jeurissen et al., 2017), but most of the pipelines have three main parts, the local diffusion modeling, the strategy to generate the trajectories, and the stop criteria and acceptance of the fibers. The local diffusion modeling will depend in part on the type of data acquired, it can be DTI or a HARDI approach. There are different approaches to generate the trajectories, that can have different labels or can be assigned to different classifications and subclassifications, like local or line propagation approach that can be subdivided in deterministic and probabilistic, or the energy minimization techniques that can be subclassified as fast-marching or global approach. Other types of algorithms are machine learning, graph-based, and based on anatomical models. The acceptance criteria refer to when a streamline is correct, when it starts in a region and finishes on another, or when the streamline cross for a specific region of interest. In the following subsections, the local and global tracking is described, as well as the limitations of tractography.

2.4.1 Local tracking

Local tractography algorithms create the streamlines by defining consecutive segments of the streamlines, following the local directions, one at a time in a greedy fashion. This type of method is fast to perform and does not require a lot of computing power but it has some problems. One of these problems is the susceptibility of errors in the local directions that can accumulate and propagate easily along all the streamline and affect the final

reconstruction. Two sub-categories of local tractography are deterministic and probabilistic approaches (Descoteaux et al., 2009).

Deterministic tracking algorithms follow the main diffusion directions in the voxel, which can be described with a single or multi-direction fiber models, performing small successive integration steps. The firsts approaches (Mori et al., 1999; Basser et al., 2000) used the primary diffusion direction (PDD) of the diffusion tensor to trace 3D curves following the diffusion direction. The generation of these 3D curves can be described with the Euler equation

$$\mathbf{r}(s_{i+1}) = \mathbf{r}(s_i) + \alpha\epsilon_1(\mathbf{r}(s_i)), \tag{2.32}$$

where $\mathbf{r}$ is the streamline curve, s_i are the points along the curve, ϵ_1 is the biggest eigenvector used as PDD in the corresponding voxel and the step size α is the length of a segment in the curve. The streamline generation starts from a seeding point and continues till a stop criterion is reached. A seeding point is usually in the white matter or in the interface gray-white matter, and the stop criteria can be based on the FA, coherence with the neighborhood, or previous steps. Higher-order methods, like Runge-Kutta, are used to improve numeric stability (Basser et al., 2000). One of the first implementations of deterministic tractography is the linear propagation method called Fiber Assignment by Continuous Tracking (FACT) (Mori et al., 1999). Another approach uses the anisotropy of the tensor to regulate the effect of the PDD, the tensor deflection approach, where the greater the anisotropy of the tensor, the more reliable the PDD. These deterministic algorithms have been adapted to use HARDI techniques, considering fODF and compartment models. In this case, there are multiple possible directions inside each voxel, extracted from the maximal fODF and direction of the compartment fiber representation. For example, the SD_STREAM algorithm (Tournier et al., 2012) increments the streamlines by stepping along the local orientation that is closest to the current direction of the streamline.

Deterministic tracking is a propagation approach that is easy to perform. Following a deterministic process, for each seed point, segments are added according to fixed directions, creating only one tract for each seed point. This simple process is sensitive to errors in the estimation of the local orientations, that are accumulated and affect the final result.

Probabilistic algorithms consider uncertainty in the orientations of the maximal diffusivity. In the line propagation process approaches, this uncertainty is considered at every step to reconstruct the curve, the orientation

is randomly selected from a probability density function, that can be generated from a tensor or fODF. This consideration allows the algorithms to generate more than one streamline for every seeding point. Those fibers are used to create probability maps, that describe the probability of tracking fibers connecting two regions of interest A and B. This can be done by counting the number of streamlines that cross each voxel. It is also possible to compute the fraction of the random paths that connect the points, and quantify what regions are more like to be connected. An example of a probabilistic algorithm is the iFOD2 (Tournier et al., 2010), which is based on second-order integration over the fODFs. Unlike the first-order integration methods that move along straight-line segments, the iFOD2 algorithm steps along arcs. The arcs are tangent to the current direction of tracking at the current point. The probability of each path is approximated by computing the product of the amplitude of the fODF along the arcs. This is done by creating candidate paths (the arcs) and sampling the fODF along the arcs. A streamline is more probable to follow a path with bigger fODF amplitudes.

Probabilistic tracking tends to generate many streamlines that explore not rigidly the space. This allows more connections among regions of the brain. But it is a propagation approach, and it suffers from the same issues as the deterministic approach, which is susceptible to errors in the local orientations that are used to reconstruct the tracts. Figure 2.13 presents examples of streamlines generated with a deterministic (SD-STREAM) (Tournier et al., 2012) and a probabilistic (iFOD2) (Tournier et al., 2010) algorithm, where can be seen the differences of the tractograms generated with the two types of algorithms described above.

2.4.2 Global tracking

Global tractography approaches try to generate all the trajectories at the same time usually in an energy minimization process (Lemkaddem et al., 2014). These methods try to reconstruct the fibers, that in combination with a forward model, reproduce the reference global data set, e.g., DW-MRI or diffusion profiles. As the optimization is performed globally, these algorithms are more robust in the presence of local diffusion modeling errors, but most of them require a very long computation time (Jeurissen et al., 2017). The tractograms are created from a set of segments, which can have properties like position, orientation, and weight (Reisert et al., 2011). During the optimization process, these segments are changed in such a way they explain the underlying data

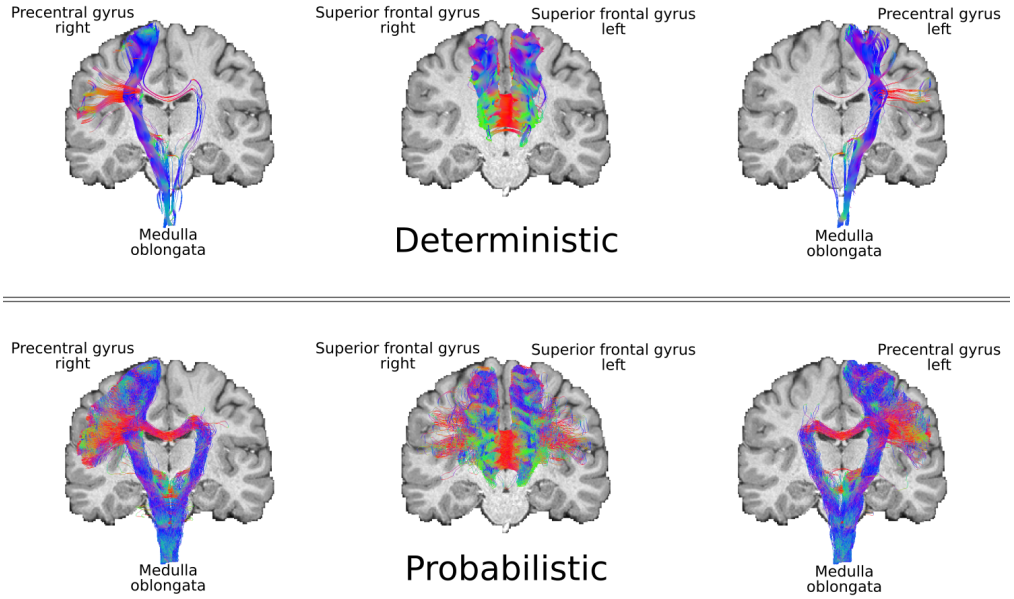

Figure 2.13: **Streamlines generated with local tractography algorithms.** Examples of streamlines generated with local tractography algorithms. In the top row one deterministic (SD-STREAM) and the bottom row one probabilistic (iFOD2). A full brain tractography was performed with both methods and the presented bundles were segmented. The bundles are formed by the streamlines connecting pairs of regions of interest in the cortex, indicated in the labels. It is possible to see that the deterministic streamlines are more smooth than the probabilistic ones, and they cover less volume. This is expected, as probabilistic algorithms generate streamlines with more bends, that tend to explore more space.

and at the same time, connections between them are created, to define the streamlines. A global tractography approach solves the energy problem of the form:

$$E(\{X\}) = \sum_{X} E_{data}(X) + \sum_{(X,Y)\in C} U_{con}(X,Y) + \mu|X|, \tag{2.33}$$

where the *external energy* term E_{data} is related to the differences between the input signal and the signal generated from the segments X in the tractogram. The *internal energy* term U_{con} controls the connection behavior between the connected segments stored in the set C. The *chemical potential* μ is a L_0 penalty that controls the number of particles with the term $\mu|X|$, this term is not always present in all the algorithms. In general, the global algorithms use an external and an internal energy term and usually involve heuristics to create the models and to solve the problem. In this section, some of these strategies will be described.

The Equation 2.33 is used in (Konopleva et al., 2018), which to generate the

signal for the term E_{data} uses a model-free approach. The signal is assumed to be the convolution of the fODF with a microstructural response function (RF). The signal, fODF, and RF are represented in spherical harmonics to find the optimal RF for a fODF proposed, minimizing a quadratic objective function. The term E_{data} is computed as function of the fODF which is represented as a superposition of fiber segments with different orientations and weights. In other algorithms, the signal in term E_{data} is generated with exponential functions (Reisert et al., 2014, 2011; Kreher et al., 2008) or a multi-shell spherical harmonic response function (Christiaens et al., 2015).

In the case of the internal energy term, different heuristics have been proposed trying to build long fibers. In most of the algorithms, the connections between pairs of segment endpoints are created randomly from the set of segments located in a local sphere (neighborhood), i.e., if the endpoints are close enough they may create a connection. In (Reisert et al., 2011) the segments are defined with a tuple $X_i = (x_i, n_i)$, the position of the center of the segment x_i and its orientation n_i. The internal energy term U_{con} of a connected pair is computed as the squared distances of the segment endpoints to the midpoint of a line connecting the centers of the segments, this promotes that the segments stay nearby and keep similar orientations. Other works added some constraints to the shape of the connection like low curvature. This is the case of the spin glass tractography (Mangin et al., 2013) where U_{con} promotes low angular changes between neighborhoods of segments (backward, central, and forward segment).

The position of the segments and their contribution to the signal generation inside each voxel differs in the algorithms. The Gibbs tracking method (Kreher et al., 2008) considers random positions for the segments, modeled as cylinders. One segment can be associated with more than one voxel and one voxel can consider many segments. It takes into account the amount of the segment that is inside each voxel as a volume fraction contribution to the signal generation in that voxel. In the Modelfree global tractography (Konopleva et al., 2018) each segment contributes only in one single voxel, independently of its position inside the voxel, and there is one segment per fiber direction (about three segments in each voxel). To increase the number of segments they divide a voxel into 8 or 27 subvoxels.

This global problem can be seen as Markov Random Fields. To perform the optimization and solve the problem strategies like stochastic optimization (Mangin et al., 2013) and Monte Carlo Markov Chain approaches

combined with the simulated annealing (Metropolis et al., 1953; Lieshout, 1994) and the Gibbs distribution have been used (Konopleva et al., 2018; Reisert et al., 2014; Kreher et al., 2008). The Gibbs distribution, also known as Boltzmann distribution, gives the probability that a system is in a certain state as function of the energy of the state and the temperature of the system. The reversal jump Monte Carlo Markov chain (RJMCMC) (Hastings, 1970; Geyer and Moller, 1994) is a sampler that creates series of configurations according to probabilities functions. It creates a chain of points in the space of all possible configurations, where each element of the chain depends only on its predecessor. Adding a new element means doing an action or transition that can be accepted or rejected. The possible actions are segment birth, segment death, segment move, change connection, and some methods have a segment weight change. Each of these actions can be modeled and has different probability to be performed and accepted. The optimization of the Gibbs sampler is an iterative process that in combination with the simulated annealing allows different probabilities of change depending on the "temperature" of the system. While the optimization process is performed, the temperature is slowly decreased, usually with some heuristics (Kreher et al., 2008). For a certain temperature (ending temperature), when the system reaches an equilibrium or a number of iterations, the whole process stops.

Global tractography is an approach that solves some problems that the local approaches have, but as it was described, the procedure is more complicated and it is not free of errors. One big problem of global tractography is the big number of parameters and the long computational time required. Usually, stochastic optimization procedures are used, but these do not guarantee the convergence to the global optimal solution. In a international competition, the global methods showed similar performance to local approaches (Maier-Hein et al., 2017). The next sections enlist some limitations of tractography and proposals to improve it, like the microstructure informed tractography.

2.4.3 Limitations of tractography

Despite the advantage of describing the brain's WM through tractography, there are technical factors in the acquisition, in the local (voxel) reconstruction models and in tractography algorithms that limit the reconstructions (Thomas et al., 2014). The fibers generated by these algorithms are not truly quantitative and present problems such as partial, duplicates, or omitted fibers (Daducci et al., 2016) as well as false positives, i.e. fibers that are

recovered, but they are not anatomically valid.

In an ex vivo experiment (Thomas et al., 2014) was highlighted that even if very high-quality DW-MRI data (ultra-high-resolution ex vivo DW-MRI of a macaque brain) is used as input to perform tractography, the reconstructed tractograms do not reach the expected anatomical accuracy regardless of the algorithm employed. In particular, this experiment indicated that algorithms that are able to reach high sensitivity (higher rate of true positives) have low specificity (higher rate of false positives) and vice versa. Additionally, it was found in the experiments that anatomical accuracy was highly dependent upon parameters of the tractography, with different optimal values per algorithm for mapping different pathways.

Another work has demonstrated that with current fiber reconstruction methods it is impossible to reach connectomes with both high sensitivity and high specificity (Zalesky et al., 2016). In particular, the conducted analysis highlighted that deterministic tractography algorithms obtain sparse connectomes, incomplete and with false-positive connections; while probabilistic methods obtain denser connectomes, often with low specificity, even though they improve the sensitivity. Then, by analyzing the resulting connectomes, Zalesky et al. (2016) concluded that to investigate the properties of the brain's networks, specificity is twice as important as sensitivity, indeed false-positive connections have a dramatic impact on the network's topology.

An international competition (ISMRM 2015 challenge) was organized to better understand the intrinsic problems of tractography (Maier-Hein et al., 2017). Simulated signals were generated for 25 known bundles of streamlines that represent structures of a realistic brain configuration. These bundles were manually segmented from a whole-brain tractogram of a Human Connectome Project (Glasser et al., 2016) subject to create the ground truth. Most of the algorithms recovered 90% of the true-positive bundles but covered only about one third of their volume. Moreover, all the algorithms recovered many bundles that were not present in the input data (an average of 88 $\pm$58 bundles), even when the ground-truth orientations were used as input for tractography. The major conclusion of this challenge was that trying to infer connectivity from local orientation fields is a fundamental problem in tractography because it is a very ill-posed inverse problem.

Another international competition that took place at the 2018 IEEE International Symposium on Biomedical Engineering (ISBI) conference, challenged the tractography algorithms with three different validation data

sets (Schilling et al., 2019). A macaque data set with a map of known tracer connections, a squirrel monkey data set derived from histological tracer density maps from the same subject, and a 3D physical fiber phantom with manually traced ground-truth pathways. The results of this challenge confirmed problems and limitations of tractography, the anatomical accuracy of tractography is still limited, this was observed in the three independent data sets. The reconstructions that recovered true connections consistently generated a large number of false positives. No one was highly similar to the ground truth, most of them had low connectivity predictive value and low spatial overlap with the true pathways. This work, as previously mentioned above, pointed out that the local orientation and seeding is not enough information, tractography needs more information to overcome the problem of specificity and sensitivity. These works suggested some possible strategies that could improve the reconstructions like: include neuroanatomy priors, e.g., to use microstructural information to better identify from end-to-end the fiber bundles, to apply machine learning techniques that could learn from challenge submissions and ground-truth structures of valid and invalid connections and to incorporate information from different modalities, e.g., myelin and functional contrast.

All these studies exposed the limited anatomical accuracy of tractography, making it clear that the false positives are a big problem that all the tractography algorithms present. These works pointed out that using only the local orientations is not enough, tractography needs more information to overcome the problem of the trade-off between specificity and sensitivity.

2.5 Microstructure informed tractography

Microstructure informed tractography is a research area that combines tractography and microstructural image reconstruction using global optimization techniques in order to generate quantitative structural networks of the brain (Kreher et al., 2008; Sherbondy et al., 2009; Daducci et al., 2016). Currently, it is common that the structural connectivity between gray matter regions of the brain is weighted by the number of streamlines, which is not directly related to the actual underlying neural connectivity (Jones et al., 2013). Microstructure informed tractography tries to recover more biologically oriented estimation of brain connectivity (Daducci et al., 2016).

Global tractography algorithms use microstructure information to

reconstruct all the tracts (Kreher et al., 2008; Fillard et al., 2009; Reisert et al., 2011; Christiaens et al., 2015; Girard et al., 2015). Those are examples of bottom-up approaches that reconstruct all the tractogram at the same time, where the streamlines are generated by the union of small segments distributed over all voxels. These segments are combined with tissue microstructure models to reproduce the signal in the voxels, these methods were described in Section 2.4.2.

Other approaches are the top-down algorithms. This type of algorithm does not build the streamlines, these take as input a tractogram and try to assess their actual contribution and other properties of the tissue, like intra-axonal signal fraction (Schiavi et al., 2020), using also global optimization approaches (Jeurissen et al., 2017). The main concept behind them is that the acquired data DW-MRI can be explained as function of the WM structure described with a tractogram. This section presents and describes some examples of top-down approaches.

2.5.1 Spherical-deconvolution Informed Filtering of Tractograms

The Spherical-deconvolution Informed Filtering of Tractograms (SIFT) method removes streamlines in such a way the streamline density of the filtered tractogram is similar to the fiber density. SIFT does not use directly the DW-MRI, it considers the integral of the fODF proportional to the volume of the tissue inside the voxels, and makes the streamline density close to the fiber density estimated with the spherical deconvolution diffusion model (Smith et al., 2013). Smith et al. (2013) indicate that to hold this property the diffusion signal must not be normalized to the b=0 image intensity, and the resulting fODFs must not be individually normalized, to keep each fODF lobe proportional to the actual underlying tissue volume. This allows that the estimates of fiber population volumes be comparable both between and within voxels. SIFT assumes that each streamline represents some axonal cross-section and contributes uniformly to the tissue volume per unit length.

To perform a comparison between fODF lobe integrals and the streamline density, a proportionality coefficient (μ) is required, which converts the streamline density of each fODF lobe into a value that can be compared with the integral of that lobe. This parameter is the ratio of the total fODF integrals

over all voxels to the corresponding track density:

$$\mu = \frac{\sum_{V} \left(PM_V \sum_{l=1}^{L_V} FOD_{V,l} \right)}{\sum_{V} \left(PM_V \sum_{l=1}^{L_V} TD_{V,l} \right)}, \tag{2.34}$$

where $FOD_{V,l}$ is the fODF integral of lobe l in voxel V, $TD_{V,l}$ is the track density of the lobe l in voxel V, L_V is the total number of fODF lobes in voxel V, and PM_V is the value of the processing mask in voxel V. This value is the square of an estimated WM partial volume fraction. This is an heuristic that restricts the contribution of partial volume contaminated voxels toward the model fit.

Under the consideration that the reconstructed tractogram is not biased, and each streamline represents some volume of axons per unit length, the streamline density will match for all fODF lobes, i.e.:

$$\forall \{V : PM_V > 0, l \geq L_V\} : \mu : TD_{V,l} = FOD_{V,l}. \tag{2.35}$$

This is the ideal case that the SIFT model tries to reproduce, using the cost function f:

$$f = \sum_{V} \left(PM_V \sum_{l=1}^{L_V} \left(\mu TD_{V,l} - FOD_{V,l} \right)^2 \right) \tag{2.36}$$

as metric to quantify how well a streamline reconstruction fits the underlying diffusion data given the model imposed.

To solve the problem SIFT removes streamlines from the data set to improve the model fit. If a streamline is removed the $TD_{V,l}$ will be reduced for the lobes traversed by the streamline and the proportionality coefficient μ will be increased. This change affects the contribution to the cost function from all the fODF lobes within the processing mask. This part is really important in the model because it allows for ongoing valid comparisons between fODF lobe integrals and streamlines densities. The direct quantification of this change will require to recompute the cost function, which would slow down the process. Instead of computing the exact change, SIFT approximates the change with the derivative of the cost functions.

$$\frac{\partial f}{\partial \mu} = 2 \sum_{V} \left(PM_V \sum_{l=1}^{L_v} TD_{V,l} \left(\mu TD_{V,l} - FOD_{V,l} \right) \right) \tag{2.37}$$

To select the streamlines to remove, SIFT computes a gradient vector that contains the estimated change in the cost function per streamline. If the value for a particular streamline is negative (i.e. $\mu TD_{V,l} > FOD_{V,l}$), indicates that the streamline should potentially be removed. Otherwise, if the value is positive (i.e. $\mu TD_{V,l} < FOD_{V,l}$) removing that streamline would likely worsen the quality of the fitting.

The optimal selection of streamlines is a combinatorial optimization problem, with 2^N possible combinations, where N is the number of streamlines in the data set. To find a solution, SIFT uses a gradient descent approach, where streamlines are iteratively removed if this removal improves the cost function value. By doing this the filtered reconstruction will never provide an inferior model fit to the original data.

To select the streamlines to remove, SIFT computes the gradient vector (Eq. 2.37) and sorts it. To remove the potential bias of long streamlines SIFT sorts the vector in order of cost function gradient per unit length. The streamlines are then removed in this order until the gradient vector has to be recomputed or the algorithm ends. The gradient vector is not recomputed after each removal, this would slow down the process. The vector is updated when the difference between the cost function gradient of the streamline to remove and the actual value in the cost function if the streamline is removed is bigger than the actual change in the cost function.

SIFT considers different stop criteria. SIFT will stop when the error cost function gradient of the streamline to remove is smaller than the expected error, that is half of the change in the cost function if the streamline is removed. Another stop criterion is the number of streamlines to keep or the ratio between the cost function change and streamline density change. Figure 2.14 presents the effect of the SIFT algorithm on synthetic data. The streamlines were seeded randomly on the area, the longer bundle has greater volume from which to seed and because of this, it has more streamlines. The fODFs are equivalent in all the voxels of the two bundles, but the normalized streamline density of the longer bundle is bigger than for the shorter one. After applying the filtering algorithm, streamlines in the longer bundle were removed such that the streamline density in both bundles was comparable. This change in the density affected the proportionality coefficient μ, which makes the relative contribution of streamlines to the cost function comparable.

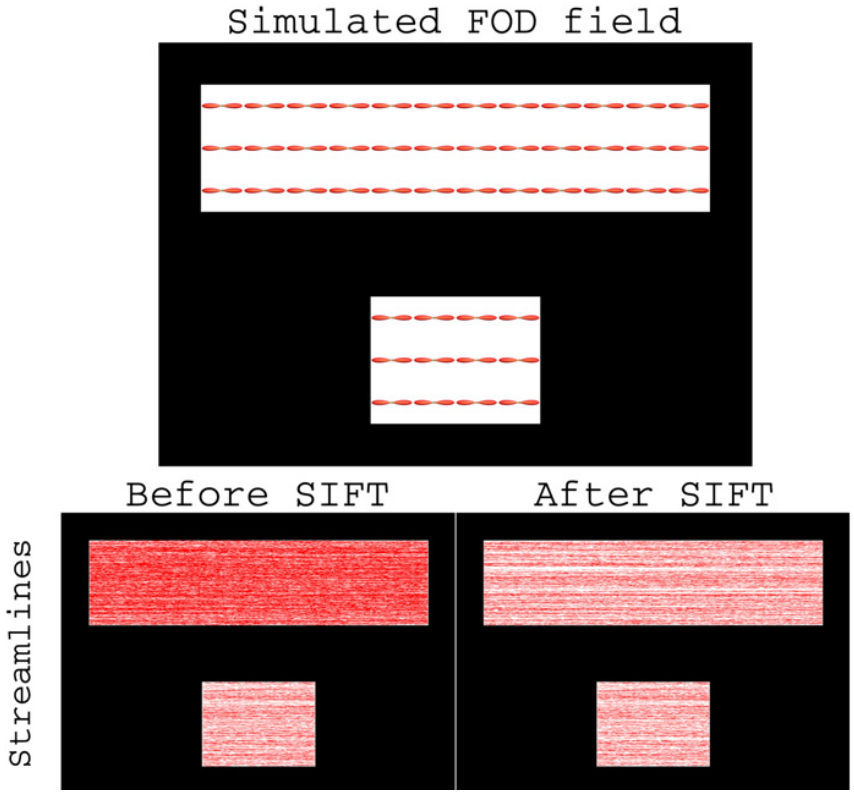

Figure 2.14: **Example of the filtering performed by the SIFT algorithm on synthetic data.** On the top, a simulated fODF field. On the bottom left, 1K probabilistic streamlines seeded randomly in the image (Before SIFT). On the bottom right, the streamlines after the application of the filtering algorithm (After SIFT). Adapted from (Smith et al., 2013)

SIFT2

SIFT2 is an algorithm that overcomes some limitations of SIFT. Similar to SIFT, SIFT2 also uses the integral of the fODF to reproduce the streamline density, but it does not remove streamlines. The goal of SIFT2 is to determine a cross-sectional area for each streamline and to use it as a multiplier in the streamlines connectivity quantification problem (Smith et al., 2015a).

SIFT2 uses a different definition of streamline density, SIFT2 considers a variable contribution (weight) for each streamline:

$$TD_l = \sum_{s:|s_l|>0} (|s_l| \cdot e^{F_s}) \tag{2.38}$$

where TD_l is the track density in fODF lobe l, $|s_l|$ is the length of the streamline s assigned to lobe l, e^{F_s} is the weighting factor, and F_s is the weighting coefficient for the streamline s that traverses lobe l.

Other difference is that the value of the proportionality coefficient μ

estimated with the initial TD_l does not change throughout the execution of SIFT2, which is:

$$\mu = \frac{\sum_{l=1}^{L} (PM_l \cdot FD_l)}{\sum_{l=1}^{L} (PM_l \cdot TD_l^0)}, \tag{2.39}$$

where the index l loops over all the fODF lobes L in the image, FD_l is the fODF lobe integral (fiber density), PM_l is the value of the processing mask (Smith et al., 2013) in the voxel where the lobe l is located, TD_l^0 is the initial sum of streamlines segment lengths (track density) associated to l (Eq. 2.38). In this case, every streamline has a weighting coefficient of zero ($F_s = 0$) and a weighting factor of one, i.e., $e^{F_s} = 1$.

SIFT2 computes a vector of weighting coefficients $\mathbf{F}$ minimizing the cost function:

$$f = \sum_{l=1}^{L} \left(PM_l \left(\mu TD_l - FD_l \right)^2 \right) + A\lambda_{\text{reg}} \sum_{s=1}^{N} \left(f_{\text{reg}}(s) \right), \tag{2.40}$$

where TD_l is the weighted tract density computed as in Eq. 2.38, f_{reg} is a regularization function, A is a scaling parameter that controls the effect of the regularization parameter λ_{reg}, making comparable its effect for different image reconstructions parameters:

$$A = \frac{1}{N} \sum_{l=1}^{L} \left(PM_l \cdot FD_l^2 \right) \tag{2.41}$$

with N the total number of streamlines. There are two regularization functions f_{reg} implemented on SIFT2, a conventional Tikhonov regularization and an asymmetric total variation function. The first one constrains the weighting coefficients F_s to remain close to zero. And the second one constrains the streamlines traversing the same fODF lobes to have similar weights by computing a mean streamline weighting coefficient per fODF lobe F_l^{mean}, which is:

$$F_l^{mean} = \frac{1}{TD_l^0} \sum (|s| \dot{F}_s) \tag{2.42}$$

The optimization problem to solve has high dimensionality due to the number of fODF lobes and streamlines in a normal data set and it is a highly under-determined system. SIFT2 uses an iterative strategy that combines the gradient descent and the expectation-maximization algorithm (Dempster et al., 1977). At every iteration of the algorithm SIFT2 updates the vector $\mathbf{F}$ using

a linear search approach to find a change ΔF_c for each candidate streamline c, that satisfies the expression:

$$\underset{\Delta F_c}{\operatorname{argmin}} \sum_{l:|c_l|\neq 0} \left[\frac{|c_l|}{TD_l^0} PM_l \left(\mu \left(TD_l - |c_l| e^{F_c} + |c_l| e^{F_c + \Delta F_c} + \frac{\delta \theta_l}{\delta F_c} \Delta F_c \right) - FD_l \right)^2 \right] + A\lambda f_{reg}(c), \quad (2.43)$$

where $|c|$ is the length of the candidate streamline c in lobe l. In this equation the density in each traversed fODF lobe was divided into four parts: 1) the streamline density attributed to that lobe given the current weighting coefficient vector $\mathbf{F}$, 2) the subtraction of track density provided by c_l, 3) the density provided by c_l under perturbation of its weighting coefficient, and 4) a correlation term that is computed as

$$\frac{\delta \theta_l}{\delta F_c} = e^{F_c} \left(TD_l^0 - |c_l| \right). \quad (2.44)$$

Then SIFT2 updates the TD_l (Eq. 2.38) and the mean streamline weighting coefficient for each fODF lobe F_l^{mean} and recalculates the cost function f (Eq. 2.40). The iteration continues until the decrease in the cost function between iterations is smaller than a threshold or the maximum number of iterations is reached.

Figure 2.15 presents a comparison of streamlines reconstructions before and after filtering with SIFT and SIFT2 algorithms. It presents an axial slice of the posterior left hemisphere at the level of the forceps major of the corpus callosum, with the streamline densities (top) and streamline reconstructions (bottom). The top left sub-image displays the streamline densities estimated from the raw data with spherical deconvolution. The second column contains the information of the initial reconstruction, all the streamlines are considered to have the same weight and the streamline densities estimated are clearly different from the raw data. The third column displays the results after filtering the streamlines with SIFT, which removes streamlines. In this case, the streamline densities are similar to the ones estimated from the raw data but the streamlines kept were reduced and the reconstruction looks sparse, and it can be too sparse. On the other hand, SIFT2 does not remove streamlines but it estimates a contribution of each streamline to the estimated density, which is also similar to the one computed from the raw data.

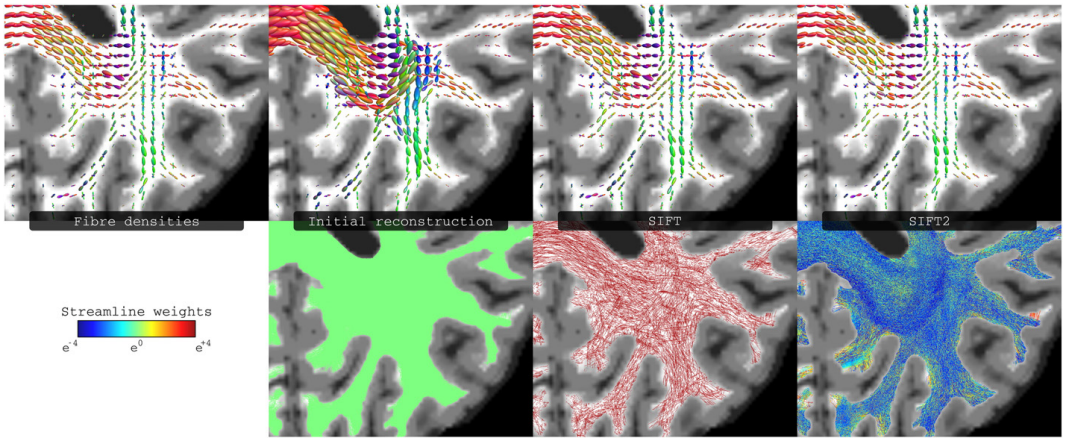

Figure 2.15: **Comparison of the filtering performed by the SIFT2 and SIFT algorithms on in vivo data.** The first row presents the fiber densities estimated from the raw data and from the streamlines reconstructions. The second row presents the streamline reconstructions colored by their weight coefficient, which for the initial reconstruction is zero and for SIFT is $e^{3.7} \approx 41$. Taken from (Smith et al., 2015a).

2.5.2 Linear Fascicle Evaluation

The Linear Fascicle Evaluation (LiFE) algorithm (Pestilli et al., 2014; Caiafa and Pestilli, 2017; Caiafa et al., 2017) combines streamlines with a tensor diffusion model to predict the diffusion data. For each segment of a streamline f a diffusion signal is generated in the direction θ with the equation

$$S(\theta, b) = S_0 e^{bA_f(\theta)} \tag{2.45}$$

for a specific gradient strength b, where S_0 is the signal measured without diffusion weighting and $A_f(\theta)$ is the diffusion coefficient in direction θ:

$$A_f(\theta) = \theta^t \mathbf{D} \theta, \tag{2.46}$$

where $\mathbf{D}$ is a diffusion tensor. The signal in every voxel v is expressed as the weighted sum of a multi-compartment model

$$S_v(\theta, b) = w_0 S_0 e^{-bA_0} + \sum_{f \in v} w_f S_0 e^{-bA_f(0)} \tag{2.47}$$

where $S_v(\theta, b)$ is the signal measured in direction θ for a b-value for the voxel v, A_0 and w_0 are the diffusion coefficient and size compartment respectively for an isotropic compartment, w_f is the size compartment of the streamline f. This function is rewritten as the sum of an isotropic term and the sum of

oriented-dependent functions

$$S_v(\theta, b) = I_v + \sum_{f \in v} w_f O_f(\theta), \tag{2.48}$$

where the isotropic term, I_v, is computed as the mean diffusion signal in the voxel

$$I_v = \frac{1}{N_\theta} \sum_{\theta} S_v(\theta, b), \tag{2.49}$$

and the oriented-dependent function, $O_f(\theta)$, is a Gaussian function centered in zero

$$O_f(\theta) = S_0 \left(e^{-bA_f(\theta)} - \frac{1}{N_\theta} e^{-bA_f(\theta)} \right). \tag{2.50}$$

LiFE solves a set of linear equations minimizing the error in all the voxels to estimate the weights for all the streamlines with the expression

$$\underset{w_f}{\operatorname{argmin}} \sum_{v} \sum_{\theta} \left((S_v(\theta, b) - I_v) - \sum_{f \in v} w_f O_f(\theta) \right), w_f \geq 0, \tag{2.51}$$

the problem is solved using a non-monotonic method for large-scale non-negative least squares (Kim et al., 2013).

2.5.3 Convex Optimization Modeling for Microstructure Informed Tractography

The Convex Optimization Microstructure Informed Tractography (COMMIT) framework (Daducci et al., 2013, 2015; Schiavi et al., 2020; Ocampo-Pineda et al., 2021) is a flexible tool that allows us to combine tractography reconstructions and any additive microstructural signal model to improve the quality of the reconstructions. COMMIT reproduces at the same time the signal in all the voxels of the brain image (global signal), which could be DW-MRI (Daducci et al., 2015) or a microstructural property like the intra-axonal signal fraction (Schiavi et al., 2020). COMMIT estimates the contribution of the streamlines to the global signal by solving a convex problem. It builds a dictionary combining a tractogram and the microstructural models and identifies the linear combination of streamlines that reproduce the observed signal. Depending on the forward models used, different quantitative properties of the tissue can be associated with the streamlines, like axonal diameter or intra-axonal signal fraction.

The formulation considers that for a given tractogram $\mathcal{T}$, the corresponding DW-MRI $\mathbf{I} \in \mathbb{R}_{+}^{n_z \times n_y \times n_x \times n_d}$, composed of n_d q-space measurements acquired over the $n_v = n_z n_x n_y$ voxels, can be modeled as $\mathbf{I} = \mathcal{A}(\mathcal{T}) + \eta$, where $\mathcal{A} : \mathcal{T} \rightarrow \mathbf{I}$ is the linear operator that describes the signal contribution of each streamline to the voxels and η is the acquisition noise. The inverse formulation, for a given input DW-MRI $\mathbf{I}$ finds the set of fibers $\mathcal{T}$ that best describes the data. COMMIT solves the inverse problem, it requires that the input tractogram is a valid superset of the anatomically plausible streamlines, because it does not create streamlines, but it can remove invalid streamlines.

The signal inside each voxel is computed as the linear combination of multi-compartment models (Panagiotaki et al., 2012) of the signal associated with the streamlines that cross the voxel and possibly in addition to local contributions from other tissues, e.g. cerebrospinal fluid. As example, the predicted signal $S(\mathbf{q})$ in a voxel can be expressed as a linear combination with the following general formulation:

$$S(\mathbf{q}) = f^{IC} R^{IC}(\mathbf{q}) + f^{EC} R^{EC}(\mathbf{q}) + f^{ISO} R^{ISO}(\mathbf{q}) \tag{2.52}$$

where R^{IC}, R^{EC}, and R^{ISO} are the predicted signals profiles for the restricted, hindered, and isotropic compartment, respectively, and f^{IC}, f^{EC}, and f^{ISO} the corresponding volume fractions. The predicted signal can be estimated from the data (Tournier et al., 2007) or generated with analytical models (Panagiotaki et al., 2012). This formulation was extended to consider all the tracts traversing the voxel as following:

$$S(\mathbf{q}) = \sum_{s_i \in \mathcal{T}} f_i^{IC} R_{(i)}^{IC}(\mathbf{q}) + \sum_{s_i \in \mathcal{T}} f_i^{EC} R_{(i)}^{EC}(\mathbf{q}) + f^{ISO} R^{ISO}(\mathbf{q}) \tag{2.53}$$

where f_i^{IC} is the global contribution of the restricted diffusion signal associated to the fiber s_i, f_i^{EC} accounts for the hindered space that is around the axons in direction of s_i. Each $R_{(i)}^{IC}$ are the signals profiles R^{IC} rotated to the local orientation (inside the voxels and described with segments) of s_i and scaled by the actual length of s_i that cross the voxel. In the same manner for the $R_{(i)}^{EC}$ functions.

The COMMIT model combines the streamlines and the response functions to implement the mapping $\mathcal{A} : \mathcal{T} \rightarrow \mathbf{I}$ as a linear operator $\mathbf{A}$. The observation model is expressed as a system of linear equations:

$$\mathbf{y} = \mathbf{A}\mathbf{x} + \eta \tag{2.54}$$

where the vector $\mathbf{y} \in \mathbb{R}_+^{n_d n_v}$ concatenates the n_d DW-MRI measurements acquired in the n_v voxels, the matrix $\mathbf{A} \in \mathbb{R}^{n_d n_v \times n_c}$ encodes n_c compartments with the signal associated to all the streamlines in the input tractogram $\mathcal{T}$ and possibly other tissues inside each voxel according to a given multi-compartment model and η accounts for both acquisition noise and modeling errors. The positive weights $\mathbf{x} \in \mathbb{R}_+^{n_c}$ represent the actual contributions of the columns of $\mathbf{A}$, needed to explain the acquired data $\mathbf{I}$.

These weights are estimated solving non-negative least squares problem:

$$\underset{\mathbf{x} \geq 0}{\operatorname{argmin}} \, ||\mathbf{A}\mathbf{x} - \mathbf{y}||_2^2, \tag{2.55}$$

where $|| \cdot ||_2$ is the Euclidean norm in $\mathbb{R}^n$.

The linear operator $\mathbf{A}$, is a big sparse matrix, because each streamline cross only a small portion of the voxels. This operator can be seen as a block matrix, which for a general multi-compartment model is:

$$\mathbf{A} = \left[\mathbf{A}^{IC} | \mathbf{A}^{EC} | \mathbf{A}^{ISO}\right] \tag{2.56}$$

where $n_c = n_r + n_h + n_i$ and the submatrices $\mathbf{A}^{IC} \in \mathbb{R}^{n_d n_v \times n_r}$, $\mathbf{A}^{EC} \in \mathbb{R}^{n_d n_v \times n_h}$ and $\mathbf{A}^{ISO} \in \mathbb{R}^{n_d n_v \times n_i}$ encode, respectively, the n_r restricted, n_h hindered, and n_i isotropic, contributions to the image. This formulation assumes constant microstructural parameter along each trajectory described by each streamline.

The original implementation was done in MATLAB and used tools to solve large-scale non-negative least squares (NNLS) problems(Kim et al., 2013; van den Berg and Friedlander, 2008). The latest version is a homemade Python implementation of the FISTA (Beck and Teboulle, 2009) algorithm.

An illustrative example of the process of the COMMIT framework is presented in Figure 2.16A, which displays a synthetic toy example. The left panel contains the diffusion orientation distribution functions (dODFs) simulated in each voxel, which were used to reconstruct the three streamlines visualized in the middle panel using a generic tractography algorithm. The right panel contains the forward model adopted to construct the matrix $\mathbf{A}$: a "stick" to account for the anisotropic contributions of the streamlines and a "ball" to consider possible CSF contaminations (Panagiotaki et al., 2012). Figure 2.16B illustrates the components of the linear system $\mathbf{y} = \mathbf{A}\mathbf{x}$ to solve using COMMIT. The column vector $\mathbf{y}$ concatenates the data simulated in each voxel. The matrix $\mathbf{A}$ is constructed by first checking how the reconstructed streamlines intersect the voxels: fiber 1 crosses voxels 1 and 2, fiber 2 crosses

voxels 1 and 3; fiber 3 crosses voxel 2, 3, and 4. It then creates one column for each streamline and stores in the rows corresponding to each voxel it traverses the contribution of a stick oriented in the same direction of the streamline; if a streamline does not cross a voxel, the corresponding rows are set to 0. To account for the possible presence of CSF in a voxel it adds four columns and, in each of them, it puts 0 everywhere except in the rows corresponding to a distinct voxel where it inserts an isotropic contribution according to the ball model.

Every column in $\mathbf{A}$ is controlled by a different contribution in $\mathbf{x}$ and, for a given configuration of contributions $\mathbf{x}$, the predicted signal is obtained by performing the multiplication $\mathbf{Ax}$. COMMIT seeks for the optimal configuration of $\mathbf{x}$, which must be positive, such that the predicted signal, i.e. $\mathbf{Ax}$, is as close as possible to the measured signal, i.e. $\mathbf{y}$, hence it tries to minimize their difference, i.e. argmin $||\mathbf{Ax} - \mathbf{y}||_2^2$. According to matrix-vector multiplication properties, we can immediately notice that to obtain the correct profile in voxel 1, we must have a positive contribution in the first two entries of $\mathbf{x}$ but 0 in $\mathbf{x}_4$ since there is no CSF in voxel 1. To assign the values to the remaining entries of $\mathbf{x}$ we continue the multiplication. Looking at voxel 2 we observe that $\mathbf{x}_3 = \mathbf{x}_5 = 0$, while from the third and fourth voxels we obtain $\mathbf{x}_6 = 0$ and $\mathbf{x}_7 = 1$ respectively. The entries of $\mathbf{x}$ are uniquely determined and, since $\mathbf{x}_3 = 0$, fiber 3 is marked as false positive and removed from the tractogram.

2.6 Comprehensive map of neural connections in the brain

The study of the neuronal architecture of the brain has benefited from the use of tractography. Tractography represents the major WM pathways of the brain using polylines called streamlines, this can be done in vivo and noninvasively. These streamlines build a wired diagram that describes the structural connectivity of the brain and can be used to create a comprehensive map of the neural connections in the brain, this map is called *connectome* (Hagmann, 2005; Sporns et al., 2005). Modeling each neuron as a node in practice is not possible (Telesford et al., 2011), instead, the structural connectome describes the connections between the cortical areas and subcortical nuclei, called regions of interest (ROIs). With this formalism, it is possible to investigate with graph theory (Bullmore and Sporns, 2009;

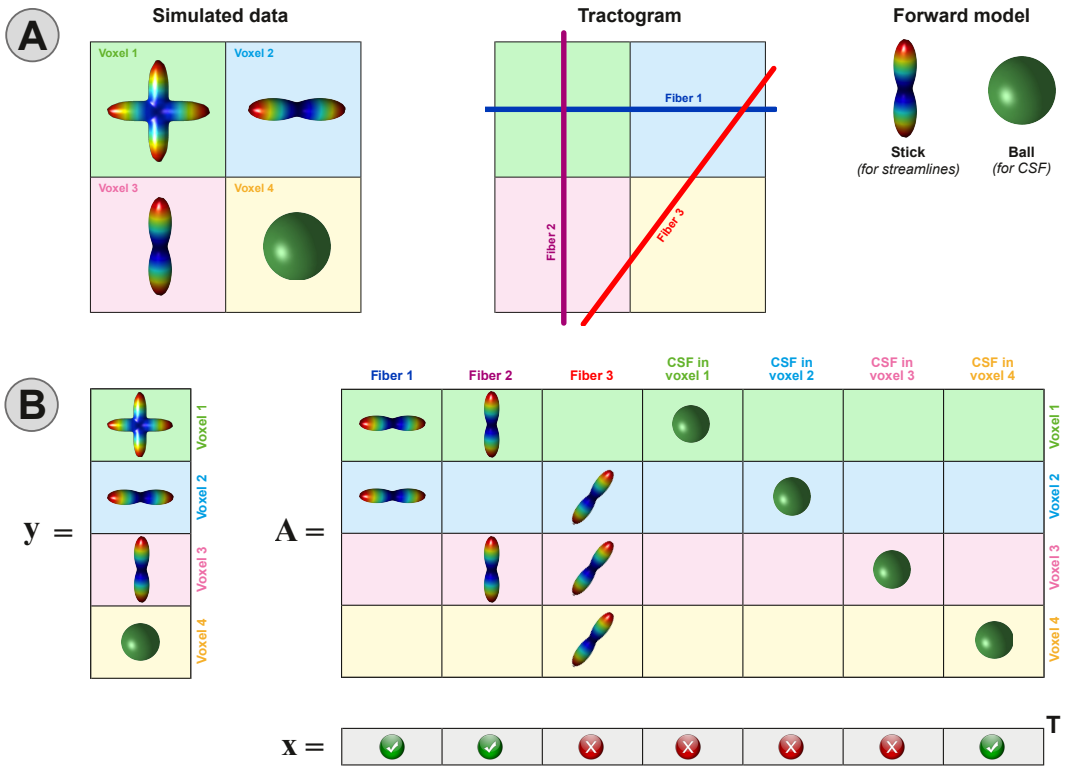

Figure 2.16: **Synthetic toy example to illustrate the modeling and the parameter estimation used by the COMMIT framework.** (**A**) The simulated orientation distribution functions (ODFs), a possible tractogram estimated with a generic tractography algorithm, and the forward model used to associate a signal contribution to each streamline. (**B**) The corresponding vector $\mathbf{y}$ containing the simulated data in all voxels, the matrix $\mathbf{A}$ encoding the signal contributions of each streamline according to the chosen forward model (as well as the potential presence of CSF) and the coefficients $\mathbf{x}$ estimated by COMMIT.

Bullmore and Bassett, 2011; Bassett and Sporns, 2017) differences of the connectivity due to biological differences or neurological conditions to perform diagnosis (Bassett and Bullmore, 2009; Griffa et al., 2013; Alexander-Bloch et al., 2013; Ingalhalikar et al., 2014; Valk et al., 2015; Smith et al., 2019).

An important part in the creation of the connectomes is the definition of the ROIs (Sotiropoulos and Zalesky, 2019), that is how the GM is segmented and as consequence the streamlines in WM. There are different approaches, some of them use templates to map regions associated with anatomical regions (Desikan et al., 2006; Gong et al., 2009; Destrieux et al., 2010), others divide the cortex in random equi-surface patches (Bastiani et al., 2012; Hagmann et al., 2007). Other approaches proposed hierarchical structured organizations of the cortex for investigating the connectivity at different scale

sizes (Cammoun et al., 2012).

Once the parcellation has been defined, to create the connectome, the tractogram is segmented based on the intersection of the streamlines and the ROIs. Fibers that do not intersect the ROIs are not considered in the creation of the connectome. Due to the partial volume in the interface of WM and GM, many of the streamlines in a tractogram do not reach an ROI. One heuristic proposed to reduce the number of streamlines discarded is to assign each streamline termination to the nearest ROI within a search radius (Smith et al., 2015b), e.g., 2mm.

To summarize the creation of a connectome, Figure 2.17 presents a general scheme of the process. First, a morphological T1-weighted image is used to segment the brain and identify cortical and subcortical GM structures to define the ROIs used as nodes. In another step, using DW-MRI, a tractography is generated to define the pathways of the structural connectivity. Then, the image with the ROIs (in the same space as the T1-weighted) and the tractogram (usually in the same space as DW-MRI) are registered and aligned, and the intersections of the streamlines endpoints and the ROIs define the connectivity matrix. The combination of these image modalities with other strategies like spectroscopic imaging, or regional activation and co-activation data, e.g. magnetoencephalography, may offer a more feasible strategy for mapping the human connectome (Sporns et al., 2005).

The definition of "connection strength" of the connectivity matrix and how to assign weights are still open questions (Jones et al., 2013). Although some studies that compared tractography with tract-tracing data proved that connectome reconstructions based on the number of streamlines represent a fairly realistic proxy for the connection strength of white matter projections (van den Heuvel et al., 2015; Delettre et al., 2019), the streamline count should not be confused with the actual fiber count (Jones et al., 2013). Notably, since network models rely on the underlying choices of what an edge represents, the accuracy of tractography reconstructions as well as how it is assigned a contribution to the streamlines become crucial.

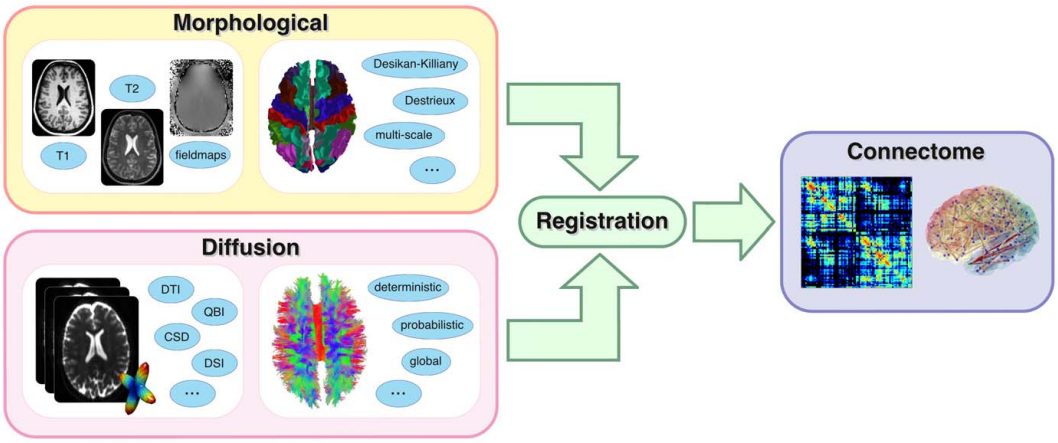

Figure 2.17: **Workflow to map the structural connectivity of the brain.** To create a connectome it is required to combine information from morphological images (T1, T2, and field maps) and DW-MRI. The morphological images are used to identify anatomical areas and divide the cortical and subcortical areas into regions of interest. The DW-MRI is used to create the tractography, that represents the structural connectivity in the brain. Both results are registered and merged to create the connectivity matrix, also called connectome. Figure taken from (Daducci et al., 2012)

Chapter 3

In vivo tractography evaluation methodology

This section presents a strategy developed to evaluate tractography reconstructions using a bundle segmentation tool called RecobundlesX (Rheault, 2020), and models of plausible and implausible bundles. To study and evaluate tractography reconstructions, a common practice is to divide them into bundles that represent WM fascicles. This is a complicated task that requires knowledge of Neuroanatomy and is not an exact procedure. There is variability among segmentations performed by experts (Rheault et al., 2020a), and up to now, there is not a ground truth for *in vivo* tractography to validate the reconstructions (Dyrby et al., 2007; Côté et al., 2013). Virtual dissection is the procedure by which specific WM fascicles are described or represented through bundles of streamlines, segmented, and selected based on the anatomical knowledge (Catani et al., 2002). The virtual dissection is used to study the shape of the bundles (Batchelor et al., 2006), quantify properties like the volume, or estimate quantitative metrics of them, e.g. tractometry (comprehensive assessment of microstructure metrics along WM tracts) (Bells et al., 2011; Cousineau et al., 2017) and profilometry (framework that joins multiple metrics along the WM tracts) (Yeatman et al., 2012; Dayan et al., 2016). One approach of bundle segmentation groups streamlines based on anatomical priors, using inclusion and exclusion regions of interest (ROIs). These ROIs can be defined based on known structures like gray nuclei, gyri, or sulci. This segmentation can be a manual procedure, where a person uses anatomical knowledge to define the ROIs, usually following a clearly defined set of rules and by doing visual inspection to group streamlines with the expected shape. The definition of the rules and

ROIs is not an easy task, as neither is the segmentation. Other segmentation procedures are automatic approaches, that also follow a set of rules, but the procedure is performed by an algorithm, and not by a person. These approaches can use atlases created based on anatomical landmarks to define a dissection plan, or model, to be used by the software (Garyfallidis et al., 2018; Guevara et al., 2012).

3.1 RecobundlesX

RecobundlesX (Rheault, 2020) is a robust multi-atlas, multi-parameter bundle segmentation tool that uses bundle models as references to identify and segment automatically bundles in tractography reconstructions. It uses the method RecoBundles (Garyfallidis et al., 2018) that is an algorithm that uses bundle models as shape priors for detecting and segment similar streamlines in a tractogram. This procedure is computationally demanding for data sets of millions of streamlines, which are commonly used. To reduce the dimension of the problem of comparing all the streamlines in the models (hundreds) with all the streamlines in a tractogram (millions) to select the streamlines, RecoBundles clusters the streamlines and works with the centroids of the clusters. The centroids are created using the implementation of QuickBundlesX (Garyfallidis et al., 2016), which is an accelerated version of the algorithm QuickBundles (Garyfallidis et al., 2012), an unsupervised clustering algorithm that uses a threshold on distance metrics to group the streamlines. Once the centroids were created, RecoBundles uses the Streamline-based Linear Registration (SLR) (Garyfallidis et al., 2015) to register the centroids of the models and the tractogram to perform the comparison among them. This procedure has a big variability in the results, generated by the clustering configurations used, in addition to the registration of the models and the tractogram.

To reduce this variability, RecobundlesX takes into account multi-atlas models, multi-parameters clustering, and a voting scheme that generates more stable solutions. The segmentation method supports the use of multiple models of the same bundle as input. These models can be generated from different subjects, with different tractography algorithms, and segmented by different experts, to cover more variability in the definition of the bundles. It also allows us to use different configurations of the segmentation parameters, e.g. clustering threshold, number of iterations for SLR, type of transformation,

pruning, etc, to cover more variability in the segmentation procedure. RecobundlesX combines the results of the multi-atlas and multi-parameters segmentation using a voting system, that merges the multiple segmentation performed for each bundle definition.

To use RecobundlesX[1] different parameters have to be set for the bundles used as models, for the tractography reconstructions, and for the merging procedure. The parameters used for the models are specified in a *JSON* file with the fields:

- *model_clustering_thr*, specifies the threshold(s) used to perform the clustering with QuickBundlesX,
- *bundle_pruning_thr*, minimum average direct-flip (MDF) distance threshold(s) used for the final streamlines selection,
- *slr_transform_type*, SLR to register the streamlines of the models and the subjects, the options are: translation, rigid, similarity, and scaling.

For the tractography reconstructions the parameters are:

- *tractogram_clustering_thr*, that specifies the threshold used to cluster the streamlines, the implementation uses the function *qbx_and_merge* that performs a tree clustering, to speed up the execution of the clustering, and considers as top levels the thresholds [45, 35, 25, 15] in addition to the one specified; and
- *seeds*, which are the random number generator seeds used to perform the clustering.

And for the merging procedure:

- *multi_parameters* specifies the maximum number of executions of Recobundle to perform, and
- *minimal_vote*, is used as a threshold to keep a streamline, i.e., only if a streamline is recognized at least this number of times, will be considered for saving.

[1] `https://github.com/scilus/scilpy/blob/master/scripts/scil_recognize_multi_bundles.py`

3.2 Creation of true- and false-positive bundle models

True-positive bundle models. Subjects 193441, 219231, 286650, 486759, and 615441 from the Human Connectome Project (HCP) (Essen et al., 2013) were used. Tractography reconstruction was performed and 37 major bundles were manually segmented. These bundles can be identified as association, commissural, or projection fibers. The association fiber bundles, presented in Figure 3.1, are: arcuate fasciculus, inferior frontal occipital fasciculus, uncinate fasciculus, cingulum, inferior longitudinal fasciculus, and superior longitudinal fasciculus (SLF); this last was divided into three bundles SLF_I, SLF_II, and SLF_III. The commissural fiber bundles segmented are part of the corpus callosum (CC) that was divided into eight parts: CC_1, CC_2a, CC_2b, CC_3, CC_4, CC_5, CC_6, and CC_7, which are presented in the Figure 3.2. The projection fibers are presented in Figure 3.3, they are middle cerebellar peduncle, optic radiation, superior cerebellar peduncle, corona radiata, and cortico-spinal tract; for the last two, two different versions were considered, in one version the streamlines arrive at the bottom part of the brainstem (medulla oblongata), while in the other version the streamlines stop before. We decided to use these two models because the endpoints of the streamlines influence notably the recognition process, and it is common to find in the tractography reconstructions streamlines that stop in different parts of the brainstem. The true-positive bundle models are available in (Rheault, 2021).

False-positive bundle models. The submitted tractograms to the ISMRM 2015 Tractography Challenge were used to select the false-positive bundles. In the study performed by Maier-Hein et al. (2017) several bundles from the submitted tractograms were labeled as false positives because they were not in the ground-truth tractogram. A quality control was performed on these bundles to select those with the most anatomical implausible trajectory. From these bundles, 44 were selected and refined to obtain smooth and well-defined bundle models (Rheault, 2020). To obtain the models from the bundles, we processed them using the toolbox *scilpy*[2] of the Sherbrooke Connectivity Imaging Laboratory (SCIL) of University of Sherbrooke in Canada. The processing includes:

[2] `https://github.com/scilus/scilpy`

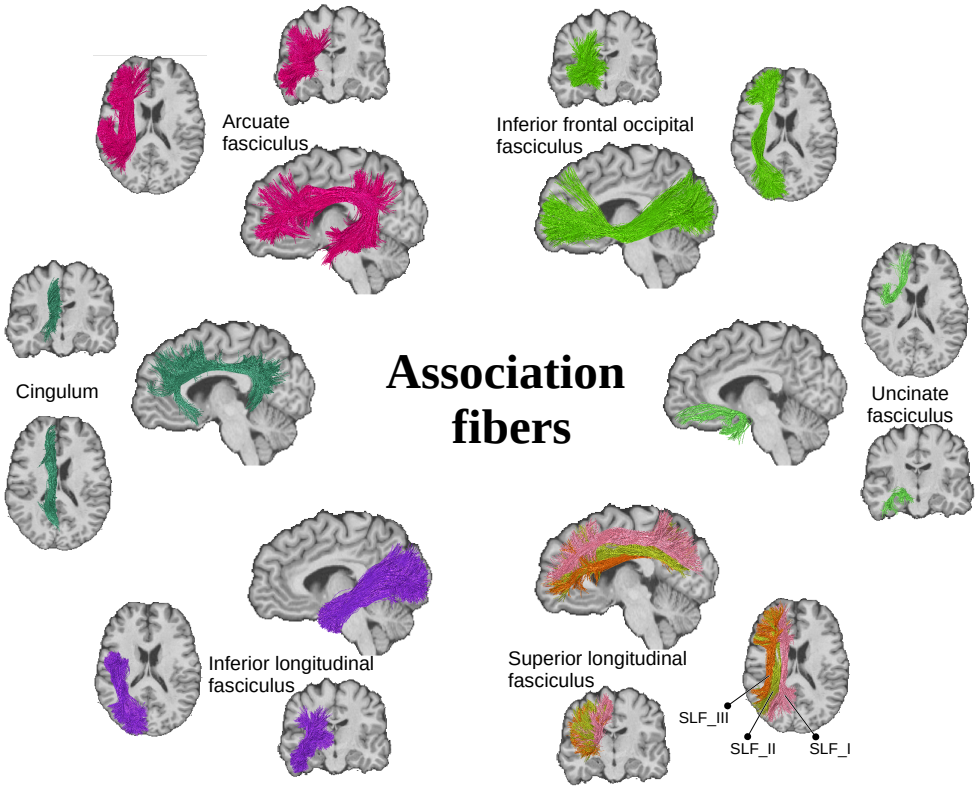

Figure 3.1: **Bundle models of association fibers** from the subject 193441 used as true-positive models. Each model is presented from three views: sagittal, axial, and coronal. The bundles presented are: arcuate fasciculus, inferior frontal occipital fasciculus, uncinate fasciculus, cingulum, inferior longitudinal fasciculus, and superior longitudinal fasciculus (SLF); this last was divided in three bundles (SLF_I, SLF_II, and SLF_III) presented with different colors.

- smooth them with the function *scil_streamline_spline_smooth.py* parameters *control_point_ratio*=0.25 and *segment_len*=4.0 to eliminate small oscillations, and with parameters *control_point_ratio* = 0.50 and *segment_len*=1.0 to smooth bending;
- eliminate loops with the function *scil_detect_streamlines_loops.py* with default parameters; and
- remove outliers with the function *scil_outlier_rejection.py* with parameter *alpha*=0.4.

The parameters used can be different depending on the bundles. The parameters presented here were selected based on a visual inspection. Figure 3.4 presents a representative bundle selected to be a false-positive bundle model before and after the processing. Figure 3.5 displays the 44

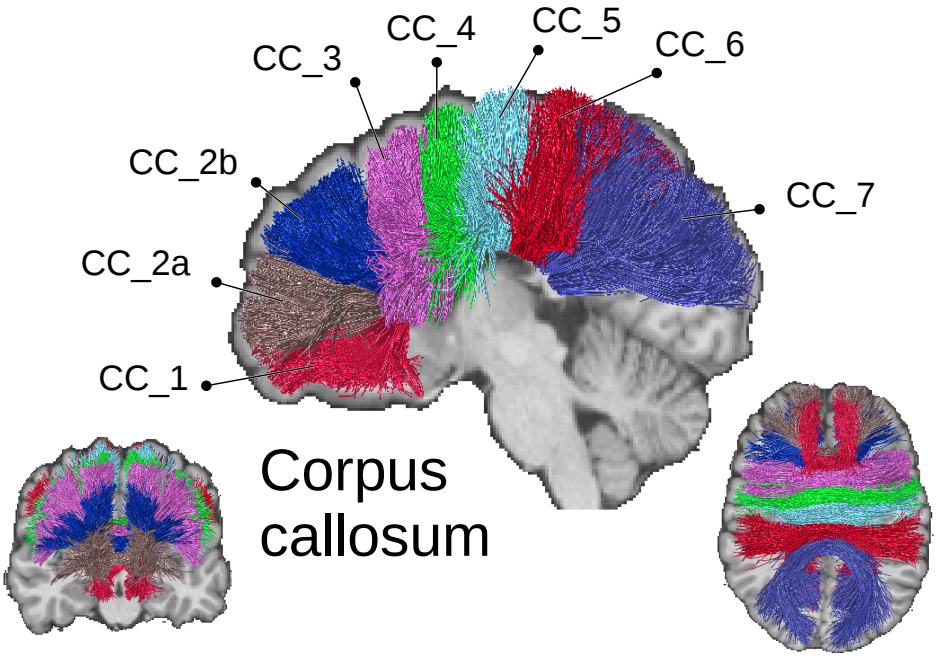

Figure 3.2: **Bundle models of the corpus callosum** from the subject 193441 used as true-positive models. The corpus callosum was divided in eight bundles, labeled as: CC_1, CC_2a, CC_2b, CC_3, CC_4, CC_5, CC_6, and CC_7. The bundles are presented from the sagittal, coronal, and axial view.

false-positive bundle models used in the processing. It is important to note that some of these bundles are similar among them and they may overlap. The false-positive bundle models are available in (Ocampo-Pineda, 2021).

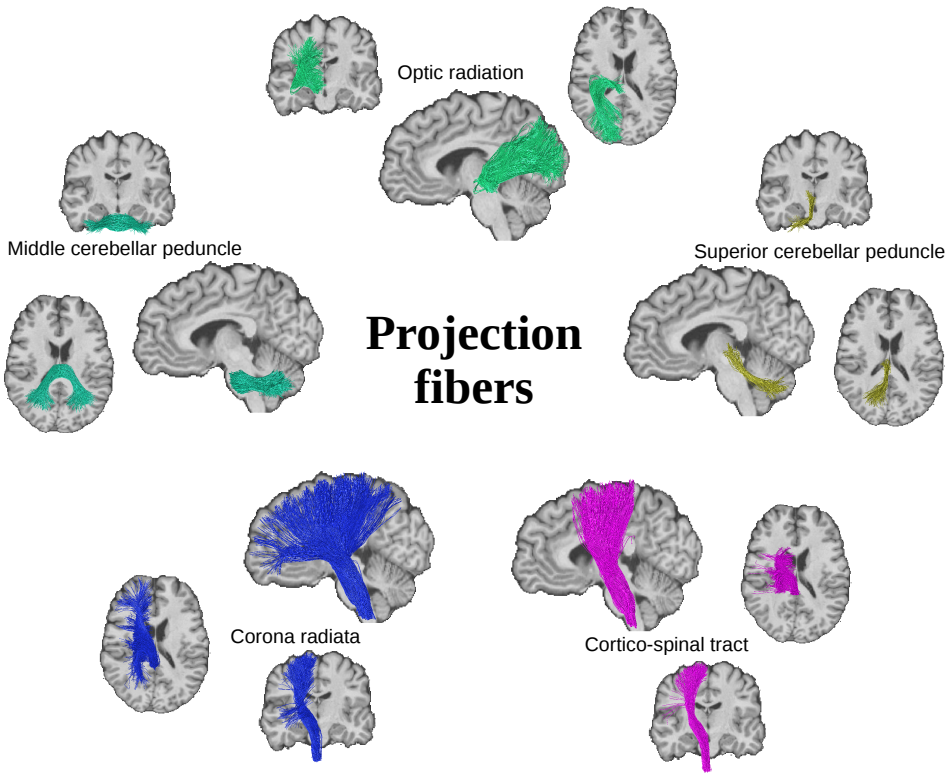

Figure 3.3: **Bundle models of projection fibers** from the subject 193441 used as true-positive models. Each model is presented from three views: sagittal, axial, and coronal. The bundles presented are: middle cerebellar peduncle, optic radiation, superior cerebellar peduncle, corona radiata, and cortico-spinal tract.

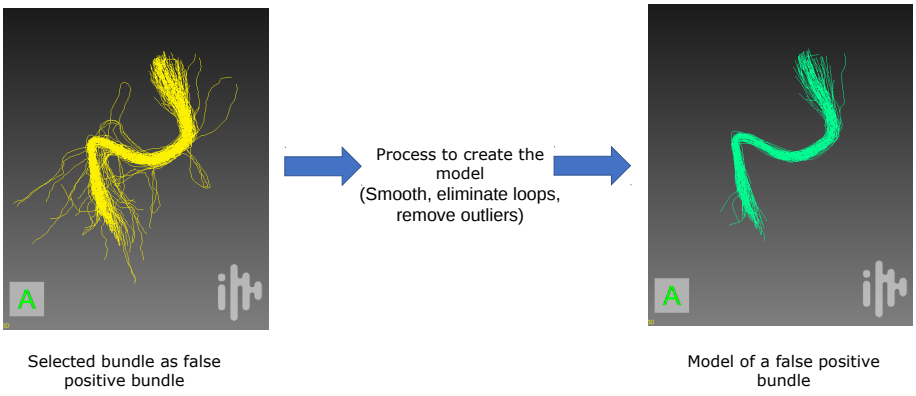

Figure 3.4: **Process to create a false-positive bundle model.** Representative false-positive bundle before (left) and after processing (right) to be a false-positive model. The bundle selected was smoothed, the streamlines that describe trajectories with loops were eliminated, and outliers streamlines were removed. The streamlines obtained after the process will be used as a model to recognize the bundle.

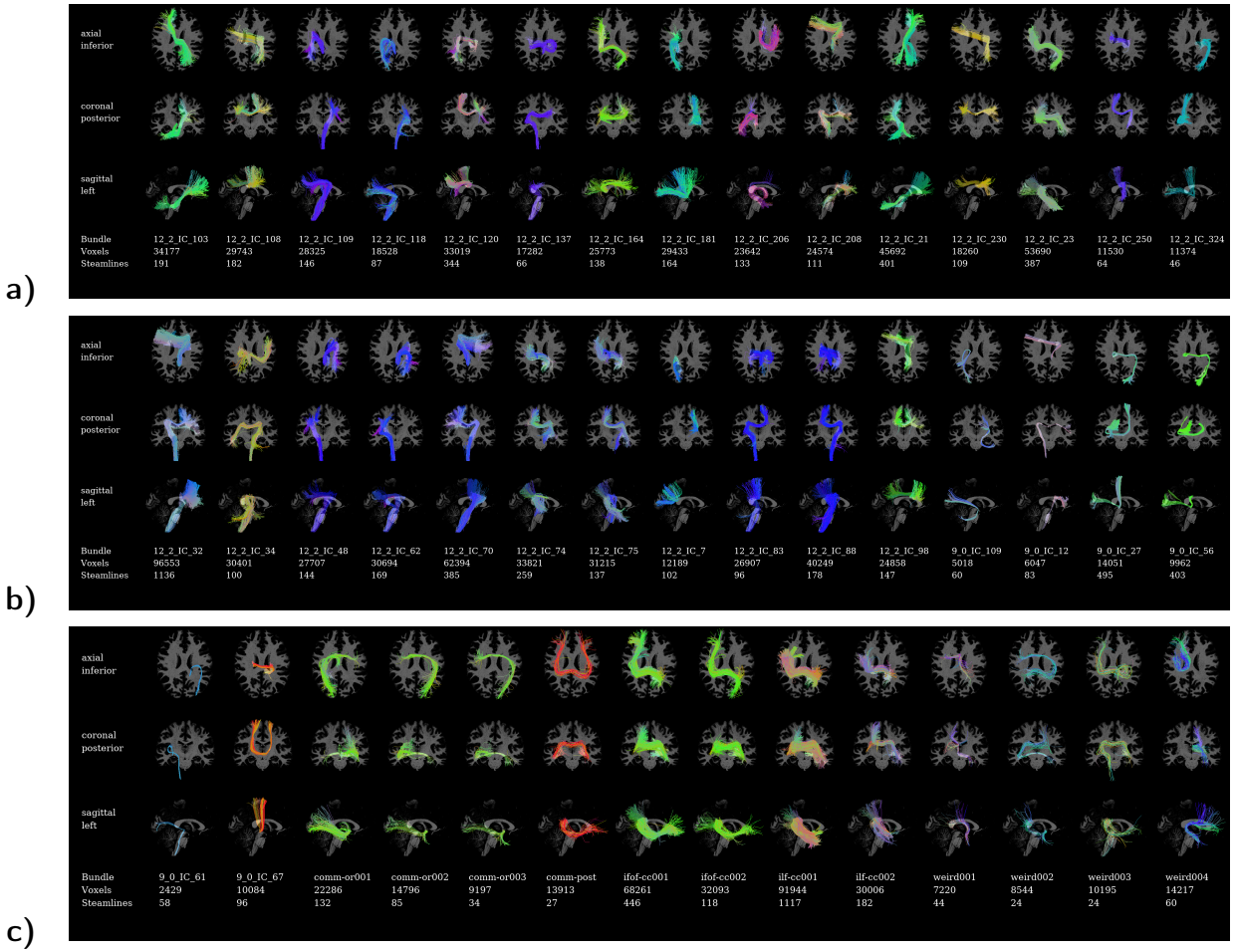

Figure 3.5: **Bundle models used as false-positive models** presented in three panels **a)**, **b)**, and **c)**. Each panel displays three different views of the bundles, axial inferior (first), coronal posterior (second), and sagittal left (third). For each bundle is presented: name, number of voxels covered, and number of streamlines in the model.

3.3 Bundle segmentation

This section describes an example of the bundle segmentation procedure used to create a gold standard set of bundles. The data set used corresponds to subject 100307 from the HCP repository[3]. The processed diffusion data and the structural T1-weighted image described in (Essen et al., 2013) were used to perform the whole brain Anatomically Constrained Tractography (ACT) (Smith et al., 2012).

We used nine different parameter configurations for RecobundlesX. In the case of true positives, we have models from five different subjects, that give us 45 different executions of RecobundlesX per model. The 37 true-positive bundle models and the corresponding bundles are listed in Table 3.1. The parameter configuration used for each model is presented in Tables 3.2 and 3.3. For the false positives, there is only one model per bundle, and for all the models the parameters used were:

- *model_clustering_thr* = [2, 3, 4]
- *bundle_pruning_thr* = [8, 7, 6]
- *slr_transform_type*: "similarity"

which were good compromises among the models used. The threshold used to cluster the input tractogram was *tractogram_clustering_thr* = 8. Only one *seed=0* was used. To perform one execution of Recobundle per parameter configuration, the parameter *multi_parameters* was set to 45 for the true positives and to 9 for the false positives. Then, the *minimal_vote* required to consider a streamline in a bundle was set to 1, and the number of occurrences for each streamline in each bundle was saved, to apply a threshold in a further step.

Although RecoBundeX adds robustness to the segmentation process, there is still variability and, it is possible that one streamline is recognized and assigned to more than one model, or even it can be labeled as true and false positive at the same time. To deal with that, we removed the intersections. First, the intersection between true and false positives was removed, i.e., if a streamline had been selected as true and false positive, this was considered only true positive. Then, to remove the intersections within the true and false positives, the bundles were sorted in descending order by number of streamlines, and the streamlines that appear in more than one bundle were removed, keeping only the first occurrence.

[3] `https://www.humanconnectome.org`

Once there are no duplicate streamlines in the bundle segmentation, we removed the streamlines with occurrences below a threshold of 75%, that is, we kept the streamlines that were assigned to a bundle 35 times of 45 experiments for the true positives and 7 times of 9 executions for the false positives. The use of this threshold caused that some of the false-positive bundles, with trajectories difficult to match with the trajectory of most models, to lost all the streamlines, and those bundles were removed from the study. An additional processing was performed on some true-positive models. The bundle models SLF_I, and SLF_II, and SLF_III were merged in one SLF, right and left, respectively. These bundle models were very similar to each other, because of this, many streamlines were selected in more than one cluster and by removing the intersections some groups were left empty, to avoid this we merged them into one. The same procedure was performed to CST with CST_cut and to CR with CR_cut. In these cases, they were merged because they were two versions of the same bundles. The bundles '_cut' contain streamlines that ended in the middle of the brainstem, near to the midbrain and the pons. The streamlines in the other bundle, ended in the bottom of the brainstem, near to the medulla oblongata. At the end, 29 bundles were used as true positive in the gold standard segmentation.

Figures 3.6 and 3.7 display the true- and false-positive bundles, respectively, segmented with the procedure described in this section. In general, the bundles are well defined and match the models used. The figures present in the first column the name of the visualization planes that are: axial inferior, coronal posterior, and sagittal left. The last row presents for each bundle an identification name, voxel covered, and number of streamlines in the bundle. The names for the true-positive bundles are the same described in Table 3.1 for the models, with the exception of SLF, CR, and CST, for which their merged versions are presented.

Panel a)	
Short name	**Name**
AF_L_m	Arcuate fasciculus
AF_R_m	
CC_1_m	Corpus callosum
CC_2a_m	
CC_2b_m	
CC_3_m	
CC_4_m	
CC_5_m	
CC_6_m	
CC_7_m	
CG_L_m	Cingulum
CG_R_m	
CR_L_m	Corona radiata long streamlines
CR_R_m	
CR_L_cut_m	Corona radiata short streamlines
CR_R_cut_m	
SCP_L_m	Superior cerebellar peduncle
SCP_R_m	

Panel b)	
Short name	**Name**
CST_L_m	Cortico-spinal tract long streamlines
CST_R_m	
CST_L_cut_m	Cortico-spinal tract short streamlines
CST_R_cut_m	
IFOF_L_m	Inferior frontal occipital fasciculus
IFOF_R_m	
ILF_L_m	Inferior longitudinal fasciculus
ILF_R_m	
MCP_m	Middle cerebellar peduncle
OR_L_m	Optic radiation
OR_R_m	
SLF_1_L_m	Superior longitudinal fasciculus
SLF_1_R_m	
SLF_2_L_m	
SLF_2_R_m	
SLF_3_L_m	
SLF_3_R_m	
UF_L_m	Uncinate fasciculus
UF_R_m	

Table 3.1: **Name of the bundle models used as true positives**. Name of the true-positive bundle models used. The short names contain some common letters: R (right), L (left), and m (model). The numbers are used to identify different sub-bundles in which the bundle was divided. Short names are used in Tables 3.2 and 3.3 to specify the configuration used to create each model.

Bundle	***model_ clustering_ thr***			***bundle_ pruning_ thr***			***slr_ transform_ type***
AF_L_m	3.5	3.75	4	8	7	6	similarity
AF_R_m	3.5	3.75	4	8	7	6	similarity
CC_1_m	3	3.5	3.75	8	7	6	similarity
CC_2a_m	3	3.5	3.75	8	7	6	similarity
CC_2b_m	3	3.5	3.75	8	7	6	similarity
CC_3_m	3	3.5	3.75	8	7	6	similarity
CC_4_m	3	3.5	3.75	8	7	6	similarity
CC_5_m	3	3.5	3.75	8	7	6	similarity
CC_6_m	3	3.5	3.75	8	7	6	similarity
CC_7_m	3	3.5	3.75	8	7	6	similarity
CG_L_m	3	3.5	3.75	7	6	5	similarity
CG_R_m	3	3.5	3.75	7	6	5	similarity
CR_L_m	2	2.5	3	8	7.5	7	similarity
CR_R_m	2	2.5	3	8	7.5	7	similarity
CR_L_cut_m	2	2.5	3	8	7.5	7	similarity
CR_R_cut_m	2	2.5	3	8	7.5	7	similarity
SCP_L_m	3	3.5	3.75	8	7	6	similarity
SCP_R_m	3	3.5	3.75	8	7	6	similarity

Table 3.2: **Parameter configuration used in RecobundlesX per each bundle presented in panel a) of Table 3.1**. Three different values were used for the parameters *model_ clustering_ thr* and *bundle_ pruning_ thr*, and one for *slr_ transform_ type*, which produce nine configurations.

Bundle	***model_ clustering_ thr***			***bundle_ pruning_ thr***			***slr_ transform_ type***
CST_L_m	2	2.5	3	8	7.5	7	similarity
CST_R_m	2	2.5	3	8	7.5	7	similarity
CST_L_cut_m	2	2.5	3	8	7.5	7	similarity
CST_R_cut_m	2	2.5	3	8	7.5	7	similarity
IFOF_L_m	3.5	3.75	4	8	7	6	similarity
IFOF_R_m	3.5	3.75	4	8	7	6	similarity
ILF_L_m	2	2.5	3	8	7.5	7	similarity
ILF_R_m	2	2.5	3	8	7.5	7	similarity
MCP_m	2	2.5	3	8	7.5	7	similarity
OR_L_m	2	2.5	3	8	7.5	7	similarity
OR_R_m	2	2.5	3	8	7.5	7	similarity
SLF_1_L_m	2	2.5	3	8	7.5	7	similarity
SLF_1_R_m	2	2.5	3	8	7.5	7	similarity
SLF_2_L_m	2	2.5	3	8	7.5	7	similarity
SLF_2_R_m	2	2.5	3	8	7.5	7	similarity
SLF_3_L_m	2	2.5	3	8	7.5	7	similarity
SLF_3_R_m	2	2.5	3	8	7.5	7	similarity
UF_L_m	2	2.5	3	8	7.5	7	similarity
UF_R_m	2	2.5	3	8	7.5	7	similarity

Table 3.3: **Parameter configuration used in RecobundlesX per each bundle presented in panel b) of Table 3.1**. Three different values were used for the parameters *model_ clustering_ thr* and *bundle_ pruning_ thr*, and one for *slr_ transform_ type*, which produce nine configurations.

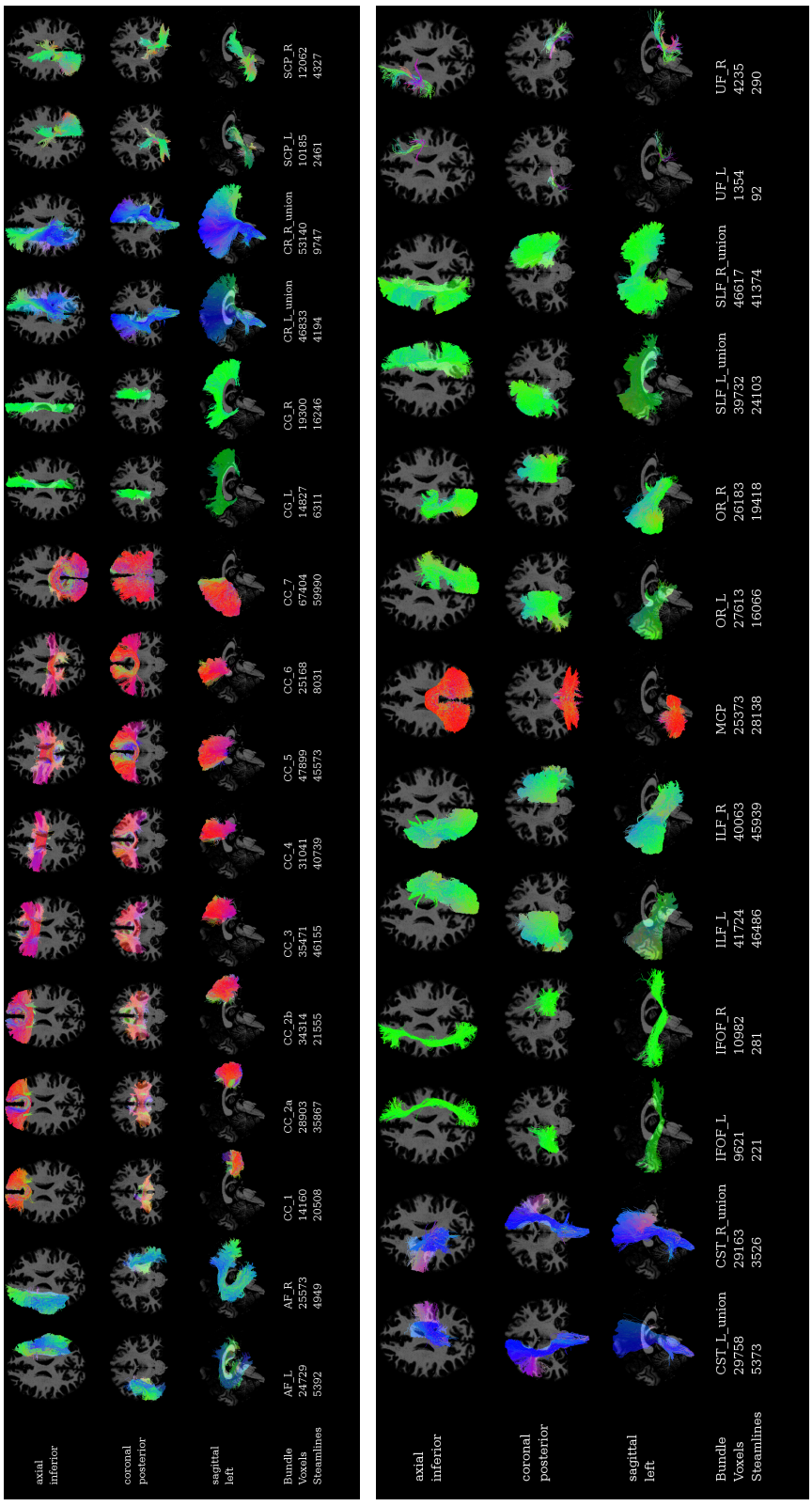

Figure 3.6: **True-positive bundles segmented with RecobundlesX.** Models of five subjects and nine different parameter configurations were used to perform forty-five executions of bundle recognition per model. After, a threshold of 75% of occurrence was applied to define a gold standard of true-positive bundles. The tractography used was generated using the data set corresponding to subject 100307 from the Human Connectome Project repository.

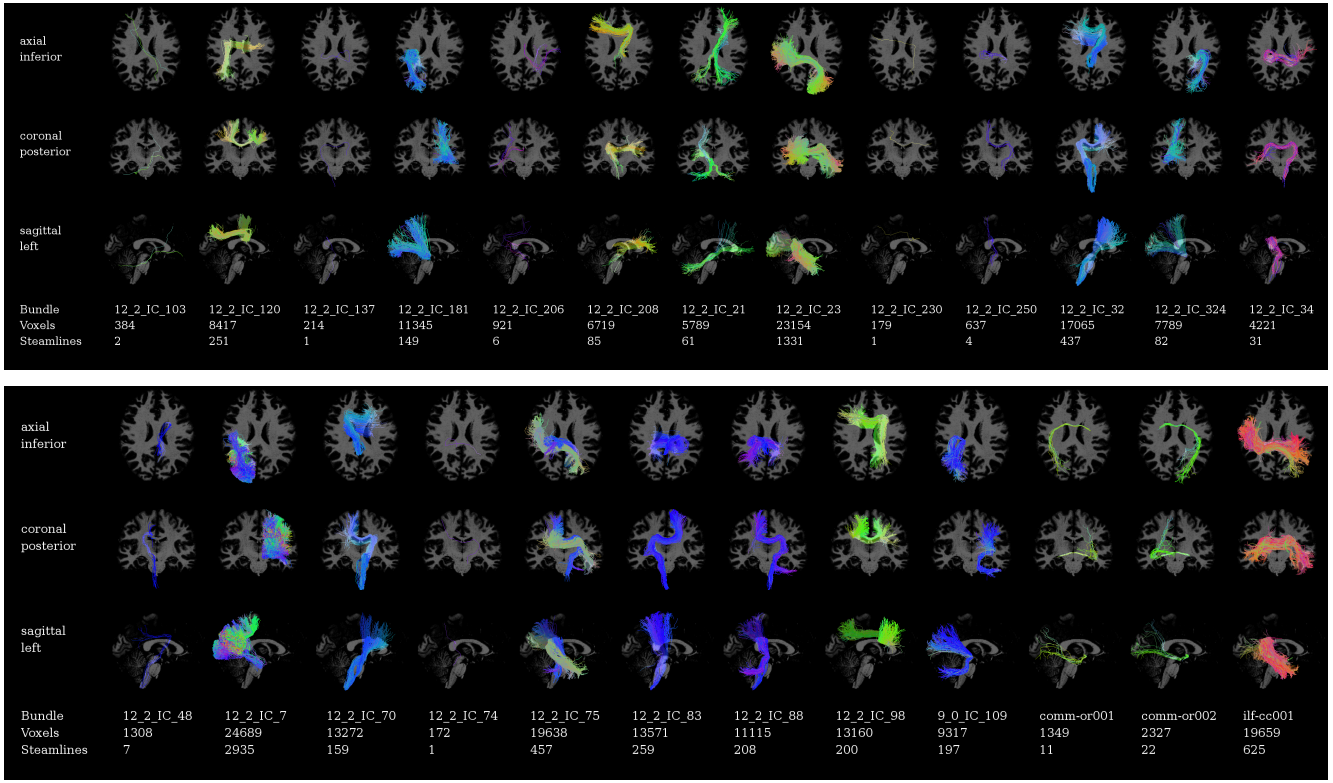

Figure 3.7: **False-positive bundles segmented with RecobundlesX.** Nine different parameter configurations were used to perform the bundle recognition per model. After, a threshold of 75% of occurrence was applied to define a gold standard of false-positive bundles. The tractography used was generated using the data set corresponding to subject 100307 from the Human Connectome Project repository.

To try to gain the intuition and to see what we could expect about this gold standard segmentation, in a further step, these true- and false-positive bundles were used to compute the corresponding connectomes. We used the structural T1-weighted image with the corresponding standard Desikan-Killiany (Desikan et al., 2006) parcellation in 85 gray matter regions of interest performed with FreeSurfer [4] replacing the brainstem with only its last part (i.e. medulla) (Iglesias et al., 2015).

The connectomes generated with the data set of subject 100307 from the HCP are presented in Figure 3.8 with their respective network density, i.e. the ratio between the actual and the possible connections. The Raw connectome has a density of 0.84, while the connectomes generated with the segmented true-positive (TP) and false-positive (FP) bundles have a density of 0.43 and 0.09, respectively, and the non labeled connections, i.e., the connections that were not classified as TP or FP created a connectome with a density of 0.39. Even though the density of the connectome of false positives is smaller than the one of the true positives, there is an intersection between them. This can be seen in Figure 3.9, which presents different operations between these connectomes, one is the intersection of connections created from TP and FP (top-left), which has a density of 0.08, most of the connections in the connectome of false positives are also labeled as true positives. The figure also presents the connectome created with the union of the labeled connectomes, i.e., TP or FP (top-right), the connections only labeled as true positive (bottom-left), and the connections without label (bottom-right). The connections that are labeled are less than 50%, and the connections labeled only as true positive are 35%, while 40% of the connections were not labeled. This shows that there are many important details of the WM represented by the streamlines that are not represented in the connectomes or its representation is ambiguous, and this also shows that there is information in the connectome that needs to be explained. Both cases will be studied in future work.

[4] `http://surfer.nmr.mgh.harvard.edu/`

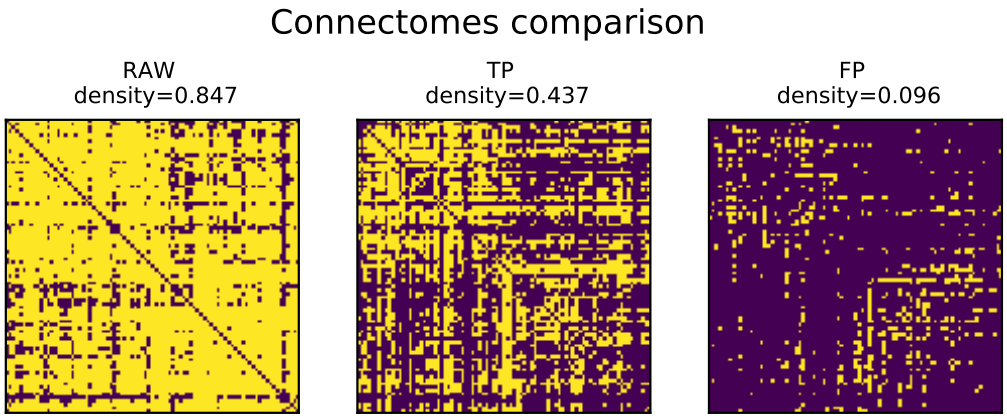

Figure 3.8: **Comparison of connectomes** created with a Raw tractogram and streamlines bundles labeled as true positive (TP) and false positive (FP) using RecobundlesX. The tractogram was created using a data set from the Human Connectome Project. For each connectome is presented the respective density.

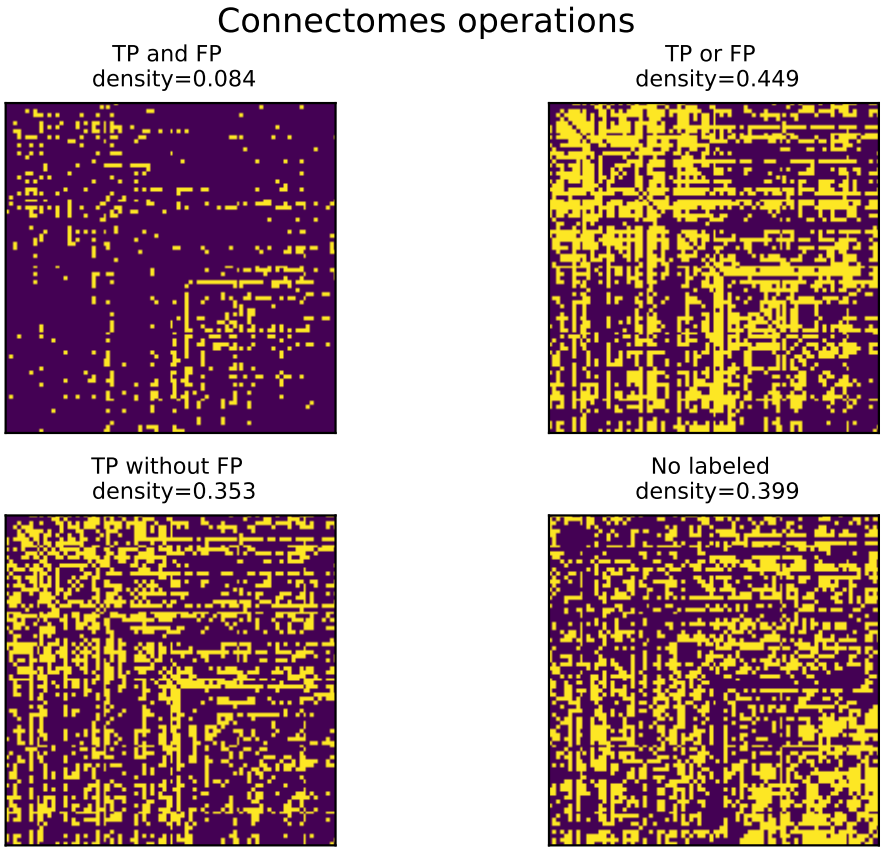

Figure 3.9: **Binary operations** of connectomes created with segmented true-positive (TP), and false-positive (FP) bundles. Intersection of the connections created with TP and FP (top-let), union of the connections, i.e., TP or FP (top-right), connections created only with TP, i.e. the connections labeled as TP and as FP were removed (bottom-left), and the connections created with streamlines that were not labeled, i.e. Raw \ (TP or FP).

Chapter 4

Injecting priors about brain anatomy and its organization

The purpose of this study was to evaluate whether we could improve the sensitivity/specificity trade-off of tractography by taking into consideration *two fundamental observations about brain anatomy* during the estimation process: (i) streamlines are not "just lines" but represent neuronal fibers, and (ii) such neuronal fibers are naturally organized in bundles. In fact, developmental neurobiology studies have demonstrated that "axons, as they grow, remain neighbors with axons that come from neighboring neurons in the presynaptic structure, and therefore arrive at the postsynaptic structure already topographically arranged" (Udin and Fawcett, 1988). The new formulation is an extension to the COMMIT (Daducci et al., 2013, 2015) framework, described in Section 2.5.3, and it is called COMMIT2 (Schiavi et al., 2020). This attempts to recover the tractogram and the connectome that best explains the signal estimated from the quantitative DW-MRI signal and, at the same time, tries to achieve this goal using the minimum number of bundles. This last condition was inspired by the recent theory about the economy of brain network organization (Bullmore and Sporns, 2012) and is explicitly promoted in our novel filtering procedure to reduce the incidence of false positives.

4.1 Materials and methods

To enforce the *first prior*, we implemented in matrix $\mathbf{A}$ of COMMIT a simple forward-model that assigns a contribution, i.e. volume or cross-sectional area, to each streamline of the input tractogram $\mathcal{T}$ proportionally to its length

inside each voxel. Then with Eq. 2.55 we require that the total amount of streamlines that traverse a voxel must sum up to the actual intra-axonal signal fraction in that voxel, which can be estimated in every voxel of the brain from DW-MRI acquisitions using standard models like NODDI (Zhang et al., 2012) or SMT (Kaden et al., 2016a) (see Section 2.3). As each streamline represents a coherent set of real anatomical fibers, there cannot be space for every possible reconstructed streamline. To implement the *second prior*, we first grouped all streamlines connecting the same pairs of gray matter regions and rearranged the corresponding columns of $\mathbf{A}$ accordingly, as shown in Figure 4.1. Then we added a new term to the cost function in Eq. 2.55 to try explaining the data, if possible, using the smallest number of such groups. Mathematically this is achieved with the *group lasso* regularization (Yuan and Lin, 2006) and the problem 2.55 becomes:

$$\underset{\mathbf{x}\geq 0}{\operatorname{argmin}} \; ||\mathbf{A}\mathbf{x}-\mathbf{y}||_2^2 \; + \; \lambda \sum_{g\in\mathcal{G}} ||\mathbf{x}^{(g)}||_2 \,, \tag{4.1}$$

where $\mathcal{G}$ is a general partition of the streamlines into groups, $\mathbf{x}^{(g)}$ represent the coefficients corresponding to the streamlines in a given group $g \in \mathcal{G}$ and the parameter $\lambda > 0$ controls the trade-off between data and the regularization term. This additional term in the cost function penalizes the contributions at the level of groups and, in practice, promotes (but does not constrain) convergence towards a solution that explains the measured DW-MRI data with the minimum number of bundles; this formulation does not have any prior knowledge about which groups correspond to true- or false-positive bundles. Note that setting $\lambda = 0$ corresponds to the classical COMMIT.

Without any strong a priori knowledge on the bundles, a classical way to operatively solve this problem is to use the so called *adaptive group lasso* (Wang and Leng, 2008) which penalizes all groups in the same manner independently of their cardinality. The problem can then be rewritten as:

$$\underset{\mathbf{x}\geq 0}{\operatorname{argmin}} \; ||\mathbf{A}\mathbf{x}-\mathbf{y}||_2^2 \; + \; \sum_{g\in\mathcal{G}} \lambda^{(g)} \, ||\mathbf{x}^{(g)}||_2 \,, \tag{4.2}$$

with

$$\lambda^{(g)} = \frac{\lambda \sqrt{|g|}}{||\mathbf{x}^{(g)}_{\text{NNLS}}||_2} \,, \tag{4.3}$$

where $|g|$ is the cardinality of the group g and $\mathbf{x}^{(g)}_{\text{NNLS}}$ are the weights of the streamlines obtained by solving the NNLS problem in Eq. 2.55, i.e. without

any regularization term. In this way, to define $\lambda^{(g)}$, the only parameter to set is λ, the rest of the information is taken from the data.

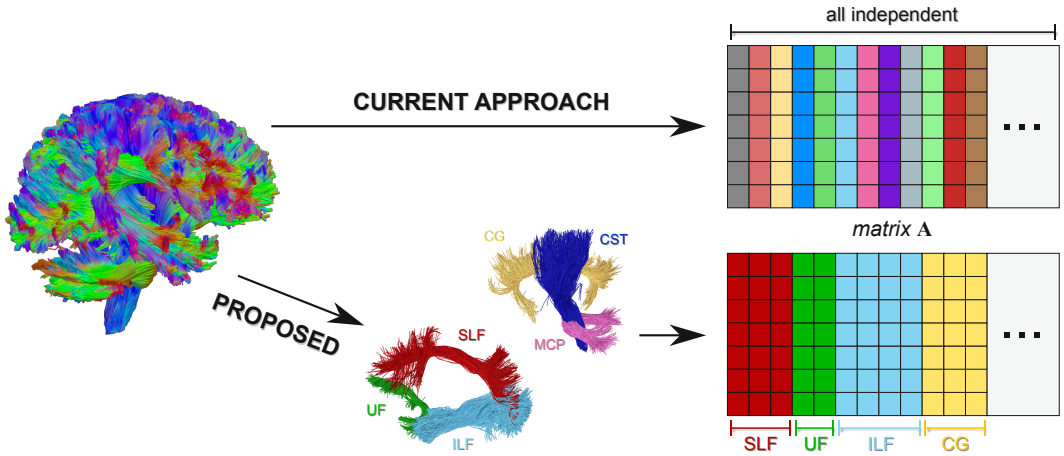

Figure 4.1: **Injecting priors about brain anatomy and its organization.** Current tractography algorithms consider all streamlines in a tractogram as independent entities and COMMIT is no exception; every column of the matrix **A** encodes a different streamline and all columns are treated as independent during the estimation of their contributions (top). The proposed method (COMMIT2) groups streamlines belonging to the same anatomical bundle together and considers the corresponding columns of **A** as a single entity in the estimation; every streamline is still modeled by a distinct column but streamlines belonging to the same bundle are arranged together as a sub-block of the matrix **A** and considered as a whole (bottom).

4.1.1 Synthetic phantom description and processing

We quantitatively evaluated our novel approach using a realistic digital phantom with known ground truth developed for the Reconstruction Challenge organized in 2013 at the IEEE International Symposium on Biomedical Imaging using Phantomas[1]. This simulated data set is shown in Figure 4.2A and consists of 27 ground-truth fiber bundles that were specifically designed to mimic real fiber configurations typically encountered in the brain (Figure 4.2B). These include complex arrangements of bending, crossing, and branching fibers, at various angles and with different curvatures; in addition, three spherical regions corresponding to fast diffusive compartments such as in brain ventricles were added. The corresponding DW-MRI signal was generated using the Composite Hindered And Restricted Model of Diffusion (CHARMED) (Assaf and Basser, 2005) along 64 directions with

[1] `https://github.com/ecaruyer/phantomas`

$b = 3000\,\mathrm{s/mm^2}$ and adding Rician noise with a signal-to-noise ratio of 30. The intra-axonal signal fraction of this phantom was computed from the geometry of the ground-truth streamlines.

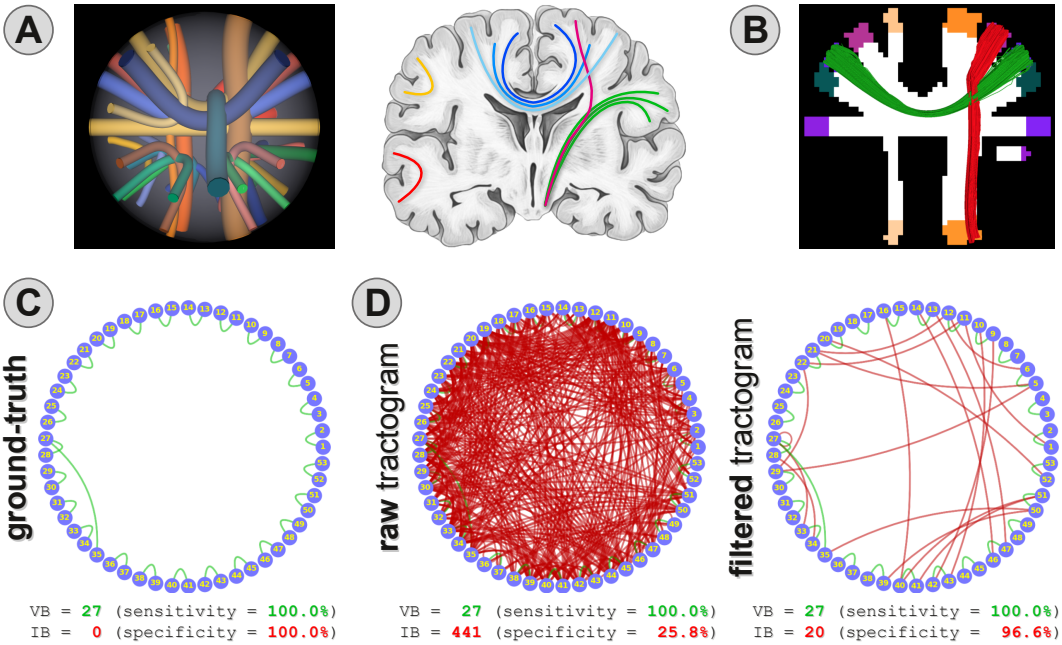

Figure 4.2: **Quantitative evaluation of the proposed method.** Synthetic data set (**A**, left), inspired by real anatomical bundles of the human brain (**A**, right), used to quantitatively evaluate our proposed method. White matter and gray matter masks used for tractography (**B**), as well as two examples of true-positive (green) and false-positive (red) bundles that can potentially be reconstructed with tractography. Ground-truth connectivity represented as a graph (**C**): blue circles correspond to the 53 gray matter regions shown in (**B**), whereas green represent true-positive or valid bundles (VB) and the red arcs represent false-positive or invalid bundles (IB), respectively. In (**D**), we compare the sensitivity and specificity of the estimated connectome before (left) and after filtering the tractogram with our COMMIT2 method (right).

Connectomes were constructed from the reconstructions obtained with both deterministic and probabilistic tractography using the 53 gray matter ROIs as network nodes. We employed the MRtrix software (Tournier et al., 2019) as it is a popular processing suite to analyze DW-MRI data. First, we computed the fODF in each voxel using Constrained Spherical Deconvolution (Tournier et al., 2007) with $\ell_{max} = 8$. Then, we reconstructed 1 million streamlines with both deterministic (SD_STREAM) and probabilistic (iFOD2) algorithms, using default parameters, and performing the tracking using the white matter mask as the seed region. Finally, we assigned each endpoint of a streamline to a node if that point fell within 2 mm from one of the 53 gray matter ROIs (default

setting); a streamline was considered as connecting two nodes if both endpoints were assigned; otherwise, it was discarded and excluded from the analysis.

For completeness, we also evaluated the proposed framework using two additional digital phantoms with more complex network configurations, created with Phantomas following a similar procedure as described in the recent work of Sarwar et al. (Sarwar et al., 2019). We defined 20 gray matter ROIs and then randomly generated two 3D geometries of fiber bundles in order to obtain a connection density in the resulting connectomes of 10% (Figure 4.3, blue panel) and 20% (Figure 4.3, rose panel), respectively. The centerline of each fiber bundle was defined using 3$^{\text{rd}}$ order piecewise polynomials and a constant radius was randomly assigned to each bundle in the range 1.5–4 mm. The generation of the DW-MRIs and the processing were performed as before.

4.1.2 Evaluation criteria

We assessed the sensitivity and specificity of the resulting connectome using the Tractometer metrics defined in (Côté et al., 2013). True positives are described in terms of the *Valid Connections* (VC) ratio, which is the proportion of streamlines in the tractogram that connect a correct pair of ROIs, as well as the corresponding number of *Valid Bundles* (VB). Similar metrics can be computed for the false positives, i.e. *Invalid Connections* (IC) and *Invalid Bundles* (IB). To summarize sensitivity and specificity in a single score, we computed the *Youden's index* $J = \text{sensitivity} + \text{specificity} - 1$. Sensitivity is defined as the ratio between VB and the number of real positive bundles (27 in this data set), and specificity as 1-IB/N, where N is the number of real negatives (594 in this data set). N represents the number of ROI pairs that may potentially be connected (incorrectly) by tractography and was computed by reconstructing 10 million streamlines with the probabilistic algorithm, as it is more permissive.

We also compared the performance of our novel formulation to other state-of-the-art filtering techniques: LiFE (Pestilli et al., 2014), SIFT (Smith et al., 2013), SIFT2 (Smith et al., 2015a) and COMMIT (Daducci et al., 2013, 2015). For each method, we downloaded the software package developed by the original authors, i.e. `https://github.com/brain-life/encode` for LiFE, `https://www.mrtrix.org` for SIFT/SIFT2 and `https://github.com/daducci/COMMIT` for COMMIT, and run the code with default parameters.

Finally, we investigated the accuracy in the estimation of the actual weights of the edges in the ground-truth connectome. However, as each technique

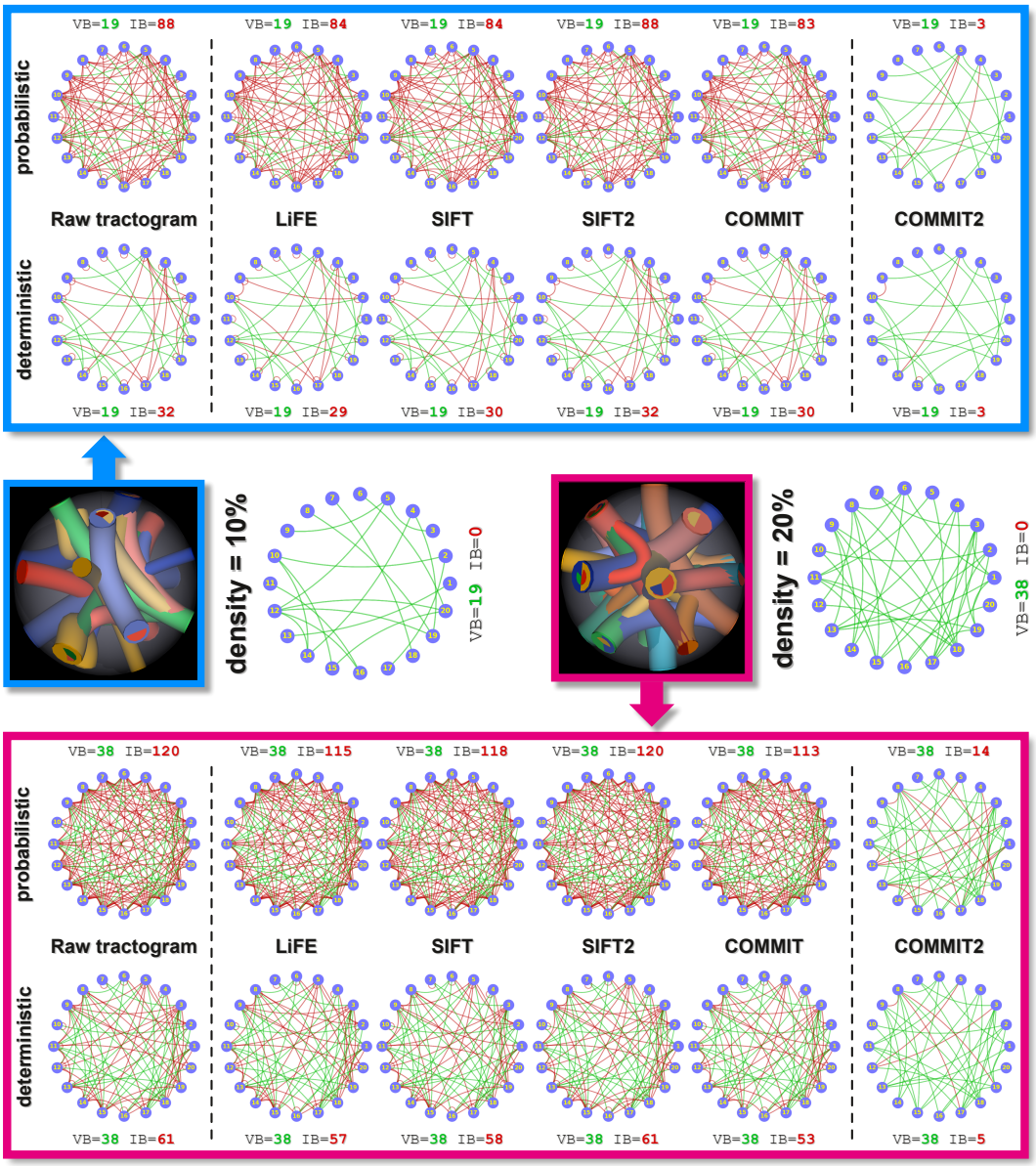

Figure 4.3: **Sensitivity and specificity of the connectomes in two additional digital phantoms with more complex and realistic network configurations.** Similarly to Figure 4.5A, we compare the valid (VB, green) and invalid (IB, red) bundles before and after applying all state-of-the-art filtering methods. The *blue* and the *rose* blocks correspond to the phantom with 10% and 20% connection density, respectively. COMMIT2 performances are systematically better than any other method in both configurations and show similar trends for both tractography algorithms.

assumes a different definition of connection strength between two brain regions, to validate these weights we first normalized each connectome to its maximum value, i.e., dividing all the values by the maximum to have values in the range $[0, 1]$, and then computed the root of the sum of squared differences

between them and the normalized ground-truth connectome. This measure was computed both considering all the connections in the connectomes

$$\varepsilon = \sqrt{\sum_{i,j=1}^{53} (C_{i,j} - \widetilde{C}_{i,j})^2} \tag{4.4}$$

as well as only the true-positive ones

$$\varepsilon_{\mathrm{TP}} = \sqrt{\sum_{(i,j)\in TP} (C_{i,j} - \widetilde{C}_{i,j})^2} \tag{4.5}$$

where $C_{i,j}$ indicate the entries of the ground-truth connectome, $\widetilde{C}_{i,j}$ the entries obtained from one of the compared methods and TP is a set containing only the pairs (i, j) corresponding to the true-positive bundles.

4.1.3 In vivo data processing

We also tested COMMIT2 on in vivo data using data from the Human Connectome Project (HCP) repository[2]. We downloaded the preprocessed diffusion data corresponding to subject 100307 as well as the structural T1-weighted image with the corresponding standard Desikan-Killiany (Desikan et al., 2006) parcellation in 85 gray matter regions of interest performed with FreeSurfer [3]. Detailed processing methods applied to all HCP open-access data are described in (Essen et al., 2013). We performed whole-brain Anatomically Constrained Tractography (ACT) (Smith et al., 2012). To do so, we first segment the T1-weighted image using FMRIB's Automated Segmentation Tool (FAST) (Zhang et al., 2001) to derive the multi-tissue image. This allowed performing the tissue-informed spherical deconvolution (Jeurissen et al., 2014). With the recovered fiber orientation distributions, we performed probabilistic tracking (iFOD2) and the white-matter mask as the seed region. We generated 5 million streamlines of length between 20 mm and 200 mm and default parameters. To create the connectome, we then used the standard 85 regions of interest of the FreeSurfer Desikan-Killiany atlas (Desikan et al., 2006) replacing the brainstem with only its last part (i.e. medulla) (Iglesias et al., 2015). To qualitatively assess the impact of COMMIT2, we segmented known true- and false-positive bundles using bundle models manually defined by an expert neuroanatomist and the procedure described in Chapter 3. Among all

[2] `https://www.humanconnectome.org`
[3] `http://surfer.nmr.mgh.harvard.edu/`

the existing models to estimate the voxel-wise intra-axonal signal fraction, we decided to employ the SMT (Kaden et al., 2016a). We acknowledge that this choice is arbitrary, but we believe it does not affect the validity of our framework. Indeed, to improve the microstructure model is out of the scope of COMMIT2, although it is important to choose one that has been proven to be valid for the DW-MRI data regime identified by the acquisition's parameters. We performed the fitting with the open-source code available at `https://github.com/ekaden/smt`. The connectomes were constructed using the streamline count for the original tractogram and the sum of weights for the one filtered with COMMIT2; we also computed the network density, i.e. the ratio between the actual and the possible connections. We compared the connectomes obtained after applying the state-of-the-art methods (SIFT, SIFT2, LiFE, and COMMIT) as described in the previous sections. The processing time was: $\approx 7'$ for SIFT, $\approx 4'$ for SIFT2, $\approx 24h$ for LiFE, $\approx 26'$ for COMMIT and $\approx 37'$ for COMMIT2; all experiments were conducted on a AMD 1950x workstation with 16 cores and 64 GB ram.

4.2 Results

4.2.1 Optimization of the regularization parameter

To set the regularization parameter λ that scales the groups' penalization and gives the best performance in the synthetic phantom, we performed several experiments by starting from zero and iteratively incrementing its value. We thus analyze the behavior of the VB, IB, and Youden's index J. Figure 4.4 analyzes the quality of the reconstructions that can be obtained by processing the raw tractogram using the proposed method. These plots correspond to probabilistic tracking, but similar results are obtained with the deterministic algorithm. In the first row are reported the number of VB and IB as a function of the regularization strength λ. Dashed lines correspond to the raw/unprocessed tractogram: VB=27 (corresponding to a sensitivity of 100%) and IB=441 (specificity 25.8%). We can notice that as λ increases, the number of IB decreases rather quickly but, correspondingly, the number of VB exhibits a much slower decrease trend. The decreasing rate of the IB slows down when they reach a value comparable with the VB. However, as expected, by increasing the regularization even further the number of VB also begins to decrease because, as it is known in optimization theory, when λ is too large the second term of Eq. 4.1 dominates and all groups are progressively

discarded. To help to choose the optimal value for λ, we made use of the index J, which is shown in the second row along with the percentage of valid connections (VC). The maximum value of J is about 0.97, which corresponds to VB=27 (sensitivity 100%) and IB=20 (specificity 96.6%). After it reaches its maximum, J starts decreasing as more and more VB are suppressed. Nonetheless, it is interesting to note that the percentage of VC exhibits an increasing trend also after this value, indicating that the rate of decrease of the IB is faster than the VB.

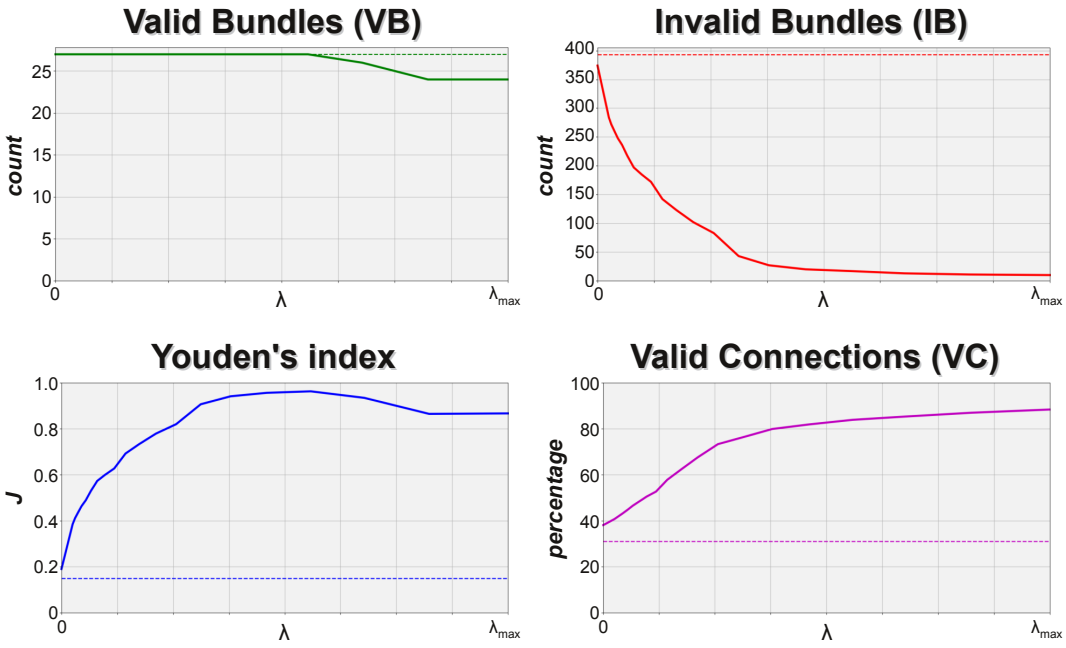

Figure 4.4: **Impact of adding the bundle-wise anatomical priors to COMMIT on the quality of the reconstructions.** In the first row are reported the number of valid (VB) and invalid (IB) bundles as function of the regularization strength (λ). In the second row are reported the Youden's index and the percentage of valid connections (VC). Results correspond to probabilistic tractography.

4.2.2 Sensitivity and specificity of the new formulation on simulated data

To quantitatively assess the effectiveness of our proposal we used a digital phantom with known ground truth (Figure 4.2A) specifically designed to mimic typical fiber configurations encountered in the brain. Figure 4.2B shows two examples of true- and false-positive bundles that may potentially be reconstructed with tractography, while the ground-truth connectome is shown in Figure 4.2C. We tested both deterministic and probabilistic tractography

and we assessed the sensitivity and specificity of the resulting connectomes using well-established metrics to evaluate tractography (Côté et al., 2013): number of valid bundles (VB), i.e. true-positive connections, and invalid bundles (IB), i.e. false positives. Figure 4.2D reports the number of VB and IB in a representative tractogram reconstructed with probabilistic tractography (left); results hold also for deterministic tractography (Figure 4.5A, second row). In line with previous literature (Thomas et al., 2014; Maier-Hein et al., 2017; Zalesky et al., 2016) all true-positive bundles were recovered, but at the price of including a large number of false positives (IB=441). Remarkably, after filtering the tractogram with COMMIT2 (right), the IB decreased from 441 to 20, boosting the specificity from 25.8% to 96.6%, without impacting the sensitivity.

4.2.3 Comparison to state-of-the-art filtering techniques

We compared this outstanding performance of COMMIT2 to other techniques that perform similar filtering procedures on the tractograms: LiFE (Pestilli et al., 2014), SIFT (Smith et al., 2013), SIFT2 (Smith et al., 2015a) and COMMIT (Daducci et al., 2013, 2015). We first tested their effectiveness in removing the false-positive bundles on tractograms reconstructed with both probabilistic and deterministic algorithms and the results are shown in Figure 4.5A. From the first column, we see that both tracking algorithms were able to reconstruct all 27 true bundles, i.e. high sensitivity, but at the price of recovering a large number of false positives, i.e. very low specificity (IB=441 in case of probabilistic tracking and IB=235 for deterministic). These results agree with previous literature (Thomas et al., 2014; Maier-Hein et al., 2017; Zalesky et al., 2016). In columns 2 to 5, we can see neither the sensitivity nor the specificity is substantially affected by filtering methods that use only microstructural information. In fact, all tractograms still contain all 27 true bundles and the number of IB diminished only marginally: LiFE 441 $\rightarrow$ 429 and 235 $\rightarrow$ 215, respectively; SIFT 441 $\rightarrow$ 342 and 235 $\rightarrow$ 216, respectively; COMMIT 441 $\rightarrow$ 393 and 235 $\rightarrow$ 204, respectively. SIFT2 does not remove streamlines, and bundles in this case, as none of the contributions assigned to the streamlines has exactly zero weight, the definition of a threshold is needed to optimally employ this method (further discussion below). On the other hand, the last column clearly shows that the inclusion of anatomical priors, i.e. COMMIT2, has a dramatic impact on the specificity as compared to models that consider only microstructure

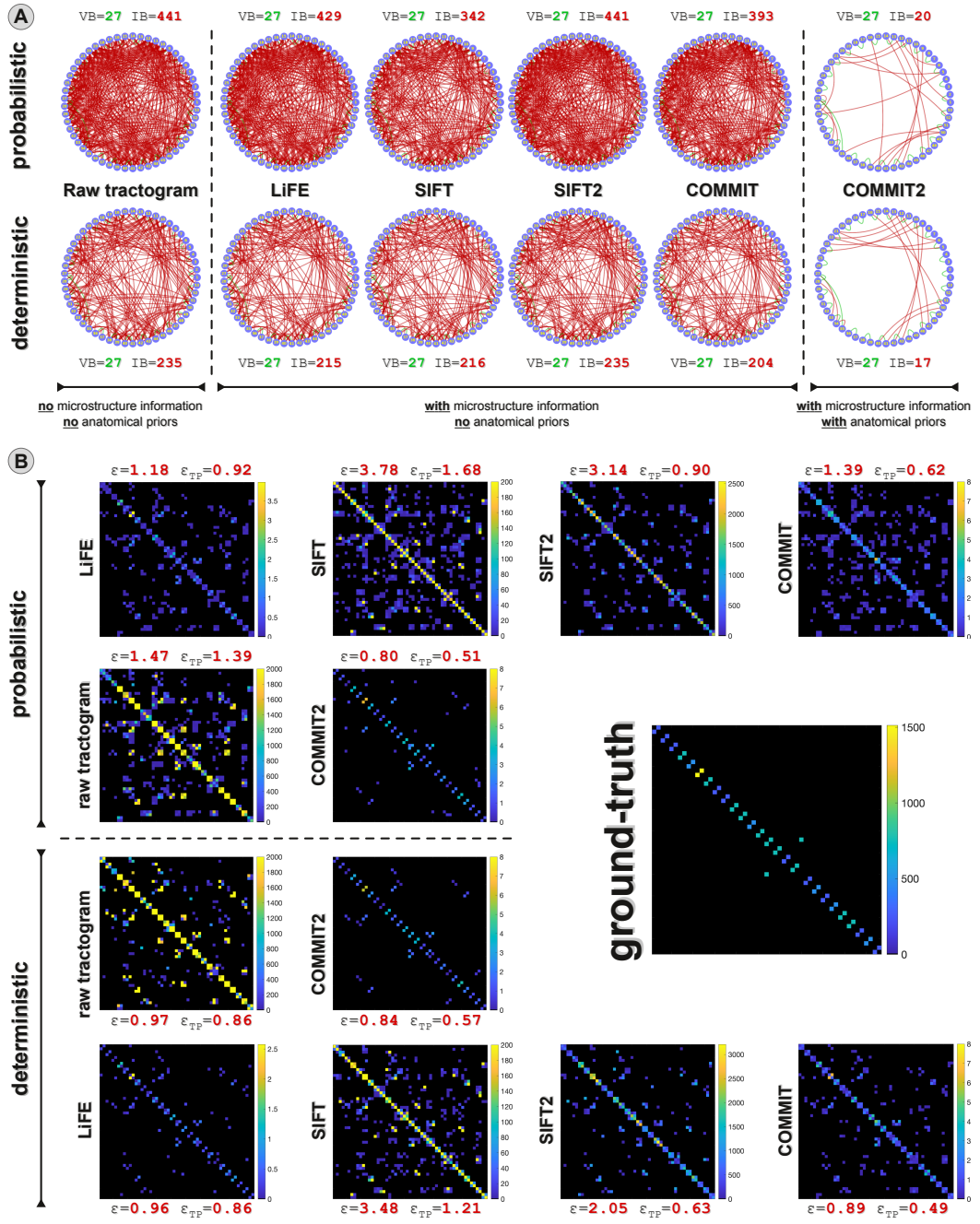

Figure 4.5: **Comparison with state-of-the-art filtering techniques.** (**A**) Sensitivity and specificity of the connectomes estimated with tractography before and after applying state-of-the-art filtering methods: LiFE, SIFT, SIFT2, and COMMIT; results with our novel approach are reported in the last column. Valid bundles (VB) are reported in green and invalid bundles (IB) in red. (**B**) Ground-truth fiber count connectome and weighted connectomes estimated with tractography before and after applying each method. ε and ε_{TP} quantify the difference between the normalized ground-truth connectome and those estimated by the methods when considering, respectively, all connections or only the true positives.

information: when using COMMIT2 the number of IB is dramatically reduced (441 $\rightarrow$ 20 and 235 $\rightarrow$ 17, respectively). These findings were confirmed also using additional digital phantoms with more complex network configurations (Figure 4.3).

For all the methods, we also compared their ability to accurately estimate the actual edge weights of the ground-truth connectome. Figure 4.5B shows the estimated connectomes represented as matrices, where we can appreciate the quite different definitions of connection strength assumed by each method: actual fiber count used to generate the ground-truth phantom, streamline count for the raw and the SIFT-filtered tractograms, sum of the streamline weights estimated by SIFT2 and LiFE from the entire DW-MRI signal or, in the case of COMMIT and COMMIT2, from the fiber density map. To fairly compare such different approaches, we normalized the connectomes and computed the distance between them and the normalized ground-truth connectome. If we consider all connections, i.e. ε, the error with COMMIT2 is very small as compared to the raw tractogram, LiFE, and COMMIT, which are about 50–80% higher, while SIFT and SIFT2 obtained even higher errors. Focusing only on the true-positive connections, i.e. $\varepsilon_{\mathrm{TP}}$, we observe again that COMMIT2 outperforms all other methods, but now SIFT2, LiFE and COMMIT show comparable results whereas the raw and SIFT-filtered ones have almost twice the error.

4.2.4 Comparison to other basic filtering procedures

We also compared COMMIT2 to other *basic filtering procedures* often used in the literature to discriminate between true- and false-positive bundles in the connectomes. Figure 4.6 reports the Receiver Operating Characteristic curve analysis for the performance of such methods on the tractogram reconstructed with probabilistic tractography; results hold for deterministic tracking. The connectomes corresponding to the best performance (i.e. max J) of each method are reported as well. COMMIT2 results are plotted in pink as function of the relative importance of the anatomical priors in the filtering procedure; the best performance with J=0.97 corresponds to the connectome shown in Figure 4.2D. The yellow line refers to results obtained by using the same formulation of COMMIT2 but considering the streamlines as independent. This is called lasso regularization (Tibshirani, 1996) and consists in promoting sparsity at the level of the individual streamlines rather than the bundles; this form of regularization was tested in the original COMMIT

formulation (Daducci et al., 2013, 2015). The gray line corresponds to filtering the tractogram by *thresholding* the bundles as function of their cardinality, i.e. removing progressively the connections containing a low number of streamlines, which is a very common procedure employed in clinical studies to reduce the presence of false positives in the connectomes. For the sake of comparison, we also tested the effect of *randomly filtering* the bundles at the same removal rate of COMMIT2 (dark blue); the reported values correspond to the average score from 100 different experiments. The best performance of each approach (i.e. max J) is also reported as a graph for visual inspection. Comparing the pink and the yellow curves we can easily appreciate that without the grouping of streamlines implemented in our new formulation only a very modest improvement of the sensitivity/specificity trade-off was possible (max J=0.64). Interestingly, COMMIT2 outperformed thresholding, as this latter could improve only marginally the initial configuration (VB=27 and IB=441, top-left of Figure 4.5A) up to a maximum J=0.72, corresponding to decreasing the IB to 120 but also to a loss of 2 valid ones. Per contra, COMMIT2 was able to reduce significantly more invalid bundles (441 $\rightarrow$ 20) before losing valid ones. We also investigated the impact of thresholding on the connectomes already filtered by previous methods (Figure 4.7). All methods largely benefitted from this additional post-processing, even though none could reach the same performance of COMMIT2. Notably, thresholding caused the loss of 2 of the 27 valid bundles in all cases but COMMIT2, on which it had no effect.

4.2.5 Qualitative evaluation on in vivo human brain data

Finally, we tested the effectiveness of the new formulation on in vivo data from the Human Connectome Project (Essen et al., 2013). As the ground truth is unknown, we qualitatively assessed the impact of COMMIT2 on known true- and false-positive bundles that were manually defined by an expert neuroanatomist using the procedure described in Chapter 3. The top row of Figure 4.8 shows ten of these known bundles as reconstructed in the original tractogram along with the voxel coverage, i.e. number of voxels traversed by the streamlines associated with each bundle; the bottom row reports the same bundles after filtering with COMMIT2. Results show that our COMMIT2 filtering procedure does not affect the true-positive bundles, as the voxel coverage is comparable with the original tractogram and the total contributions estimated by COMMIT2 are high. This means that COMMIT2 removes implausible streamlines inside the bundles, but recognizes these bundles as

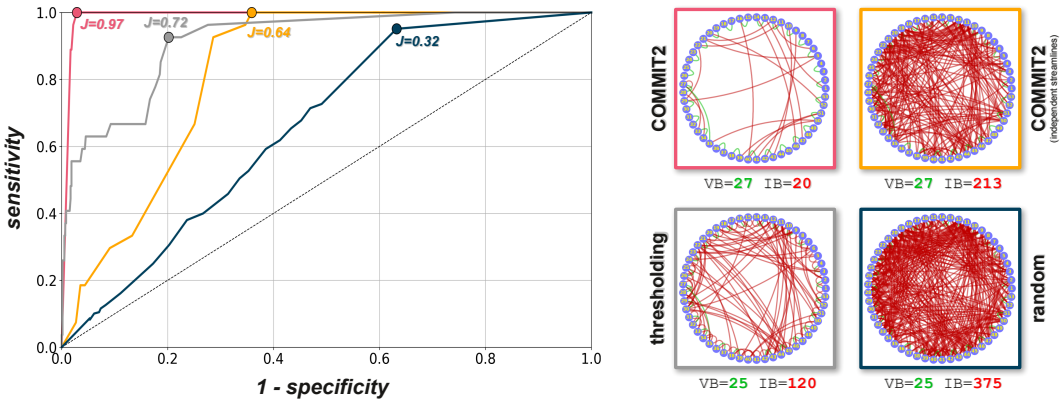

Figure 4.6: **Comparison with basic filtering procedures.** Receiver Operating Characteristic curve analysis to assess how COMMIT2 (pink) compares to other filtering procedures present in the literature in terms of discriminating between true- and false-positive bundles in the connectome. The yellow results correspond to using the same formulation of COMMIT2 but considering all streamlines as independent. We also tested the effect of filtering the tractogram by thresholding the bundles as function of their cardinality (gray) as well as their random removal using the same rate (dark blue). The best performance of each approach (i.e. max J) is reported as a graph for visual inspection.

fundamental to explain the data and keeps the coverage of the white matter intact. Conversely, the false-positive bundles are drastically thinned, i.e. the voxel coverage is extremely reduced, and the weights assigned to them by COMMIT2 are close to zero, meaning they are not necessary to explain the signal. In particular, we observe that while the less populated bundles are (almost) completely removed, the more populated ones are extremely thinned in terms of white matter coverage and their contribution to the resulting connectome is minimal. This effect can be observed also on the differences between the weights of the connectomes reported on the left side of the figure.

In absence of ground truth, we could only evaluate the estimated networks qualitatively. The raw connectome appears very dense, which is an expected result as it corresponds to probabilistic tracking, but we can clearly observe that after filtering with COMMIT2 it is definitely more sparse, in agreement with the recent theory about the economy of brain networks (Bullmore and Sporns, 2012). The connectomes recovered with SIFT, SIFT2, LiFE, and COMMIT are shown in Figure 4.9; all have a density that is at least twice as dense as the one estimated with COMMIT2. However, from the visual inspection of the known true- and false-positive bundles, our results suggest that this higher level of sparsity does not imply the loss of valid connections,

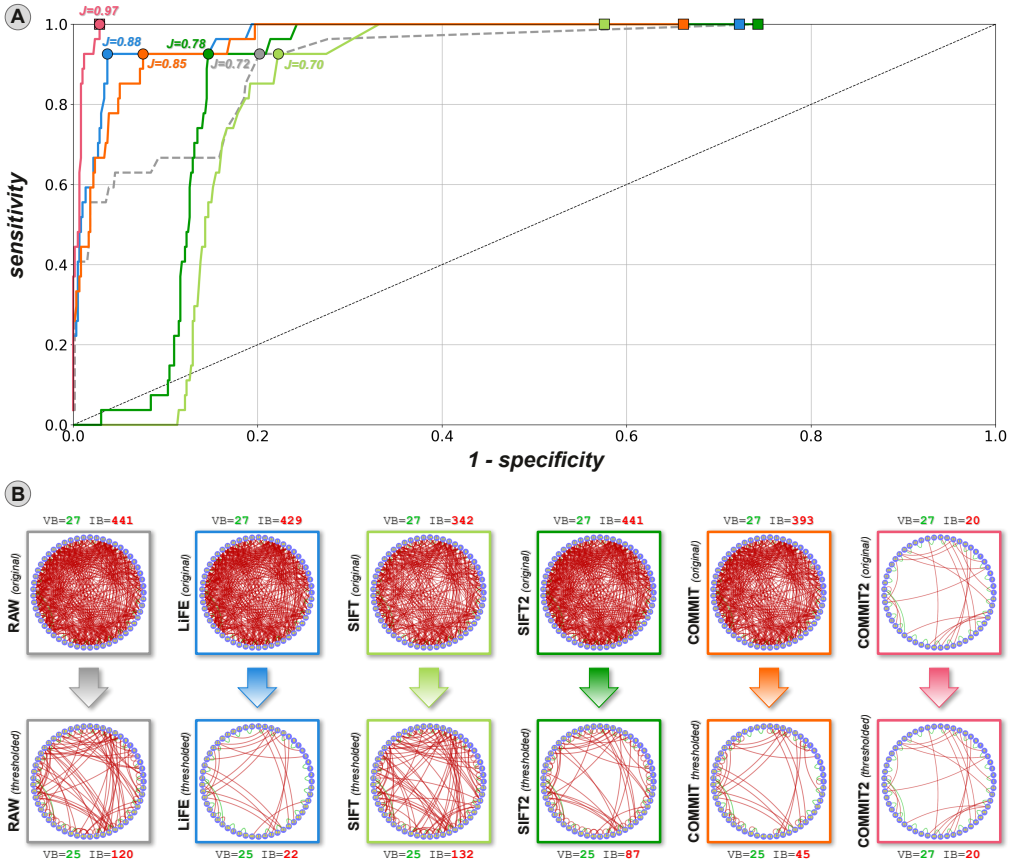

Figure 4.7: **Effect of thresholding on the estimated connectomes.** (**A**) Receiver Operating Characteristic curve analysis to assess how COMMIT2 compares to the state-of-the-art filtering procedures when their estimated connectomes are further thresholded. Connections were gradually removed from the connectomes based on the streamline count for raw tractograms and SIFT, and on the streamline weight sum for LiFE, SIFT2, COMMIT, and COMMIT2. The *squares* correspond to the original connectomes estimated by each method, whereas the *circles* to the best performance after thresholding, i.e. max J. The connectomes before and after this additional filtering are reported in panel (**B**) for visual inspection. All methods largely benefitted from this additional thresholding, even though none could reach the same performance of COMMIT2. Besides, thresholding caused the loss of 2 valid bundles for each method whereas it had no effect in the case of COMMIT2.

but seem to indicate that the connections that are filtered out are indeed incompatible with the underlying data.

4.3 Discussion

Tractography has proven particularly effective for studying noninvasively the neuronal architecture of the brain but recent studies have challenged

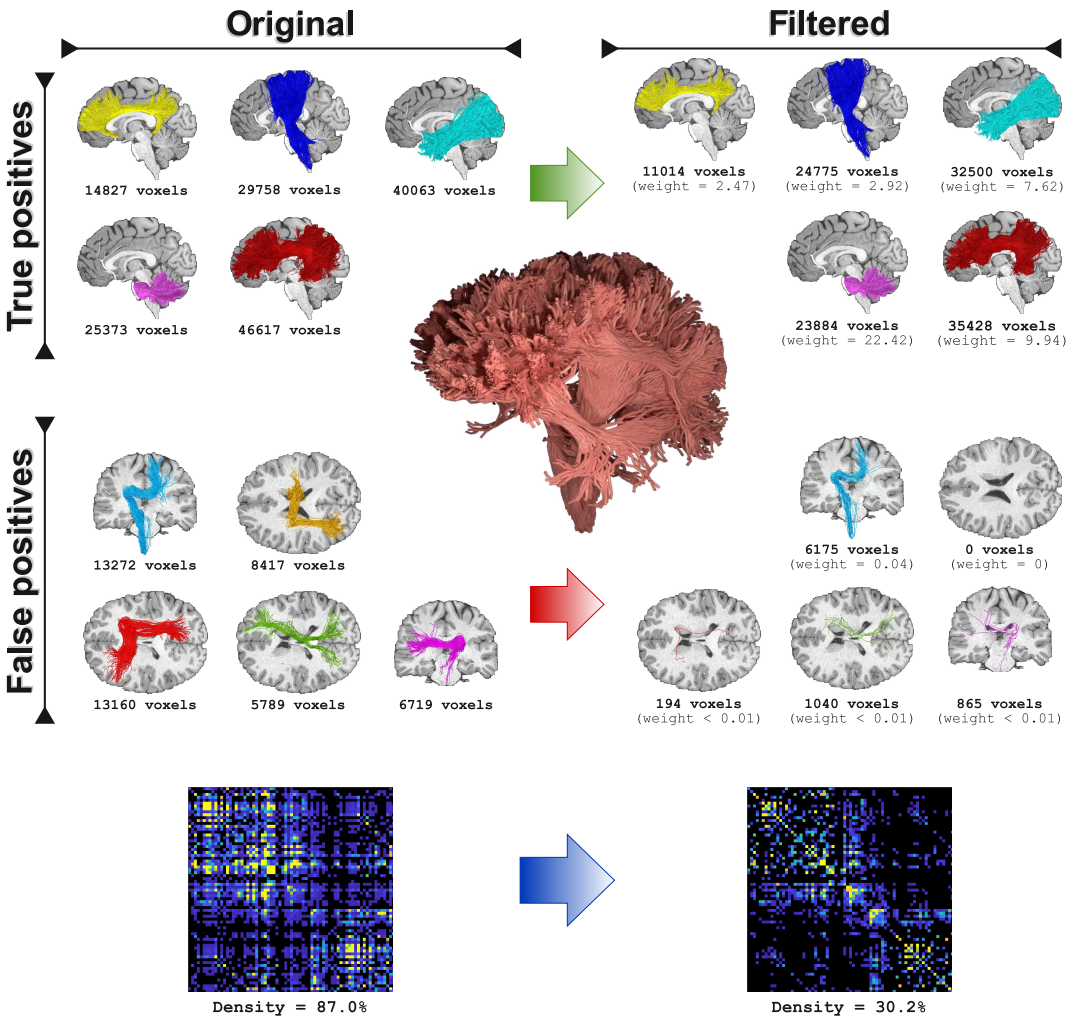

Figure 4.8: **Qualitative evaluation of the proposed method with in vivo data.** In the first column (Original) are reported the bundles and the connectome of the input tractogram while in the second column (Filtered) the same filtered by COMMIT2. To better compare the bundles before and after the filtering, we report the voxels coverage as well as the sum of the streamlines weights assigned by COMMIT2. The filtering procedure behaves extremely differently for the true (first row) and the false (second row) positives. Indeed, while the voxels coverage of the true positives remains intact, the one of the false positives is dramatically reduced and, in some cases, they are completely removed. Looking at a more quantitative meaningful measure - the COMMIT2 weights - we also appreciate that the weights associated with the true positives are much higher than those of the false positives, which are very close to zero.

its accuracy (Thomas et al., 2014; Maier-Hein et al., 2017; Zalesky et al., 2016; Drakesmith et al., 2015). In particular, it was shown that the presence of false-positive connections in the reconstructions can significantly bias the topological properties of the estimated brain networks, raising serious concerns for its use in mapping the human connectome. Some authors prescribed

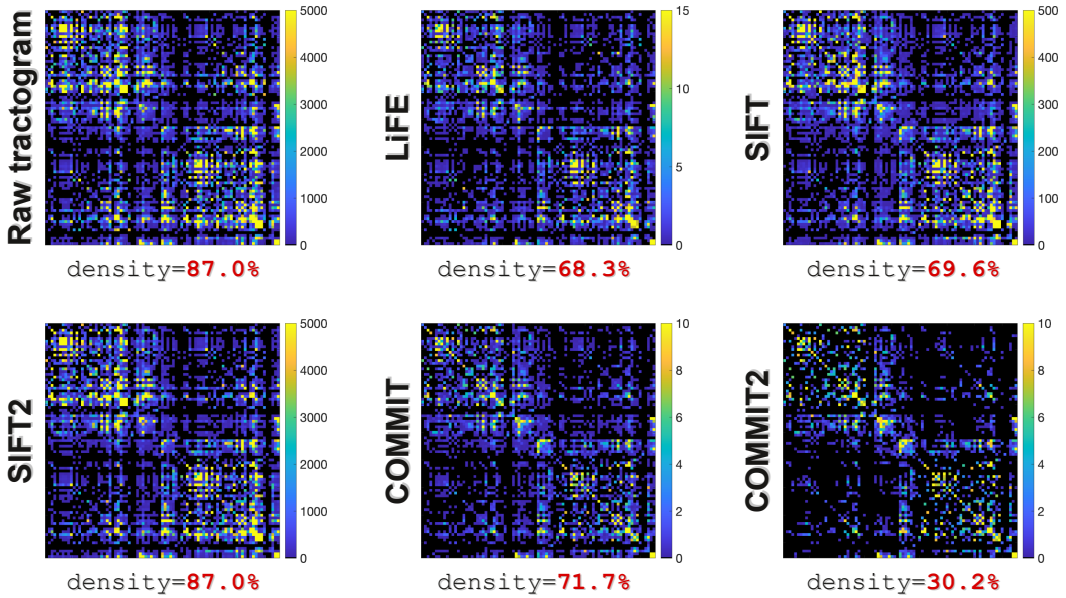

Figure 4.9: **Comparison of connectomes estimated on the HCP data**. From the top left to the bottom right, we show the connectomes estimated with probabilistic tractography before (first entry) and after applying state-of-the-art filtering methods: LiFE (second entry), SIFT (third entry), SIFT2 (fourth entry), and COMMIT (fifth entry). Results with our novel filtering approach (COMMIT2) are reported in the last entry. Below each connectome the density of the network is reported.

the need for a revolution of tractography techniques in order to reconstruct the known anatomy reliably while controlling for false positives and, in particular, that the notion of both anatomy and microstructure is essential to progress (Maier-Hein et al., 2017). We explicitly developed COMMIT2 with this concept in mind and, in fact, our novel formulation naturally incorporates both these characteristics. Apart from sharing the same convex optimization procedure with the original COMMIT, the method presented here is a significant improvement of the previous framework and not only an incremental variant. The possibility to inject priors about brain anatomy and its organization, and not only about microstructural properties, represents a powerful and novel way to tackle the false positive problem in tractography and brain structural connectivity. When we compared the performance of COMMIT2 with other state-of-the-art filtering techniques (LiFE, SIFT, SIFT2 and COMMIT) (Pestilli et al., 2014; Smith et al., 2013, 2015a; Daducci et al., 2013, 2015), which are all similar in spirit to our proposed method but are purely data driven, none of them proved effective in reducing invalid bundles. This clearly indicates that adding anatomical priors about the organization of the bundles has indeed a dramatic impact on the specificity of the estimated

connectomes.

COMMIT2 is not a pure tractography algorithm, but a flexible filtering procedure that can be applied on top of any tractogram. An appealing feature of the COMMIT2 formulation is that it allows injecting additional priors on the bundles. A possible way to take advantage of this property is to use the anatomical knowledge we have on bundles. In practice, if we knew that a connection surely exists, e.g. from atlases or population studies, we could promote the corresponding bundle; conversely, if we knew that a specific tractography algorithm is keen to find a particular implausible connection, we may want to penalize it more than others during the filtering. Thus, as our knowledge about true and false bundles improves, COMMIT2 results can be directly improved, since the framework can selectively promote or penalize groups of fibers with these priors. Besides, we demonstrated the effectiveness of this new formulation by fitting the streamlines to the intra-axonal signal fraction map estimated from DW-MRI with a specific biophysical model, but multiple options are available in the literature, e.g. (Assaf and Basser, 2005; Kaden et al., 2016a; Zhang et al., 2012) among others. We believe this choice does not affect the validity of our results, as this map could be replaced by any additive quantity as long as this provides a proxy measure of axonal density or any microstructural property of the fibers that is invariant along their pathway. The investigation of which map is the most suitable as input for COMMIT2 was beyond the scope of this work and will be subject of future studies. Clearly, the more our knowledge of microstructural modeling grows, the more accurate the estimates with our framework will become.

By performing experiments with both deterministic and probabilistic tractography, we could observe that despite the initial connectomes were quite different, after filtering them with COMMIT2 they became more comparable and with minimal discrepancy of network density. On the contrary, the connectomes estimated by other methods differ quite heavily depending on the input tracking method. This suggests that the application of COMMIT2 converges towards a more reliable estimation of connectivity. Sarwar et al. (Sarwar et al., 2019) recently investigated whether using deterministic or probabilistic tracking is preferable for clinical studies. They concluded that to minimize the impact of false positives one should prefer deterministic tracking at the price of having maybe some false negatives, unless a strong thresholding is employed on the connectomes estimated with probabilistic tracking. Here we presented results using both, showing that although the input was different

the final results obtained with COMMIT2 are comparable. On the tractogram obtained with probabilistic tracking, we also compared the performances of COMMIT2 against a standard thresholding procedure showing that although the latter was able to improve the initial configuration, also at its best performance was far from the accuracy obtained with COMMIT2. In the same spirit, to analyze in vivo data we performed probabilistic tracking with multi-shell multi-tissue anatomically constrained tractography (Smith et al., 2012) to highlight the benefits of the application of COMMIT2 even on top of one of the most accurate state-of-the-art methods. Nevertheless, we stress that, as already pointed out by the results on synthetic data, the performances of COMMIT2 on a different input tractogram would be comparable.

Besides improving the estimation of brain connectivity, we believe that COMMIT2 is also a promising tool that can be routinely used by neurosurgeons for whom tractography has rapidly become an essential tool for planning surgery. By allowing visualization of the different bundles before the operation, tractography has always been considered as a potential tool, but since its reliability has always been under debate, not all neurosurgeons feel comfortable to trust it. Nevertheless, the continuous progress in MRI scanners has already provided them easy access to patient's diffusion images through which they can now have access to a more reliable structural connectivity reconstruction. The short computational time required by COMMIT2 can allow its application on any type of whole brain tractograms that may be built from a large database (like HCP[4], UK BioBank[5], ...) in order to extract and study the most reliable bundles and omit the false-positives ones. Indeed, with COMMIT2, we could now perform studies on the variability of the diffusion metrics along bundles in large cohorts of subjects and possibly relate them with their functional counterpart.

Although we obtained outstanding results, we acknowledge that the proposed framework is not without limitations, and there is room for future improvements. First, the bundle regularization guarantees that if a group is not necessary to explain the signal, then all its streamlines will be discarded. This implies that none of the eventual good streamlines present in that group will be kept, so the choice made to group streamlines plays a critical role. Instead, if a group is necessary to explain the signal, even if a streamline follows a very different path from the others in the same group, because of this choice of

[4] `https://www.humanconnectome.org`
[5] `https://www.ukbiobank.ac.uk`

regularization, it will be kept since it still connects the same two ROIs. Even though a proper way to filter inside groups is yet under investigation and will be an object of future works, we can speculate that one possible way to do that is considering a finer parcellation for the gray matter resulting in smaller groups to be evaluated by the framework. Another way could be using clustering techniques to group streamlines together, e.g. (O'Donnell et al., 2013). These possibilities will be tested and compared in future analyses. In Chapter 5 is presented an evolution of COMMIT2, where a hierarchical structure of groups is used to perform the filtering. Another key assumption of our formulation is that, at the current resolution of DW-MRI and recalling that streamlines do not represent single axons, the contribution of every streamline remains constant along its path. This assumption is shared by all methods considered in this study and most state-of-the-art tractography algorithms present in the literature. Of course, if this assumption was not biologically valid, all these algorithms and the results presented here might be biased.

Chapter 5

Refinement based on the hierarchical organization of fibers

In the previous formulation (COMMIT2, see Section 4.1), the partition $\mathcal{G}$ was created using a parcellation-based approach, i.e., grouping together all the streamlines connecting the same pair of cortical regions. However, as Eq. 4.2 promotes or penalizes each group of streamlines as a whole, if a group contains both true- and false-positive streamlines, as shown in Figure 5.1 (top), they will be promoted or penalized together. In Figure 5.1 (bottom) we present an example of an actual bundle of streamlines reconstructed with tractography from in vivo data where this situation happens. This bundle consists of two distinct sub-bundles: the streamlines that directly connect the brainstem to the postcentral gyrus, which are known to be correct from anatomy, and those that incorrectly pass through the corpus callosum. Applying COMMIT2 using a gray matter parcellation as in (Schiavi et al., 2020) results in a single group for this bundle which does not allow disentangling the true-positive streamlines from the false positives. If, instead, smaller groups are used, e.g., obtained from a finer parcellation or a clustering procedure, some invalid structures are lost but at the price of losing also some of the true-positive streamlines that were connected to the inferior part of the postcentral gyrus (see below for a discussion on this topic). However, if we combine the previous groups in a hierarchical way, the false-positive streamlines can be removed and more true positives can be kept. Inspired by this example, we propose to modify COMMIT2 (Schiavi et al., 2020) and make it more flexible, allowing the possibility to group the streamlines into multiple levels in order to capture the natural hierarchical organization of the fibers in fascicles and subfascicles (Chenot et al., 2019; Nieuwenhuys et al., 2008). This new

formulation is called COMMIT2$_{\text{tree}}$ (Ocampo-Pineda et al., 2021).

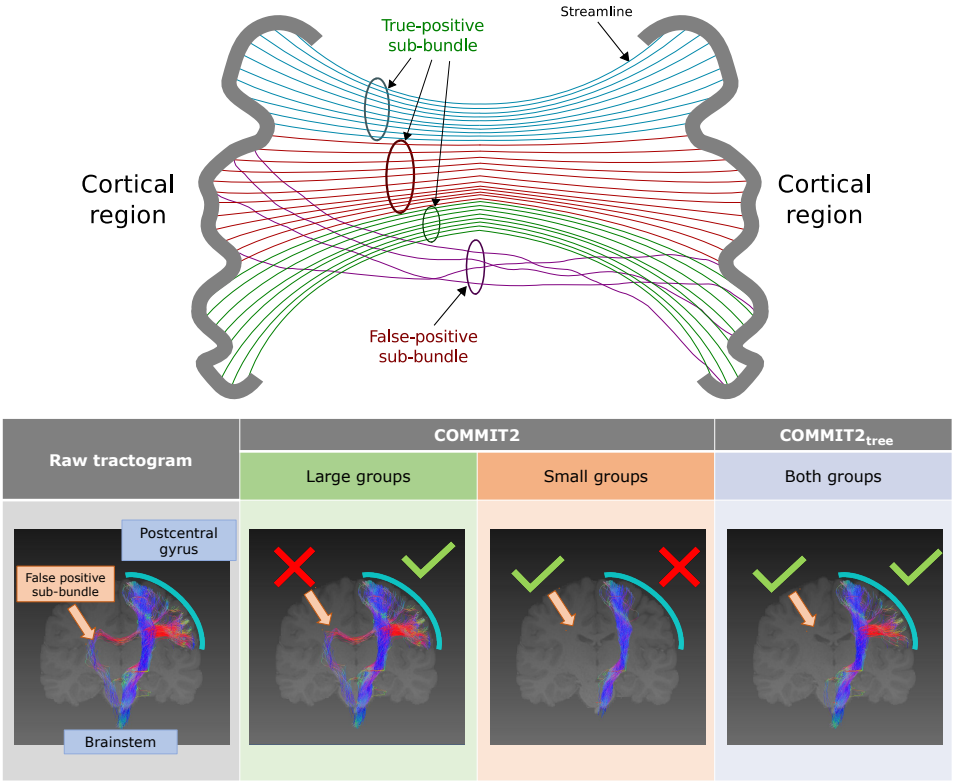

Figure 5.1: **Possible improvement over the COMMIT2 formulation.** Top: This simplistic example shows some representative streamlines between two cortical regions obtained with a generic tractography algorithm. This bundle consists of three true-positive sub-bundles (blue, red, and green) but there are also some streamlines that seem to describe odd or implausible trajectories (purple), which are probably false positives. However, using the parcellation-based approach introduced in COMMIT2, all these streamlines are grouped together as one unique bundle and considered as a whole, so they cannot be differentiated in true and false trajectories. Bottom: Example of an actual bundle of streamlines from in vivo data as reconstructed in the input tractogram and after filtering with COMMIT2, using either large or small groups, and with COMMIT2$_{\text{tree}}$ using both large and small groups in a hierarchical structure. This bundle consists of plausible streamlines that directly connect the brainstem to the postcentral gyrus (cyan arc), as well as of implausible streamlines that incorrectly pass through the corpus callosum (orange arrow).

5.1 Materials and methods

To take into account this organization of the streamlines, we implemented the hierarchical sparse encoding approach proposed by Jenatton et al.

(2011), which uses sparsity-inducing norms as regularization terms to promote tree-structured sparse solutions. The set of groups $\mathcal{G}$ is defined as a tree-structured set of groups with n levels, where each level d represents a partition of all the streamlines. The root $\mathcal{G}_0$ contains all the streamlines of the tractogram in one group and the partitions in the lower levels called $\mathcal{G}_1, ..., \mathcal{G}_n$ are created by splitting each group $g_{d-1} \in \mathcal{G}_{d-1}$, creating a nested structure. The reconstruction problem can be written as:

$$\underset{\mathbf{x} \geq 0}{\operatorname{argmin}} \, ||\mathbf{A}\mathbf{x} - \mathbf{y}||_2^2 + \lambda \sum_{d=1}^{n} \sum_{g_d \in \mathcal{G}_d} \omega^{(g_d)} ||\mathbf{x}^{(g_d)}||_2 \, , \tag{5.1}$$

where $\mathcal{G}_d$ represents a partition into groups of level d, $\mathbf{x}^{(g_d)}$ are the coefficients of the streamlines in group $g_d \in \mathcal{G}_d$ and $\lambda \geq 0$ controls the regularization strength. Note that if $n = 1$ then Eq. 5.1 reduces to Eq. 4.2. The scaling factor to balance groups with different cardinality is modified as follows:

$$\omega^{(g_d)} = \frac{\sqrt{|g_d|}}{||\mathbf{x}_{\text{NNLS}}^{(g_d)}||_2} \, , \tag{5.2}$$

where $|g_d|$ is the cardinality of the group g_d and $\mathbf{x}_{\text{NNLS}}^{(g_d)}$ are the contributions of the streamlines that belong to the group g_d estimated without group regularization, that is, $\lambda = 0$ (Eq. 2.55). The regularization in Eq. 5.1 is also called Hierarchical Group Lasso and was introduced by Zhao et al. (2009). Different implementations exist of this formulation, and for our application, we implemented the one proposed by Jenatton et al. (2011). The main advantage of this formulation is that its complexity is linear in the number of streamlines and levels, so increasing the number of levels does not significantly affect the computation time (for further details we refer the reader to the mathematical proofs contained in (Jenatton et al., 2011)), we will refer to this approach as COMMIT2$_{\text{tree}}$. Figure 5.2 visually compares the differences between COMMIT (Daducci et al., 2013, 2015), COMMIT2 (Schiavi et al., 2020), and COMMIT2$_{\text{tree}}$ (Ocampo-Pineda et al., 2021) formulations.

5.1.1 Illustrative toy example.

Figure 5.3 shows a simple synthetic example to illustrate how the introduction of the hierarchical regularization can improve the accuracy of the tractograms. The ground truth consists of four regions of interest (A, B, C, and D) connected by three streamlines (S1, S2, and S3). From this

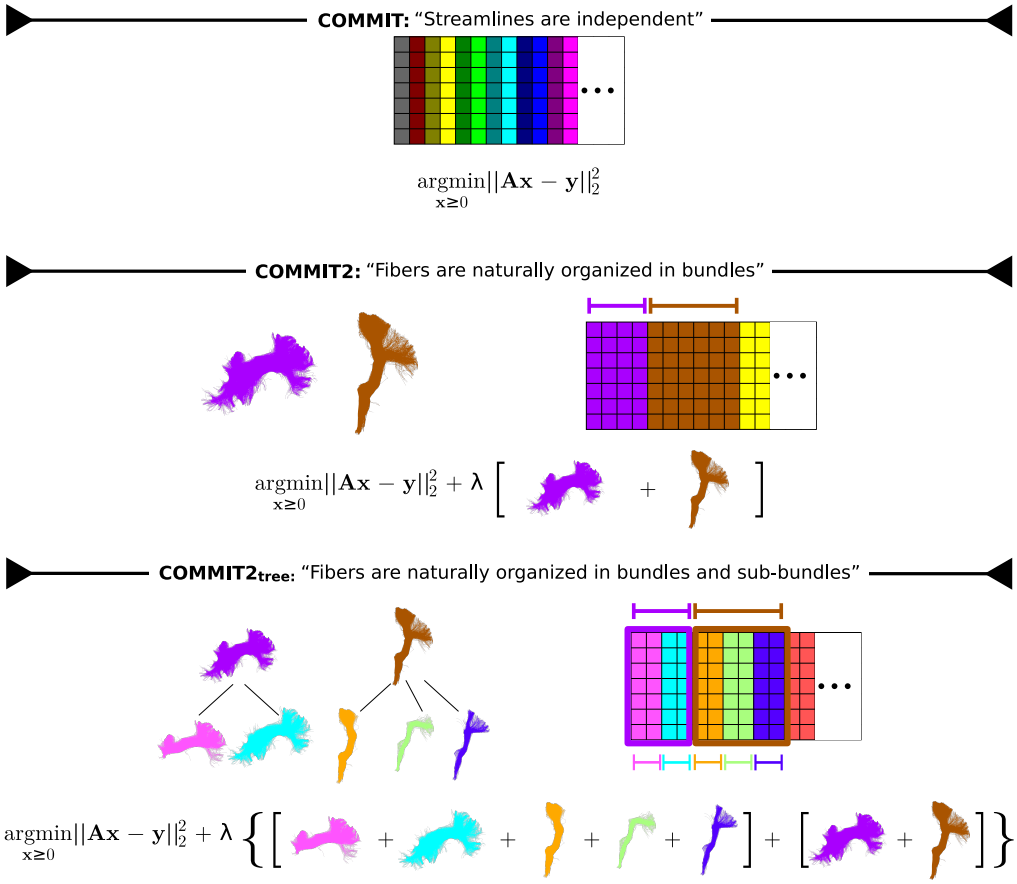

Figure 5.2: **Visual comparison between the COMMIT, COMMIT2, and COMMIT2$_{\text{tree}}$ formulations.** COMMIT considered the streamlines as independent entities and COMMIT2 added a regularization term to take into account that streamlines are instead naturally organized in bundles. With COMMIT2$_{\text{tree}}$ we propose to improve this regularization by allowing a multilevel hierarchical organization of the streamlines, where every bundle may be composed of several sub-bundles and each can be selectively promoted or penalized.

dataset, a generic tractography algorithm (top row, center) reconstructed the three true-positive streamlines as well as two false positives (S4 and S5). This tractogram was then filtered with COMMIT, COMMIT2, and COMMIT2$_{\text{tree}}$. Without any prior information, COMMIT keeps all five streamlines (top row, right), as they are all compatible with the underlying data. COMMIT2 groups streamlines based on a partition with a single level and attempts to find solutions that explain the data with the minimum number of groups. If large groups are used (bottom row, left), e.g., streamlines that connect the same pair of ROIs, the group formed by S3 and S4 is necessary to explain the data in the top-right voxel, which is covered only by S3. Therefore both S3 and S4 are

kept even though S4 is a false positive. This choice, in turn, requires to keep also S5 to explain the data in the remaining voxels using the minimum number of groups. This causes the removal of the true positives S1 and S2 because they are no longer necessary to fit the data. In general, if small groups are used (bottom row, center), e.g., dividing B into two sub-regions B1 and B2, and C into C1 and C2, we obtain more groups consisting of fewer streamlines each; in this example, every group has a single streamline. This situation contains many ambiguous configurations as saw before for COMMIT (top row, right) and, as groups are treated as independent entities, these ambiguities cannot be solved. Please note that this situation was already analyzed in Chapter 4 (see Figure 4.6). On the contrary, the grouping implemented in COMMIT2$_{\text{tree}}$ is more flexible and helps to disentangle ambiguous configurations such as the one presented here. In fact, according to the hierarchical structure, the group S3-S4 can be further subdivided into two groups (bottom row, right), i.e., one containing the true positive S3 and the other one the false-positive S4. This allows COMMIT2$_{\text{tree}}$ to remove all the false positives and keep the true positives.

5.1.2 Data and experiments

We demonstrate the improvements of COMMIT2$_{\text{tree}}$ over the previous formulation using a hierarchical structure with only two levels; however, our proposed formulation can easily accommodate any number of levels. In the first level, we grouped the streamlines connecting the same pair of cortical regions as in COMMIT2. Then, to capture the presence of possible sub-bundles, we constructed a second level where we subdivided these parcellation-based groups by clustering the streamlines in each group with QuickBundles (Garyfallidis et al., 2012). In brief, QuickBundles is an unsupervised clustering algorithm for tractography datasets which does not require knowing the number of clusters in advance, but it rather uses a threshold to group streamlines based on distance metrics. In this work, we used the Average of Pointwise Euclidean Metric. The algorithm is very fast and well suited for large tractograms, as its complexity is $O(kN)$, where k is the number of clusters and N the number of streamlines (for technical details see (Garyfallidis et al., 2012)). For a more direct comparison with COMMIT2, we adopted the same forward model as in (Schiavi et al., 2020), which associates a contribution to each streamline proportional to its cross-sectional area using a map of the intra-axonal signal fraction (IASF).

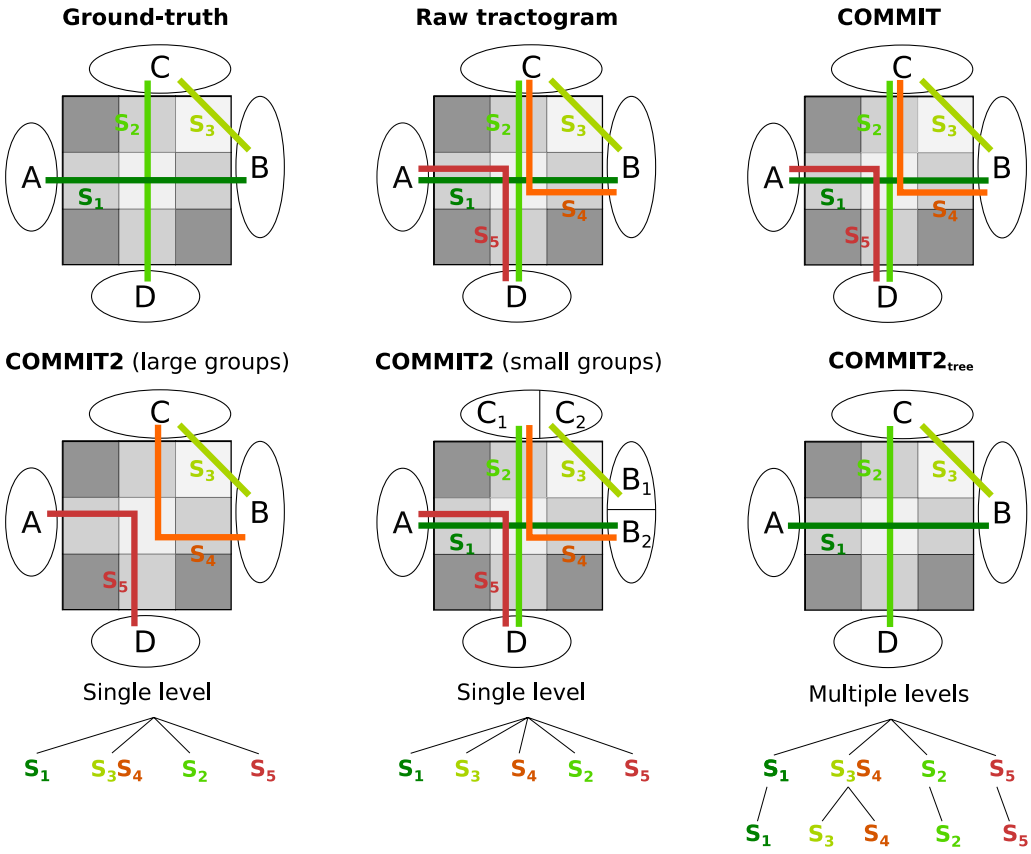

Figure 5.3: **Illustrative toy example.** First row: ground-truth streamlines configuration as well as representative streamlines reconstructed with a generic tractography algorithm, i.e., raw tractogram, and after filtering with COMMIT. Second row: results after filtering with COMMIT2 (single level, once using large groups and another with small groups) and COMMIT2$_{\text{tree}}$ (multiple levels, combining parcellation and clustering). S1, S2, and S3, in green shades, represent true-positive streamlines while S4 and S5, in red shades, are false positives.

5.2 Results

5.2.1 Quantitative evaluation on synthetic data

To quantitatively evaluate the performance of our proposed formulation with respect to COMMIT2, we adopted the same synthetic phantom used in (Schiavi et al., 2020). We compared the sensitivity and specificity of the tractograms after filtering with both techniques by assessing the number of valid bundles (VB), i.e., true-positive connections in the corresponding connectomes, and invalid bundles (IB), i.e., false-positive ones. The phantom is shown in Figure 5.4A and consists of 27 ground-truth bundles between 53 ROIs that mimic challenging configurations like branching, kissing, and

crossing with different curvatures and sizes (Caruyer et al., 2014). The IASF map of this phantom was computed from the ground-truth geometry. The corresponding DW-MRI signal was generated using the Composite Hindered And Restricted Model of Diffusion (CHARMED) (Assaf and Basser, 2005) along 64 directions with $b = 3000\,\mathrm{s/mm^2}$ and Rician noise was added with a signal-to-noise ratio of 30. All tractograms and the corresponding connectomes were estimated using the MRtrix3 software (Tournier et al., 2019). First, we computed the fiber orientation distributions in each voxel using Constrained Spherical Deconvolution (Tournier et al., 2007). Then, we reconstructed 1 million streamlines with both deterministic (Tournier et al., 2012) and probabilistic (Tournier et al., 2010) algorithms, using a white matter mask as seeding region and default parameters. Finally, we assigned each endpoint of a streamline to a node if that point fell within 2 mm from one of the 53 gray matter ROIs. A streamline was considered as connecting two nodes if both endpoints were assigned, otherwise it was discarded from the analysis.

Figure 5.4 compares the sensitivity and specificity of the tractograms estimated from the synthetic data with both deterministic and probabilistic tracking, before and after filtering with COMMIT2 and COMMIT2$_{\text{tree}}$. As a reference, results with COMMIT are also reported. All reconstructions included the 27 true-positive bundles and, as expected, the raw tractograms were contaminated by a large number of false-positive bundles, respectively IB=441 (probabilistic) and IB=235 (deterministic). Only a few IB were removed with COMMIT, whereas COMMIT2 was able to drastically reduce them from 441 to 20 (probabilistic) and from 235 to 17 (deterministic). Using the proposed multilevel regularization, COMMIT2$_{\text{tree}}$ was able to further improve these results, although not substantially. Using different distance metrics in the clustering did not produce particular effects on the results (see Figure 5.5), probably due to the simple geometry of this phantom.

5.2.2 Qualitative evaluation on in vivo data

To appreciate the improved quality of the tractograms, we visually inspected known true- and false-positive bundles in 10 subjects (5 males and 5 females of ages 26–30) of the HCP (Essen et al., 2013). These bundles were extracted with RecobundlesX (Garyfallidis et al., 2018; Rheault, 2020), a multi-atlas, multi-parameter segmentation tool that uses bundles manually segmented by an expert neuroanatomist as reference, the procedure is described in Chapter 3. We performed RecobundlesX using nine different

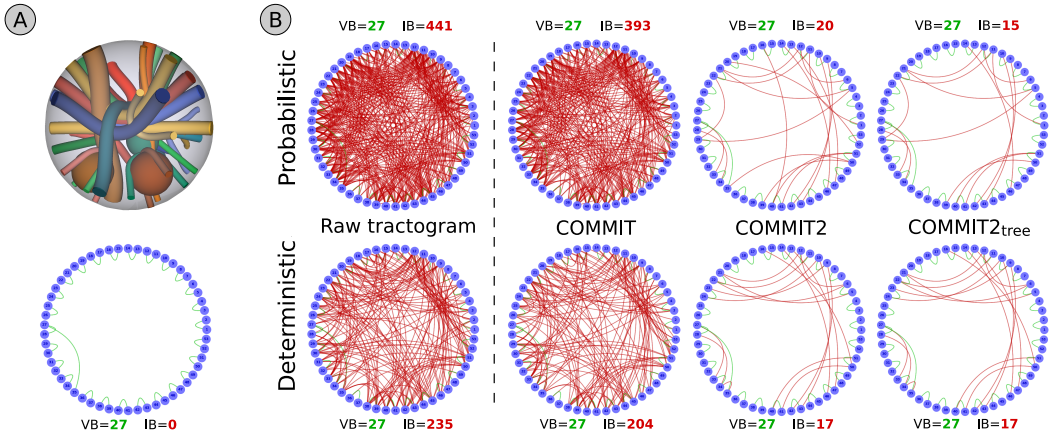

Figure 5.4: **Quantitative comparison on synthetic data between COMMIT2 and COMMIT2$_{\text{tree}}$.** We compared the valid (VB, reported in green) and invalid (IB, reported in red) bundles in the connectomes generated on a synthetic phantom (A, top) for which we know the ground-truth connectivity (A, bottom). Panel B compares the quality of the connectomes estimated from the probabilistic (top row) and deterministic (bottom row) tractograms before (raw tractogram) and after filtering with COMMIT2 and COMMIT2$_{\text{tree}}$; performances of COMMIT are reported for reference.

parameter configurations and a threshold for the voting system of 75%. If a streamline had been selected as true positive, it was not taken into account in the segmentation of the false-positive bundles. The intersections of streamlines in different bundles were eliminated, that is, each streamline could only belong to one bundle. We also reported the voxel coverage of each of them, i.e., the number of voxels traversed by the streamlines associated with each bundle. We segmented the T1-weighted image using the FMRIB's Automated Segmentation Tool (FAST) (Zhang et al., 2001) to derive the multi-tissue image and perform the multi-shell, multi-tissue constrained spherical deconvolution (Jeurissen et al., 2014) on the preprocessed DW-MRI data (Glasser et al., 2013). We generated 5 million streamlines of length between 20 mm and 200 mm with the probabilistic algorithm (Tournier et al., 2010), using Anatomically Constrained Tractography (Smith et al., 2012) and default parameters. As in the synthetic experiments, the white matter mask was used as a seeding region. The IASF map needed by the forward model used in COMMIT2 and COMMIT2$_{\text{tree}}$ was computed using the Spherical Mean Technique (Kaden et al., 2016a). Besides inspecting individual bundles, we also compared the resulting connectomes, which were created using the 85 gray matter ROIs defined in the Desikan-Killiany atlas (Desikan et al., 2006) derived

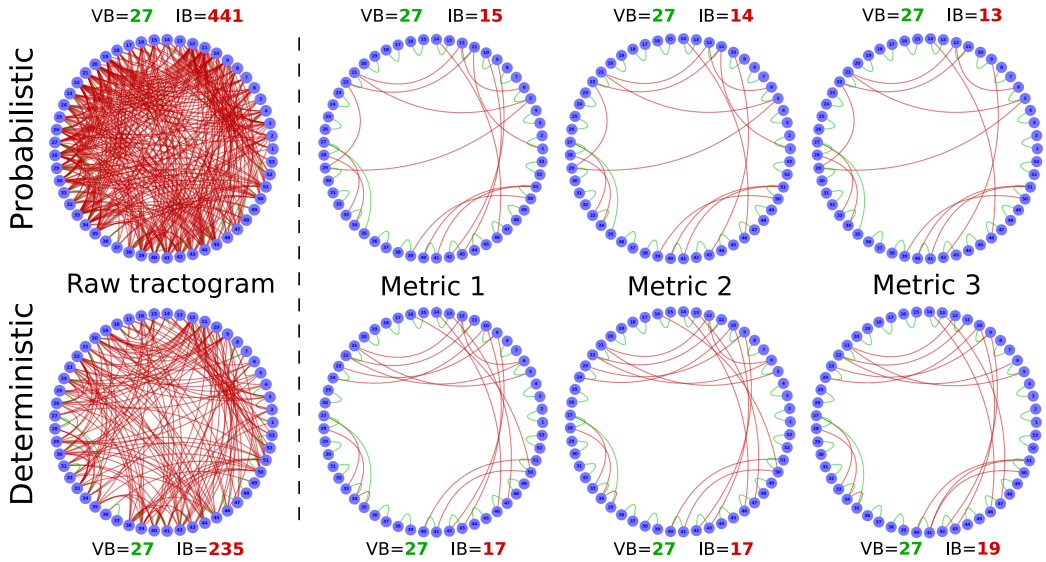

Figure 5.5: **Impact of the distance metric on the quality of the tractograms filtered with COMMIT2$_{\text{tree}}$.** Following the same notation as Figure 5.4, we evaluated in the synthetic phantom the effect of changing the clustering metric to build the second level of the hierarchy. We tested the following metrics (see `https://www.dipy.org/` for more details): Metric 1 is the Average of Pointwise Euclidean Metric between streamlines (same as Figure 5.4), Metric 2 is the Euclidean Metric between the centers of mass of the streamlines, and Metric 3 is the Cosine Similarity between the vectors of the streamline endpoints.

from the T1-weighted images using FreeSurfer[1], and replacing the brainstem with its last part, i.e., medulla oblongata (Iglesias et al., 2015). Finally, as edge weights, we used the streamline count for the raw tractograms and the sum of the estimated streamline contributions for COMMIT2 and COMMIT2$_{\text{tree}}$. For each connectome, we report its density, i.e., the ratio between the actual and the possible connections.

Figure 5.6 evaluates the effectiveness of the multilevel formulation in real brain data, where the fiber configurations are expected to be more complex. We qualitatively compared known true- and false-positive bundles obtained in one HCP subject after filtering the tractograms with COMMIT2 and COMMIT2$_{\text{tree}}$. The volume coverage of the bundles is reported in terms of the number of voxels and, in the last two cases, we also report the estimated contributions (weight). The filtering with COMMIT2 does not negatively affect the true-positive bundles, i.e., their volume is comparable with the raw tractogram, and, as expected, the false-positive bundles are sensibly thinned,

[1] `http://surfer.nmr.mgh.harvard.edu/`

i.e., reduced volume coverage. The introduction of the additional level in the regularization term of COMMIT2$_{\text{tree}}$ further improved these performances. On the one hand, the voxel coverage of the true-positive bundles is comparable but the estimated contributions are larger, which translates into a higher likelihood to be true positives. On the other hand, the contributions of the false positives are further reduced and all of them are almost completely removed. These results were consistent across all the ten subjects (Table 5.1).

		INPUT	**COMMIT2**		**COMMIT2$_{\text{tree}}$**	
		voxels	*voxels*	*weight*	*voxels*	*weight*
True positives	*#1*	18,968 ± 5,229	12,983 ± 4,997	2.92 ± 1.80	10,678 ± 4,421	2.82 ± 2.12
	#2	39,920 ± 3,637	30,892 ± 4,108	3.88 ± 1.82	21,160 ± 5,285	3.90 ± 2.15
	#3	44,899 ± 2,995	37,840 ± 3,143	12.73 ± 3.24	31,203 ± 3,780	14.76 ± 4.15
	#4	28,403 ± 3,681	26,101 ± 3,372	18.95 ± 4.16	24,243 ± 3,214	17.99 ± 4.13
	#5	57,300 ± 6,645	43,324 ± 7,729	10.03 ± 4.39	34,406 ± 6,835	14.26 ± 5.52
False positives	*#1*	19,362 ± 4,924	7,847 ± 3,134	0.09 ± 0.04	1,211 ± 1,256	<0.01 ± 0.01
	#2	22,037 ± 5,221	4,110 ± 6,605	0.04 ± 0.08	229 ± 686	<0.01 ± 0.01
	#3	10,066 ± 6,567	3,617 ± 3,077	0.05 ± 0.05	1,333 ± 1,511	0.02 ± 0.03
	#4	20,908 ± 7,060	10,805 ± 3,720	0.13 ± 0.08	897 ± 2,036	0.01 ± 0.02
	#5	11,243 ± 5,714	3,876 ± 3,013	0.03 ± 0.03	474 ± 634	0.01 ± 0.02

Table 5.1: **Stability across the ten HCP subjects**. Voxel coverage (*voxels*) and estimated sum of streamline contributions (*weight*) of the 5 true-positive bundles and the 5 false-positive bundles shown in Figure 5.6. *True positives*: #1 (yellow), #2 (dark blue), #3 (cyan), #4 (fuchsia), #5 (dark red). *False positives*: #1 (green), #2 (light red), #3 (orange), #4 (light blue), #5 (magenta).

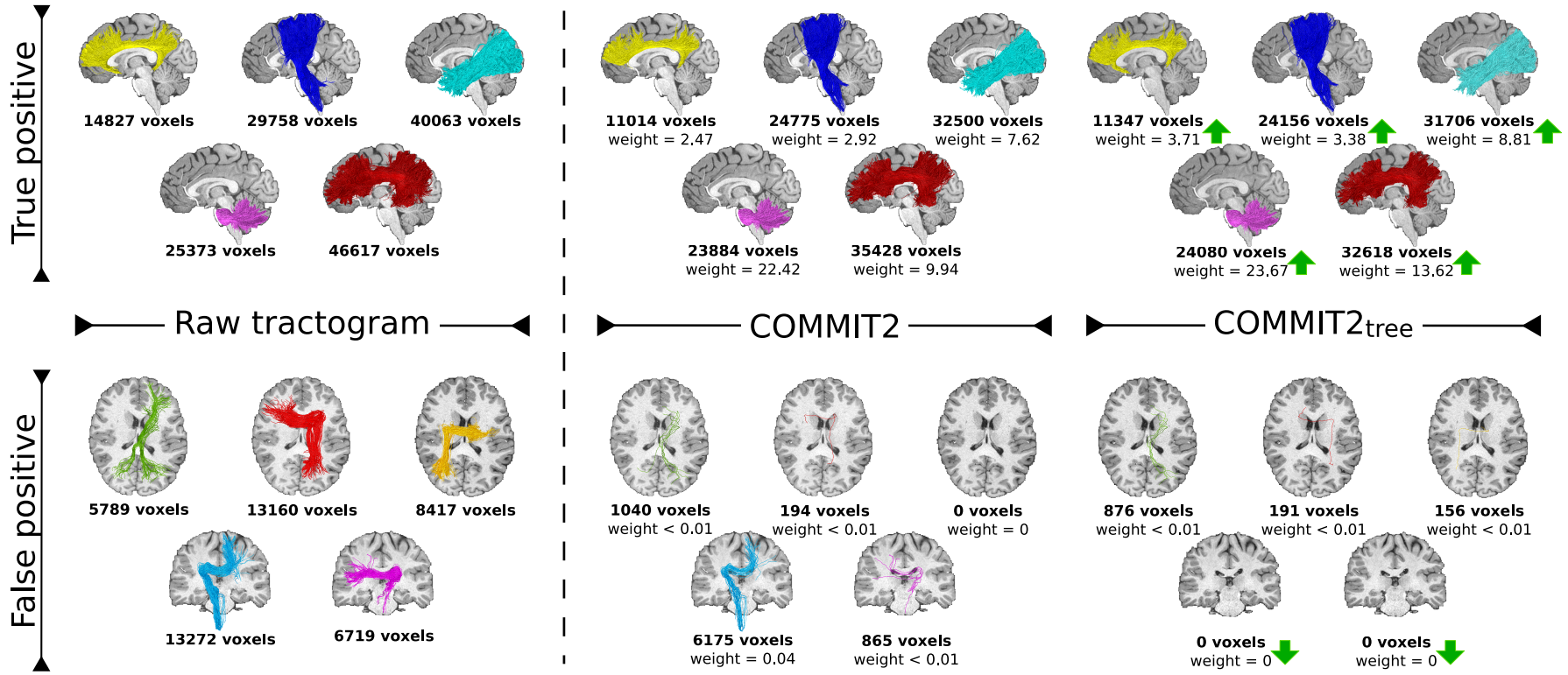

Figure 5.6: **True- and false-positive bundles estimated in one HCP subject.** We report the raw tractogram and after filtering it with COMMIT2 and COMMIT2$_{\text{tree}}$. The voxel coverage is reported for all the bundles, and for the filtered ones, it is also reported the sum of the streamline contributions estimated (weight). The performance of both methods is similar, the true positives keep comparable coverage to the raw tractogram, and the false positives are drastically reduced. Green arrows highlight the cases where COMMIT2$_{\text{tree}}$ assigned larger contributions to the true positives and further reduced the false-positive bundles than COMMIT2.

To better appreciate the improved anatomical accuracy of the tractograms, in Figure 5.7 we visually inspect two representative bundles as reconstructed in each of the ten subjects. They correspond to the streamlines connecting the medulla oblongata to, respectively, the right precentral gyrus (Bundle 1) and the left precentral gyrus (Bundle 2). As can be seen, these bundles have streamlines that are coherent and well organized in two sub-bundles, and one of these describes an implausible pathway passing through the corpus callosum. The streamlines in the raw tractogram are colored based on their local orientation, whereas for COMMIT2 and COMMIT2$_{\text{tree}}$ they are colored according to the estimated sum of the streamline contributions in each sub-bundle. To make this visual comparison more effective, we use two different colormaps, *cool* for the true-positive streamlines and *hot* for the false positives. As expected, since COMMIT2 treats all the streamlines in each bundle as a whole, it is not able to completely remove any false-positive sub-bundles that are included in such bundles. However, if subgroups of streamlines are considered in the filtering as done in COMMIT2$_{\text{tree}}$, it is possible to assign low contributions to these false positives or even remove them completely. For all the subjects, there is an evident improvement using COMMIT2$_{\text{tree}}$: lower values are assigned to all the false positives as compared to COMMIT2, e.g., yellow and green arrows, and in some subjects, it was able to completely remove them. Moreover, COMMIT2$_{\text{tree}}$ assigned higher contributions than COMMIT2 to all the true positives. We can also appreciate that the patterns of the streamlines of these two bundles are consistent across subjects. Table 5.2 reports the mean and standard deviation among the ten subjects of the sum of the streamline contributions and the voxel coverage for each sub-bundle.

		COMMIT2		**COMMIT2$_{\text{tree}}$**	
		voxels	*weight*	*voxels*	*weight*
Bundle 1	TP	20,280 ± 2,159	2.75 ± 0.81	17,733 ± 2,181	3.18 ± 0.76
	FP	9,325 ± 3,471	0.14 ± 0.08	2,842 ± 2,689	0.01 ± 0.01
Bundle 2	TP	20,252 ± 2,577	2.97 ± 0.71	17,819 ± 2,166	3.41 ± 0.76
	FP	10,195 ± 3,876	0.18 ± 0.12	4,122 ± 4,300	0.02 ± 0.02

Table 5.2: **Quantitative comparison across the ten HCP subjects of the sub-bundles presented in Figure 5.7**. Mean and standard deviation of the sum of the streamline contributions (weight) and voxel coverage (voxels) for the true-positive (TP) and false-positive (FP) sub-bundles. Bundle 1: Medulla oblongata and Precentral gyrus left. Bundle 2: Medulla oblongata and Precentral gyrus right.

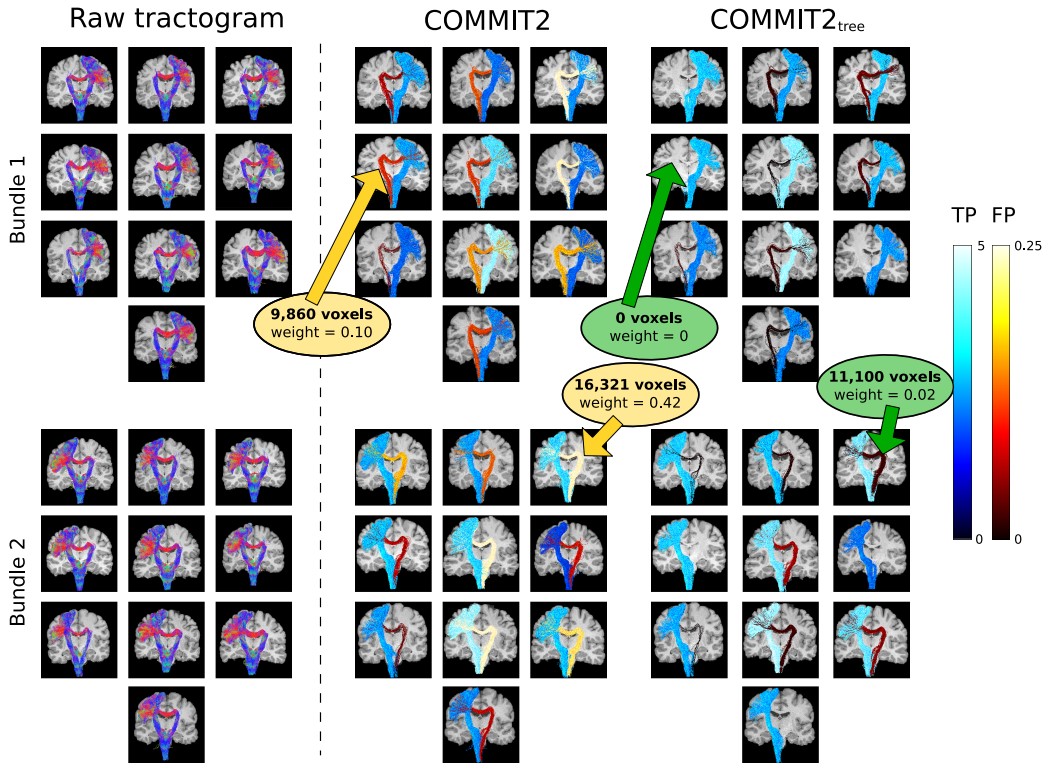

Figure 5.7: **Visual inspection of two representative bundles across the ten HCP subjects.** Reconstructed streamlines belonging to two representative bundles which connect, respectively: medulla oblongata with the precentral gyrus left (Bundle 1), and medulla oblongata with the precentral gyrus right (Bundle 2), as obtained across the ten subjects before (raw tractogram) and after filtering the tractograms with COMMIT2 and COMMIT2$_{\text{tree}}$. For display and visual inspection purposes, the filtered bundles of streamlines are divided into two sub-bundles, true positives (TPs) and false positives (FPs), these definitions were not used in the filtering procedure. The colormaps display the sum of the streamline contribution per sub-bundle, *cool* for TPs and *hot* for FPs. For all the bundles, the contributions estimated with COMMIT2$_{\text{tree}}$ are better than the ones estimated with COMMIT2, the FPs have smaller contributions and the TPs are more significant. The yellow and green arrows point to the region in the raw tractogram with false-positive sub-bundles after filtering with COMMIT2 and COMMIT2$_{\text{tree}}$, respectively, highlighting their voxel coverage and the sum of the streamline contributions.

Figure 5.8 compares the estimated connectomes in one HCP subject before and after filtering the tractogram reconstructed with probabilistic tractography with COMMIT2 and COMMIT2$_{\text{tree}}$. To assess how well each filtered tractogram explains the input data, we report the input IASF map used for the filtering and the one predicted from the filtered tractograms, as well as the root mean square error (RMSE) between the input and the

fitted maps. We observe that the connectome of the raw tractogram is very dense (density=0.896), which is an expected result for probabilistic tracking, whereas after the filtering with COMMIT2 and COMMIT2$_{\text{tree}}$, the connectomes are sparser and have comparable density between them (0.245 and 0.307, respectively). Despite sparser, the corresponding tractograms seem to explain well the input IASF map; the RMSE map is comparable and shows very small errors in the white matter, with higher values located in voxels at the interface with cortical and subcortical gray matter.

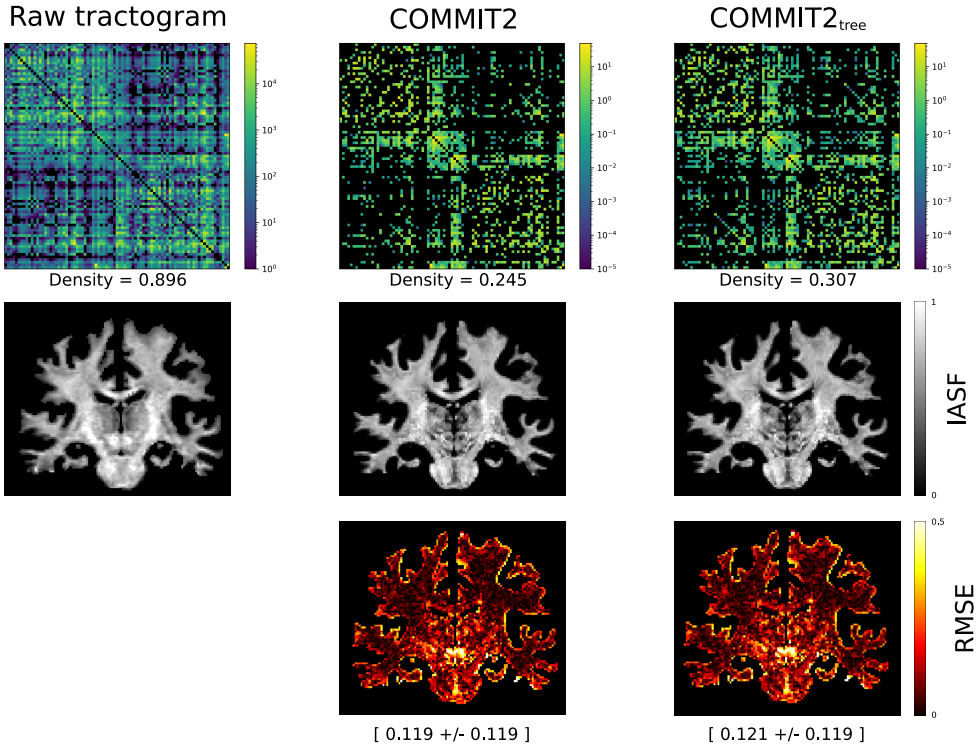

Figure 5.8: **Connectomes estimated in one HCP subject.** In the first row, we show the estimated connectomes; in the case of the raw tractogram, we used the number of streamlines, whereas for COMMIT2 and COMMIT2$_{\text{tree}}$ the sum of the streamline contributions was used. In the second row, we present the intra-axonal signal fraction (IASF) maps used as input and estimated to perform a visual inspection. The third row presents root mean square error (RMSE) maps of the estimations, along with their mean and standard deviation for a quantitative comparison.

5.3 Discussion

Tractography is a unique technique that is able to describe the major neural pathways in white matter. In the last decades, it has been used to

study the structural network organization of the brain, but its anatomical inaccuracy and limitations have been exposed in different studies (Thomas et al., 2014; Drakesmith et al., 2015; Zalesky et al., 2016; Maier-Hein et al., 2017; Schilling et al., 2019; Girard et al., 2020; Rheault et al., 2020b). One of the major limitations still unresolved is the intrinsic trade-off between specificity and sensitivity. In a recent international challenge (Maier-Hein et al., 2017), it was suggested that a possible way to overcome this issue would be to inject microstructural and anatomical prior during tractography reconstruction. A step forward in this direction was achieved by the recent work of Schiavi et al. (2020), where microstructure informed tractography was combined with the anatomical prior that white matter fibers (axons) are organized in fascicles giving origin to COMMIT2. Using the prior knowledge that bundles are organized in sub-bundles (Chenot et al., 2019; Mandonnet et al., 2018), in this work we extended COMMIT2 proposing the use of a multilevel organization of the streamlines in order to identify streamlines following implausible trajectories inside valid bundles. This new formulation, called COMMIT2$_{\text{tree}}$, considers partitions of the streamlines with different granularity and organizes them in a hierarchical structure which provides more degrees of freedom than COMMIT2 but in a constrained clever way. The subgroups used in COMMIT2$_{\text{tree}}$ share anatomical constraints like the starting and ending region in the gray matter, but they have different geometrical properties, i.e., the trajectory. Figure 5.7 clearly shows that by considering this way of grouping in the optimization, more false-positive streamlines inside true-positive bundles are removed, boosting further the accuracy of the final tractogram.

In synthetic data, the connectivity graphs obtained after filtering the tractograms with COMMIT2 and COMMIT2$_{\text{tree}}$ showed comparable results. However, the simple geometry of this phantom does not allow us to fully exploit the advantages of our proposed multilevel regularization, as the bundles consist of regular and smooth tubes. Nonetheless, our findings indicate that this enhanced formulation results in a stable and robust regularization of the original problem. In particular, Figure 5.4 shows that adding more levels to the structure does not affect the stability of the method, but can slightly improve the quality of the estimated tractograms.

To evaluate the quality of the in vivo reconstructions, we analyzed ten HCP subjects and we looked both at the anatomical accuracy of individual bundles and at the overall structural connectivity estimated after filtering the

tractograms with COMMIT2 and COMMIT2$_{\text{tree}}$. The density of the filtered connectomes was about one-third of the unfiltered one, showing again similar performances of both methods. These results confirm and extend the results presented in (Schiavi et al., 2020), which were in agreement with the theory of the economy of brain networks (Bullmore and Sporns, 2012). However, when looking more closely at the individual bundles, before and after the filtering, it is evident that a significant improvement was achieved by COMMIT2$_{\text{tree}}$. In fact, in Figure 5.6 and Table 5.1 we can appreciate how COMMIT2$_{\text{tree}}$ was able to filter more the false-positive bundles than COMMIT2 without negatively affecting the true positives, in particular, because of its capability to remove invalid streamlines inside valid bundles (Figure 5.7 and Table 5.2). From a quantitative point of view, we observe that both methodologies assigned lower contributions to the false positives than the true positives; notably, it is important to note that COMMIT2$_{\text{tree}}$ assigned higher contributions to the true positives and smaller values to the false positives as compared to its predecessor. This is an important property when one is interested in network properties relying on connections strengths.

Although COMMIT2$_{\text{tree}}$ was able to further improve the anatomical accuracy of the tractograms, it did not eliminate completely all known false positives in every analyzed subject. This may be partly due to the regularization parameter λ used and to the actual groups created with clustering in each subject. First, in our experiments, we used the same regularization strength for all subjects, which was empirically determined as the value that overall produced visually satisfactory results. However, optimizing the value of λ on a subject-specific basis might considerably improve the performance of the filtering. Second, the results presented here show that the quality of the anatomical prior, i.e, structure definition and how streamlines are grouped, plays a fundamental role in the optimization procedure. The original COMMIT was only data driven and the filtering did not improve significantly the anatomical accuracy of the tractograms; COMMIT2 added the prior that white matter fibers are organized in fascicles which, instead, had a big positive impact on the performance. In COMMIT2$_{\text{tree}}$ we added geometrical priors based on the trajectories described by the streamlines and we built a hierarchical structure to combine both anatomical (based on which gray matter regions the streamlines connect) and geometrical (clustering the streamlines based on their trajectory) information. However, different definitions of structures can be implemented in our formulation. For

example, we could use more than two levels to create the hierarchy as well as explore different strategies to group the streamlines and inject additional prior information, e.g., see (Côté et al., 2015; Guevara et al., 2011; Siless et al., 2018; Vázquez et al., 2020) and references therein. All these aspects will be the subject of future research.

It is worth noting that using a finer partitioning of the streamlines may create groups that might capture better the plausible and implausible sub-bundles; for instance, in the extreme case where all groups have a cardinality equal to 1, i.e., they consist of a single streamline, true- and false-positive streamlines are clearly separated in distinct groups. However, as the granularity of this partitioning becomes smaller, the number of generated groups increases accordingly. But since the groups are treated as independent entities in the penalty term in Eq. 5.1, this process has the side effect of gradually reintroducing the ambiguous configurations that, instead, COMMIT2 was able to disentangle using a coarser partition. Figure 5.9 shows that, indeed, the performances gradually deteriorate as the groups become smaller. As it is not possible to predict a priori the behavior of the algorithm using partitions with different granularity, our proposed approach represents an effective way to consider and take advantage of more than one granularity in the filtering procedure. Clearly, future research will be required to identify the optimal configuration of groups in this multilevel structure.

Finally, it is important to note that the proposed approach is still a filtering procedure, so even if it can be applied on any type of input tractograms (coming from either deterministic or probabilistic tractography approaches), it is still limited on the quality of the input reconstruction. Clearly, if a bundle is not present in the original tractogram it will not be recovered by COMMIT2$_{\text{tree}}$. So, particular attention should be given to this aspect. Another important factor that affects the results is the selection of the regularization parameter λ. As it was analyzed in Chapter 4 (see Figure 4.4), a high value of this parameter would result in a very strong filtering and would end up in removing too many connections. On the contrary, a too low value would end up in removing only a few. Up until now, and for both COMMIT2 and COMMIT2$_{\text{tree}}$ formulations, we do not know a close formula to define the best value of this parameter according to the input tractogram, signal, and structure for grouping the streamlines. Thresholds for upper and lower bounds when using the adaptive Group Lasso approach like ours have been suggested for the case of independent and identically distributed columns of the matrix $\mathbf{A}$, but they still need to be

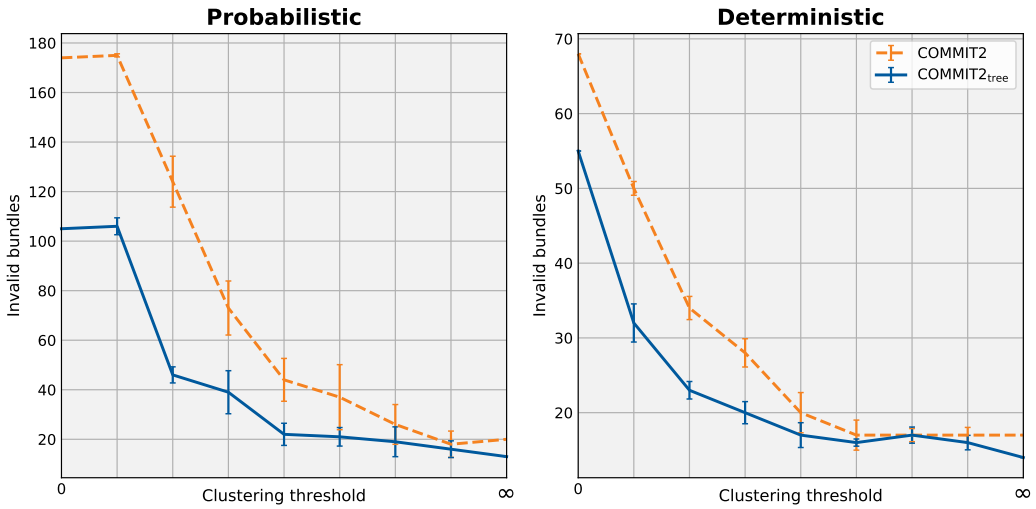

Figure 5.9: **Impact of the group size on the quality of the tractograms filtered with COMMIT2$_{\text{tree}}$.** In the synthetic phantom, we investigated the effect of changing the size of the groups to build the second level of the hierarchy, by changing the threshold of the Average of Pointwise Euclidean Metric between streamlines from 0 (one streamline per cluster) to "infinity" (bundles are not divided into clusters). We repeated the clustering 10 times and, here, we report the mean and standard deviation of invalid bundles kept after filtering with COMMIT2$_{\text{tree}}$ (continuous blue line) and, for comparison, COMMIT2 (orange dashed line).

generalized to our case. In the experiments presented in this work the choice was made based on the knowledge we have on known bundles: i.e., we choose the largest value that was able to filter out the known invalid bundles from the input tractogram while keeping all the known valid ones.

Chapter 6

Outlier adjusted tractogram weighting

Weighting tractography reconstructions can be biased if the DW-MRI measurements are unreliable due to partial volume or artifacts (Sairanen et al., 2018). In the forward modeling of the COMMIT framework (Daducci et al., 2013, 2015), a weight is assigned to each streamline to represent its contribution to the predicted DW-MRI signal. Weights are iteratively updated based on a chosen cost function until implausible streamlines are filtered out and the algorithm converges to a prediction that is the closest to the original measurements by solving a non-negative least squares (NNLS) problem. If a weight becomes zero, the corresponding streamline will be rejected as not compatible with the measured signal. Minimization approaches based on NNLS are suited only for voxels that can be correctly described by the chosen microstructural model. If a streamline traverses a voxel that partially or fully consists of grey matter (GM) or data is partially unreliable, the microstructural model for white matter WM would be incorrect to predict the corresponding signal in that voxel.

In this Chapter, we present a robust augmentation to COMMIT that adjusts for the reliability of the original measurements. The reliability can be estimated with respect to the used microstructural model or to the overall quality of the data which could be decreased by outliers or artifacts (Sairanen et al., 2018), for the purposes of this work, we focus on the former.

6.1 Materials and Methods

6.1.1 Weighted minimization

Consider a simple linear problem as *a toy example* $\mathbf{y} = a \cdot \mathbf{x} + b$. Estimation of coefficients $\mathbf{x} = [x_0, x_1]^T$ from measurements $\mathbf{y} = [0, 1, 2]$ can be described using matrix formulation as Eq. 6.1 below:

$$\underbrace{\begin{bmatrix} 0 \\ 1 \\ 2 \end{bmatrix}}_{\mathbf{y}} = \underbrace{\begin{bmatrix} 1 & 0 \\ 1 & 1 \\ 1 & 2 \end{bmatrix}}_{\mathbf{A}} \underbrace{\begin{bmatrix} x_0 \\ x_1 \end{bmatrix}}_{\mathbf{x}}, \tag{6.1}$$

with $\mathbf{A}$ being a design matrix. Estimates for the coefficients $\hat{\mathbf{x}} = [0, 1]^T$ can be computed with a linear least squares solver:

$$\hat{\mathbf{x}} = \left(\mathbf{A}^T\mathbf{A}\right)^{-1}\mathbf{A}^T\mathbf{y}, \tag{6.2}$$

with the root mean square error (RMSE) of 0. However, if an outlier is introduced, e.g. $y_0 = 3$, the coefficients would be incorrectly estimated as $\hat{\mathbf{x}} = [2.5, -0.5]^T$ with the RMSE of 0.71.

Similar real-world problems of *unreliable measurements* have already been encountered in the processing of DW-MRI voxel-wise data, and the weighted linear least squares method has been proposed to solve them with good success (Veraart et al., 2013). If we have obtained prior information on the reliability of the measurements via e.g. statistical analysis of the original measurements $\mathbf{y}$ (Sairanen et al., 2018), we can use that information to weight down the unreliable measurements in COMMIT. This can be described as a *weighted linear least squares* estimation (Veraart et al., 2013):

$$\hat{\mathbf{x}} = \left(\mathbf{A}^T\mathbf{W}\mathbf{A}\right)^{-1}\mathbf{A}^T\mathbf{W}\mathbf{y}, \tag{6.3}$$

where the diagonal of the weight matrix $\mathbf{W}$ contains the measurement-wise reliability estimates and the off-diagonal elements are zero. In our example, this diagonal would be a vector $\mathbf{w} = [0, 1, 1]$, with the outlier having zero reliability and the rest of the measurements being fully reliable, if the outlier was correctly identified during any pre-processing step. Estimating the model coefficients with Eq. 6.3 would provide the original and correct $\hat{\mathbf{x}} = [0, 1]^T$ with

the RMSE of 1.7. Thus, despite the model being more accurately estimated, we would end up obtaining a higher RMSE due to its definition depending on the original measurements which were partially unreliable. Because of this, an approach that considers the level of reliability can be better, like the weighted RMSE (RMSE_w):

$$\text{RMSE}_w = \sqrt{\frac{\sum_{i=1}^{N} W_{ii} \left(A_i \hat{x}_i - y_i\right)^2}{\sum_{i=1}^{N} W_{ii}}}. \tag{6.4}$$

The weighted RMSE in Eq. 6.4 reduces to the normal RMSE if all the measurements are equally reliable. To continue on our example for which Eq. 6.3 provided exact results but the RMSE was 1.7, the weighted RMSE would be 0. Although the forward models used in COMMIT (Daducci et al., 2013, 2015; Schiavi et al., 2020; Ocampo-Pineda et al., 2021) are more complex than this example, the same principle applies: the modeling and minimization should account for the reliability of the measurements. To this end, we propose an augmented cost function to COMMIT in (6.5) as an adjustment to these novel reliability weights:

$$\underset{\hat{\mathbf{x}} \geq 0}{\text{argmin}} \frac{1}{2} \left\| \mathbf{W}^{1/2} \left(\mathbf{A}\hat{\mathbf{x}} - \mathbf{y} \right) \right\|_2^2, \tag{6.5}$$

where $\mathbf{W}^{1/2}$ is a diagonal matrix with the ith diagonal entry being $\sqrt{W_{ii}}$.

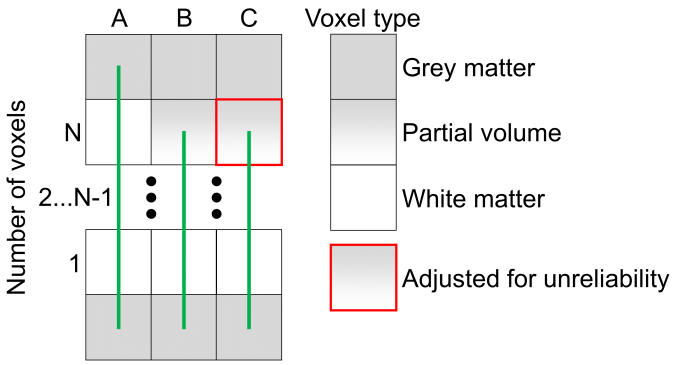

Figure 6.1: **Description of the synthetic fiber phantom.** (A) In the baseline, a streamline begins in a GM voxel, traverses through N WM voxels, and ends in a GM voxel. (B) The last voxel is affected by partial volume causing the streamline to end prematurely in the middle of the voxel. (C) Similar to (B) but now the last voxel is adjusted for the unreliability.

6.1.2 Data and experiments

We generated a simple synthetic fiber phantom, described in Figure 6.1, with three different setups to evaluate the robust weighting algorithm performances with varying streamline lengths. In the baseline setup (A), a single streamline traverses through N WM voxels. In the setup (B), the last voxel is affected by partial volume effect with 70% signal from GM and 30% signal from WM causing the streamline to end prematurely in the middle of the voxel. The setup (C) is otherwise identical to (B) but the last voxel is identified as being corrupted by GM and the corresponding reliability weight w_N is reduced.

Signal simulations for WM and GM were performed using the stick and ball model implemented in the *dmipy* library (Fick et al., 2019). We used the parallel and isotropic diffusivities of $1.7 \cdot 10^{-9}\mathrm{m}^2/\mathrm{s}$ and $3.0 \cdot 10^{-9}\mathrm{m}^2/\mathrm{s}$ (Zhang et al., 2012) with signal fraction of 3:1 in WM. The GM simulation was composed only of the ball compartment. We used the Human Connectome Project's (HCP) gradient scheme (Essen et al., 2013) to simulate the DW-MRI signals with 300 noise iterations for all setups. We applied Rician noise with a non-diffusion-weighted signal-to-noise ratio of 20 (Maier-Hein et al., 2017) to all voxels.

The preliminary human studies were conducted using the preprocessed and B1-field corrected DW-MRI data of the subject 100307 from the HCP project. We used probabilistic (Tournier et al., 2010) anatomically constrained tractography (Smith et al., 2012) implemented in MRtrix3 (Tournier et al., 2019) to calculate whole-brain tractogram with 5 million streamlines and removing the streamlines that do not reach any GM ROI. Similar to the simulated data, we weighted the tractograms with COMMIT (Daducci et al., 2013, 2015) and the robust version to obtain RMSE, intra-axonal, and isotropic signal fraction maps. Reliability estimates for the measurements were based on the 5TT (Smith et al., 2012; Tournier et al., 2019) segmentation of the WM, which provides voxel-wise values between 0 and 1 depending on how likely the content of the voxel is WM. A similar approach has been used in other weighting (Smith et al., 2015a) or filtering (Smith et al., 2013) algorithms to restrict the contribution of voxels contaminated with partial volume toward the model fit.

6.2 Results and discussion

We used the synthetic fiber phantom (Figure 6.1) to evaluate the streamline-specific contributions $\mathbf{x}$ as a function of streamline lengths from 3 to 100 voxels. This setup ensured that all changes in streamline contributions are due to the partial volume effect and not due to the geometrical properties of the streamlines. For the baseline (A), all voxels consisted of WM signal, whereas for the setups (B) and (C), the last voxel was partially corrupted by GM. Although the ground truth streamline contribution should be 0.75 due to 3:1 signal fraction for parallel and isotropic diffusivities used in the WM simulation, the simulated noise results in a slight deviation even for the baseline setup (A), as demonstrated in Figure 6.2. Partial volume is affecting COMMIT in the setup (B) causing a deviation of 4% from the ground truth for the shortest streamline. With the streamline length increasing, COMMIT approaches the baseline setup results. Adjustment for the reliability of the measurements in the setup (C) is clearly beneficial as the mean streamline contribution is nearly identical to the baseline.

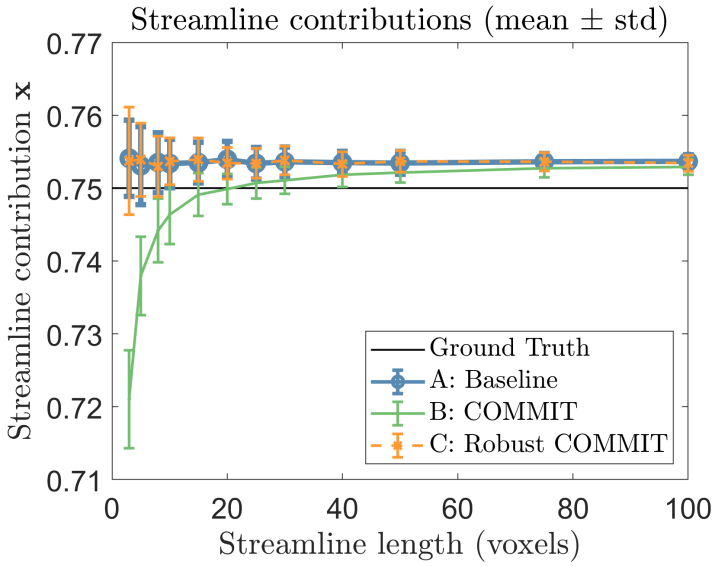

Figure 6.2: **Streamline contributions in the numerical simulations.** The ground-truth value is 0.75. In the baseline setup (A), a single streamline traverses through WM voxels and noise causes a small deviation from the ground truth. When the last voxel is polluted by GM, the contributions of the short streamlines are notably affected by partial volume with standard COMMIT setup (B) whereas with the robust COMMIT setup (C) the results are nearly identical to the baseline setup (A). The reported values are the mean ± standard deviation of the streamline contributions calculated from 300 noise iterations.

We used the HCP subject to compare the whole-brain RMSE, intra-axonal, and isotropic signal fraction maps between COMMIT and the proposed robust version. Figure 6.3 visualizes the histograms of RMSE and RMSE_w computed per each voxel and a coronal section of an image created by subtracting the result of Robust COMMIT from COMMIT. It is important to note that the minimization process is global, i.e. all the voxels and all the streamlines are considered at the same time. These errors are computed once the minimization process finished but per each voxel independently. In this experiment, for each voxel, only one value of reliability is considered for all the measurements, this makes the computation of RMSE_w equivalent to RMSE. In the plot, the error distributions displayed are comparable, and in the map of differences, the regions likely polluted by GM present the biggest RMSE_w because the smaller weights considered from the reliability map allow bigger errors for those voxels in the fitting, which is performed globally.

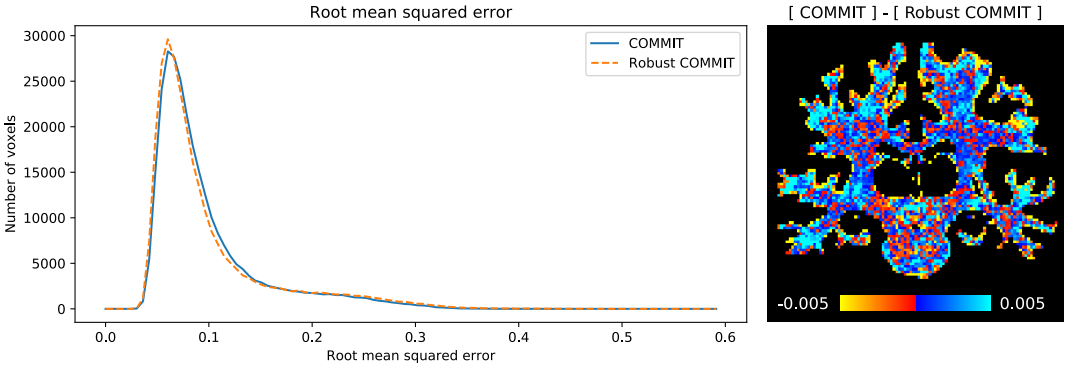

Figure 6.3: **Whole-brain RMSE evaluation of the HCP subject.** Left: Histograms of RMSE generated with COMMIT and RMSE_w generated with Robust COMMIT. Right: Coronal section of an image created by subtracting the result of Robust COMMIT from COMMIT. In this case, as only one reliability value is considered per voxel the computation of RMSE is equivalent to the RMSE_w and the methods produced a comparable distribution of errors. In the coronal image is possible to see in the WM-GM boundary that Robust COMMIT produced bigger errors, but this result can be an artifact of the RMSE computation per voxel.

Figure 6.4 shows the differences of the intra-axonal and isotropic signal fraction compartments. It displays the histogram of values and a coronal section of an image created by subtracting the respective results of Robust COMMIT from COMMIT. The intra-axonal compartments recovered by both methods are comparable, this is expected as the data does not contains many outliers. On the other hand, greater difference can be seen in the isotropic compartment, where Robust COMMIT produced bigger values in most of the

voxels but in the WM-GM boundary, where COMMIT produced bigger values. It is possible to see that the distribution of intra-axonal values produced by Robust COMMIT is a little bit shifted to the left in comparison to the results of COMMIT. On the other hand, the isotropic compartment of Robust COMMIT looks loaded toward the right of COMMIT results. In this compartment, the displacement is bigger than the intra-axonal one. The sum of both compartments has maximum peaks at 1.002 for Robust COMMIT, while for COMMIT at 1.033. This behavior needs to be investigated in future work.

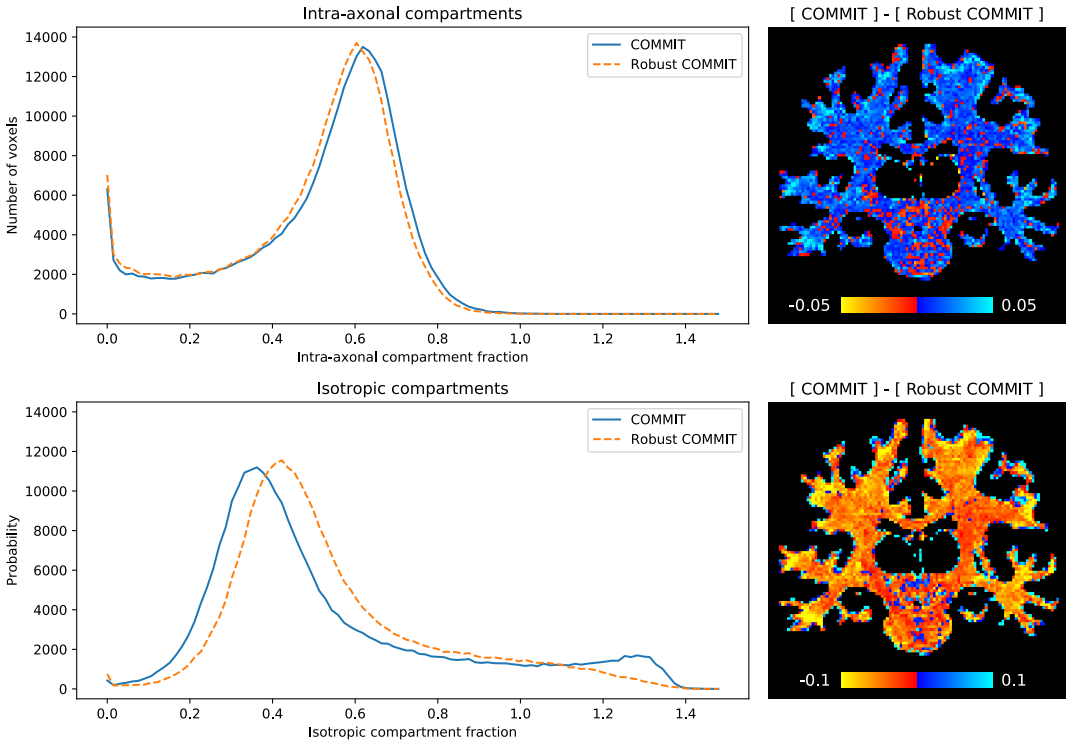

Figure 6.4: **Whole-brain intra-axonal and isotropic signal fraction evaluation of the HCP subject.** Left: Histograms of compartments. Right: Coronal section of an image created by subtracting the result of Robust COMMIT from COMMIT. Top: Intra-axonal compartment fractions. Bottom: Isotropic compartment fraction. The distribution of intra-axonal measurements generated by both methods are comparable, but COMMIT obtains bigger values in voxels where is expected to have mostly WM and on the WM-GM boundary, while in bigger areas that also contain GM, e.g., brainstem, the Robust COMMIT assigned bigger values to the compartment. In the case of the isotropic compartment, the robust COMMIT generates bigger values for most of the voxels, but original COMMIT generated a bigger number of voxels with values > 1.2. This can be due to isolated voxels that contain GM can be described by increasing the contribution of the isotropic compartment, this effect can be seen on the WM-GM boundary. If reliability is used, the isotropic compartment does not need to be too big.

In this work, we proposed a novel robust cost function for COMMIT (Daducci et al., 2013, 2015; Schiavi et al., 2020; Ocampo-Pineda et al., 2021) in Eq. 6.5 that takes into account the reliability of the data in the weighting process, in which the modeling can be affected if the voxels are affected by partial volume, outliers, or artifacts. We demonstrated that it was minimally affected by the partial volume in the synthetic simulation in Figure 6.2. Moreover, we performed a test with HCP data taking into account the partial volume effect. The robust weighting algorithm had competitive results, but we think that in presence of outliers and artifacts the proposed method can outperform the performance of the original formulation. These investigations will be done in future work.

Chapter 7

Conclusion

In this thesis we presented, discussed, and proposed solutions to one of the major problems of tractography, which are the implausible streamlines reconstructed (Maier-Hein et al., 2017) and the invalid connections between cortical and subcortical regions that those create (Zalesky et al., 2016). With this work, we looked to understand if the incorporation of information about the white matter (WM) organization can help to identify and remove invalid representations of WM pathways. We worked with the COMMIT framework that has been effectively used to link tissue microstructure properties to the streamlines and to remove redundant streamlines and the ones that are not compatible with the underlined data along their complete trajectory (Daducci et al., 2013, 2015). The COMMIT framework effectively represents the tractography problem in a linear formulation and sets it as a convex problem that promotes the identification of a unique solution. The formulation allows the integration of new information or regularization terms that can be used to add restrictions to the problem, and also more information. That is what we did, we extended COMMIT to improve the tractography reconstructions weighted and filtered by the framework.

We designed and integrated two regularization terms and we proposed a robust cost function. The regularization terms consider information about the structural organization of the streamlines, specifically, a structural organization of groups of streamlines. The main purpose of those is to promote solutions that reproduce the observed data but using the minimum number of groups of streamlines. The initial strategy presented in Chapter 4, uses a partition of groups of streamlines. These groups were defined based on the regions of the cortex that the streamlines intersect, this strategy is identified as COMMIT2 (Schiavi et al., 2020). The second strategy presented in Chapter 5,

in this one we extended the group division to a multilevel hierarchical structure. In the structure tested, we consider as first-level the same partition used in COMMIT2, and we added as a second level another partition which was defined by splitting the groups in level one into clusters that were created based on the pathway described by the streamlines (Ocampo-Pineda et al., 2021). The proposed formulation is not limited to two levels, it supports the addition of more levels, and also it allows to assign individual weights to each group to promote removing or keeping groups in different ways. We proposed computing the group weights using the contribution of the streamlines to the global signal, but the definition of these values can consider additional information like the length of the streamlines or coming from external sources, such as anatomical atlases. Finally, we proposed a robust cost function to deal with voxels affected by partial volume, or voxels that can be outliers or artifacts. Some advantages and limitations, as well as a summary of the work developed in this thesis, will be discussed in the following paragraphs.

The human brain is a fascinating and complex organ that has been studied for many years, nowadays we understand some aspects but ignore many more. In recent years it has been possible to study it in vivo and in a noninvasive way, with tools like magnetic resonance image and tractography (Basser et al., 1994a, 2000). This has been used to create representations of the white matter structures, that let us study and understand how the brain is connected, its functions, and changes because of the aging process or by a disease. Tractography is also a research area that is in development, with known limitations that are in the process to be solved, with works like microstructure informed tractography (Kreher et al., 2008; Sherbondy et al., 2009; Daducci et al., 2016), from which this thesis is part. All these concepts were presented and discussed in Chapter 2, to give a background about the context and the motivation of this thesis.

We developed this work with the intention to apply it on in vivo data, unfortunately, up to now, there is no ground truth to validate the reconstructions generated (Dyrby et al., 2007; Côté et al., 2013). Because of this lack of evaluation on in vivo data, we proposed to use an automatic segmentation tool (Garyfallidis et al., 2018; Rheault, 2020) and anatomical models of valid and invalid groups of streamlines to evaluate and compare the tractography reconstructions generated with our proposal. The procedure implemented for the creation of the models and the gold standard is described in Chapter 3.

The first strategy proposed to improve the weighting and filtering of tractography reconstructions is presented in Chapter 4, this is identified as COMMIT2. In this strategy, we took into account that the axons are organized and grouped in fascicles (Udin and Fawcett, 1988). We included this organization in the optimization process with a regularization term implementing the adaptive group lasso regularization (Yuan and Lin, 2006; Wang and Leng, 2008), Figure 4.1 presents a diagram of this consideration. The original COMMIT framework filters out redundant and invalid streamlines, and with our extension, it is able to remove groups of invalid streamlines, this was proved on synthetic and in vivo data. In the study performed we created the groups based on the structural connections between cortical and subcortical regions. For the evaluation of synthetic data, we use a phantom that mimics some of the WM configurations. The phantom and the evaluation criteria are described in Figure 4.2. With the results presented in Figure 4.5 we proved that our method obtains better results than the state-of-the-art methods that only consider a data driven approach. On this phantom we also studied the effect of the regularization strength parameter λ, Figure 4.4 presents the number of valid and invalid connections kept after applying our method with different regularization strength values. Many more invalid bundles were removed (372 IB) before the first VB was removed and the percentage of valid connections increases as the regularization parameter increases and more streamlines were removed, but if the regularization strength is too big, the valid bundles are also affected. We were not able to define a close solution for the definition of the regularization strength. We found that it is different for different setups of the problem, i.e., tractography reconstruction, group definition, or weights. For in vivo reconstructions, where there is no ground truth, a quality check that the filtering does not remove the known structures is recommended. In this work, we compared the volume coverage before and after filtering and the contribution of valid and invalid bundles to the global signal. In Figure 4.8 we demonstrated that the volume of the valid bundles was not affected in comparison with the invalid ones, which were almost completely removed and the contribution (streamline weight) of these to the global signal was very small in comparison to the contribution of the valid ones, the difference was at least two orders of magnitude.

In Chapter 5 we presented a strategy to further improve the reconstructions where we tried to remove groups of implausible streamlines inside the bundles. We noted that in the previous approach the groups can contain valid and

invalid bundles, as is illustrated in Figure 5.1. To handle this situation we proposed the method COMMIT2$_{\text{tree}}$. We adapted the regularization term to consider a multilevel hierarchical structure of groups of streamlines, to take into account that the fascicles of axons can be divided into subfascicles (Chenot et al., 2019; Nieuwenhuys et al., 2008). We implemented the hierarchical sparse encoding approach (Jenatton et al., 2011), which supports structures with multiple levels and requires that the groups in one level are split into subgroups, to promote sparse solutions in a tree-structured way (Zhao et al., 2009). A schematic representation of the differences between the methods is presented in Figure 5.2. In this work we designed a hierarchical structure with two levels, the first level contains the groups used in COMMIT2. In the second level, we clustered the streamlines inside each group based on their pathway. With this configuration, COMMIT2$_{\text{tree}}$ is able to reproduce and improve the results of the grouping approach. The method with hierarchical approach assigned smaller contributions to and removed groups of implausible streamlines inside valid bundles, this is presented in Figure 5.7 and Table 5.2. In this proposal, the regularization term has a bigger contribution to the problem to be optimized, because the number of groups considered is bigger than in COMMIT2, in this case, each streamline is present in two groups. Because of this, the filtering is stronger, i.e., it promotes that more streamlines are removed, this situation can be handled by reducing the regularization strength parameter λ, and as for the previous strategy, it is strongly recommended to quality check that the known structures are not removed.

The current weighting approaches are valid only in voxels that the chosen model can represent, which is an issue in voxels that are affected by partial volume or by outliers or artifacts. To fix this, we proposed in Chapter 6 a novel robust cost function to COMMIT framework (Daducci et al., 2013, 2015). We demonstrated that it was minimally affected by partial volume in a synthetic simulation in Figure 6.2. Moreover, we performed a test on HCP data, where we compared the performance of the robust and the original formulation on a healthy subject taking into account the partial volume of WM. The robust weighting had competitive results, but we have the hypothesis that the proposed formulation can outperform the original formulation when the data used contains outliers or artifacts that decrease reliability in the DW-MRI measurement. This is part of the future work, as the evaluation of the robust formulation for the investigation of the human connectome.

As a conclusion of this thesis, we presented evidence about the benefits of introducing information about the WM structure to remove implausible streamlines in tractography, and information about the reliability of the data for the estimation of the streamline contributions. We implemented two strategies that allow us to include knowledge about the anatomy that could come from different sources that add information to the microstructural information already considered in the original COMMIT framework, and we proposed a robust cost function to handle noisy data, considering the reliability of the data. I would like to highlight that the methods proposed should not be used as black-box, the regularization strength parameter, the definition of weights of the groups and the reliability of the data, and the group configuration used affect the quality of the reconstructions produced.

All these aspects are areas that can be improved in the method. More validation is needed, future work is required to design strategies of evaluation with synthetic and in vivo data. For the first one, it is required more complex phantoms that reproduce complex scenarios that are found in the anatomy, like the presence of plausible and implausible streamlines in the same connection of cortical regions. We need to evaluate the benefits for the investigation of the human connectome, especially in clinical cases. The definition of the weights is a very interesting research area with many possibilities to explore. To compute them we have used the contributions estimated with COMMIT, but the length of the streamlines can be considered in the process, moreover, the values of the weights can be computed from different sources, e.g., from the known anatomy or atlases (the likelihood of the existence of a bundle), from other modalities like functional magnetic resonance imaging (the correlation of a property between cortical areas), from other methods that can generate metrics o values over the streamlines, like the quantity of myelin signal fraction or the thickness of the cortex, and the combination of these and other values. I think one important variable to know is the ratio or difference in the weights that are required to promote kipping or removing a bundle, this to avoid the introduction of a strong bias by combining information from heterogeneous sources. About the definition of the group structure, there are also many ways to do it that will be interesting to test, like add more levels, the effect of different groups of different sizes, or different clustering procedures, and also consider and link more than one property to each streamline like, axonal diameter, diffusion signal fraction, or myelin signal fraction.

The proposed microstructure informed tractography framework is a flexible tool able to merge and link information of tractography and more modalities or sources. We think it will help to improve tractography reconstructions and the study and description of the brain.

Bibliography

Alexander, A. L., Lee, J. E., Lazar, M., and Field, A. S. (2007). Diffusion tensor imaging of the brain. *Neurotherapeutics*, 4(3):316–329.

Alexander, D., Barker, G., and Arridge, S. (2002). Detection and modeling of non-Gaussian apparent diffusion coefficient profiles in human brain data. *Magnetic Resonance in Medicine*, 48(2):331–340.

Alexander, D. C. (2005). Multiple-Fiber Reconstruction Algorithms for Diffusion MRI. *Annals of the New York Academy of Sciences*, 1064(1):113–133.

Alexander, D. C. (2008). A general framework for experiment design in diffusion mri and its application in measuring direct tissue-microstructure features. *Magnetic Resonance in Medicine*, 60(2):439–448.

Alexander, D. C., Dyrby, T. B., Nilsson, M., and Zhang, H. (2019). Imaging brain microstructure with diffusion MRI: practicality and applications. *NMR in Biomedicine*, 32(4):e3841. e3841 NBM-16-0261.R1.

Alexander, D. C., Hubbard, P. L., Hall, M. G., Moore, E. A., Ptito, M., Parker, G. J., and Dyrby, T. B. (2010). Orientationally invariant indices of axon diameter and density from diffusion MRI. *NeuroImage*, 52(4):1374 – 1389.

Alexander-Bloch, A., Giedd, J. N., and Bullmore, E. (2013). Imaging structural co-variance between human brain regions. *Nature Reviews Neuroscience*, 14(5):322–336.

Assaf, Y. and Basser, P. J. (2005). Composite hindered and restricted model of diffusion (CHARMED) MR imaging of the human brain. *NeuroImage*, 27(1):48 – 58.

Assaf, Y., Blumenfeld-Katzir, T., Yovel, Y., and Basser, P. J. (2008). Axcaliber: A method for measuring axon diameter distribution from diffusion MRI. *Magnetic Resonance in Medicine*, 59(6):1347–1354.

Assaf, Y., Johansen-Berg, H., and Thiebaut de Schotten, M. (2019). The role of diffusion mri in neuroscience. *NMR in Biomedicine*, 32(4):e3762. e3762 NBM-16-0223.R1.

Basser, P., Mattiello, J., and Lebihan, D. (1994a). Estimation of the effective self-diffusion tensor from the nmr spin echo. *Journal of Magnetic Resonance, Series B*, 103(3):247–254.

Basser, P. J., Mattiello, J., and LeBihan, D. (1994b). MR diffusion tensor spectroscopy and imaging. *Biophysical journal*, 66(1):259–267. S0006-3495(94)80775-1[PII].

Basser, P. J., Pajevic, S., Pierpaoli, C., Duda, J., and Aldroubi, A. (2000). In vivo fiber tractography using DT-MRI data. *Magnetic Resonance in Medicine*, 44(4):625–632.

Basser, P. J. and Pierpaoli, C. (1996). Microstructural and Physiological Features of Tissues Elucidated by Quantitative-Diffusion-Tensor MRI. *Journal of Magnetic Resonance, Series B*, 111(3):209 – 219.

Bassett, D. S. and Bullmore, E. T. (2009). Human brain networks in health and disease. *Current opinion in neurology*, 22(4):340.

Bassett, D. S. and Gazzaniga, M. S. (2011). Understanding complexity in the human brain. *Trends in cognitive sciences*, 15(5):200–209. 21497128[pmid].

Bassett, D. S. and Sporns, O. (2017). Network neuroscience. *Nature neuroscience*, 20(3):353.

Bastiani, M., Shah, N. J., Goebel, R., and Roebroeck, A. (2012). Human cortical connectome reconstruction from diffusion weighted MRI: The effect of tractography algorithm. *NeuroImage*, 62(3):1732 – 1749.

Batchelor, P. G., Calamante, F., Tournier, J.-D., Atkinson, D., Hill, D. L. G., and Connelly, A. (2006). Quantification of the shape of fiber tracts. *Magnetic Resonance in Medicine*, 55(4):894–903.

Beck, A. and Teboulle, M. (2009). A Fast Iterative Shrinkage-Thresholding Algorithm for Linear Inverse Problems. *SIAM Journal on Imaging Sciences*, 2(1):183–202.

Behrens, T., Berg, H. J., Jbabdi, S., Rushworth, M., and Woolrich, M. (2007). Probabilistic diffusion tractography with multiple fibre orientations: What can we gain? *NeuroImage*, 34(1):144 – 155.

Behrens, T., Woolrich, M., Jenkinson, M., Johansen-Berg, H., Nunes, R., Clare, S., Matthews, P., Brady, J., and Smith, S. (2003). Characterization and propagation of uncertainty in diffusion-weighted MR imaging. *Magnetic Resonance in Medicine*, 50(5):1077–1088.

Bells, S., Cercignani, M., Deoni, S., Assaf, Y., Pasternak, O., Evans, C. J., Leemans, A., and Jones, D. K. (2011). Tractometry–comprehensive multi-modal quantitative assessment of white matter along specific tracts. volume 19, page 678.

Berger, A. (2002). Magnetic resonance imaging. *BMJ (Clinical research ed.)*, 324(7328):35–35. 11777806[pmid].

Bitar, R., Leung, G., Perng, R., Tadros, S., Moody, A. R., Sarrazin, J., McGregor, C., Christakis, M., Symons, S., Nelson, A., and Roberts, T. P. (2006). MR Pulse Sequences: What Every Radiologist Wants to Know but Is Afraid to Ask. *RadioGraphics*, 26(2):513–537. PMID: 16549614.

Bloch, F. (1946). Nuclear induction. *Phys. Rev.*, 70:460–474.

Brown, R. (1828). Xxvii. a brief account of microscopical observations made in the months of june, july and august 1827, on the particles contained in the pollen of plants; and on the general existence of active molecules in organic and inorganic bodies. *The Philosophical Magazine*, 4(21):161–173.

Bullmore, E. and Sporns, O. (2009). Complex brain networks: graph theoretical analysis of structural and functional systems. *Nature Reviews Neuroscience*, 10(3):186–198.

Bullmore, E. and Sporns, O. (2012). The economy of brain network organization. *Nature Reviews Neuroscience*, 13(5):336–349.

Bullmore, E. T. and Bassett, D. S. (2011). Brain graphs: graphical models of the human brain connectome. *Annual review of clinical psychology*, 7:113–140.

Burdette, J. H., Durden, D. D., Elster, A. D., and Yen, Y.-F. (2001). High b-value diffusion-weighted mri of normal brain. *Journal of Computer Assisted Tomography*, 25(4).

Caiafa, C. F. and Pestilli, F. (2017). Multidimensional encoding of brain connectomes. *Scientific Reports*.

Caiafa, C. F., Sporns, O., Saykin, A., and Pestilli, F. (2017). Unified representation of tractography and diffusion-weighted MRI data using sparse multidimensional arrays. In Guyon, I., Luxburg, U. V., Bengio, S., Wallach, H., Fergus, R., Vishwanathan, S., and Garnett, R., editors, *Advances in Neural Information Processing Systems 30*, pages 4340–4351. Curran Associates, Inc.

Callaghan, P. (1996). NMR imaging, NMR diffraction and applications of pulsed gradient spin echoes in porous media. *Magnetic Resonance Imaging*, 14(7):701 – 709. Proceedings of the Third International Meeting on Recent Advances in MR Applications to Porous Media.

Callaghan, P. T., Eccles, C. D., and Xia, Y. (1988). NMR microscopy of dynamic displacements: k-space and q-space imaging. *Journal of Physics E: Scientific Instruments*, 21(8):820–822.

Cammoun, L., Gigandet, X., Meskaldji, D., Thiran, J. P., Sporns, O., Do, K. Q., Maeder, P., Meuli, R., and Hagmann, P. (2012). Mapping the human connectome

at multiple scales with diffusion spectrum MRI. *Journal of Neuroscience Methods*, 203(2):386 – 397.

Caruyer, E., Daducci, A., Descoteaux, M., Houde, J.-C., Thiran, J.-P., and Verma, R. (2014). Phantomas: a flexible software library to simulate diffusion MR phantoms. In *ISMRM, May 2014, Milan, Italy. 2014*.

Catani, M. and Dell'Acqua, F. (2011). *Mapping white matter pathways with diffusion imaging tractography: focus on neurosurgical applications*, pages 61–75. Springer Vienna, Vienna.

Catani, M., Howard, R. J., Pajevic, S., and Jones, D. K. (2002). Virtual in Vivo Interactive Dissection of White Matter Fasciculi in the Human Brain. *NeuroImage*, 17(1):77 – 94.

Cercignani, M. and Bouyagoub, S. (2018). Brain microstructure by multi-modal mri: Is the whole greater than the sum of its parts? *NeuroImage*, 182:117–127. Microstructural Imaging.

Chenot, Q., Tzourio-Mazoyer, N., Rheault, F., Descoteaux, M., Crivello, F., Zago, L., Mellet, E., Jobard, G., Joliot, M., Mazoyer, B., and Petit, L. (2019). A population-based atlas of the human pyramidal tract in 410 healthy participants. *Brain Structure and Function*, 224(2):599–612.

Christiaens, D., Reisert, M., Dhollander, T., Sunaert, S., Suetens, P., and Maes, F. (2015). Global tractography of multi-shell diffusion-weighted imaging data using a multi-tissue model. *NeuroImage*, 123:89 – 101.

Colom, R., Karama, S., Jung, R. E., and Haier, R. J. (2010). Human intelligence and brain networks. *Dialogues in clinical neuroscience*, 12(4):489–501. 21319494[pmid].

Conturo, T. E., Lori, N. F., Cull, T. S., Akbudak, E., Snyder, A. Z., Shimony, J. S., McKinstry, R. C., Burton, H., and Raichle, M. E. (1999). Tracking neuronal fiber pathways in the living human brain. *Proceedings of the National Academy of Sciences*, 96(18):10422–10427.

Coronado-Leija, R., Ramirez-Manzanares, A., and Marroquin, J. L. (2017). Estimation of individual axon bundle properties by a multi-resolution discrete-search method. *Medical Image Analysis*, 42:26–43.

Cory, D. G. (1990). Measurement of translational displacement probabilities by NMR: An indicator of compartmentation. *Magnetic Resonance in Medicine*, 14(3):435–444.

Côté, M.-A., Garyfallidis, E., Larochelle, H., and Descoteaux, M. (2015). Cleaning up the mess: tractography outlier removal using hierarchical QuickBundles clustering. In *ISMRM 2015*.

Côté, M.-A., Girard, G., Boré, A., Garyfallidis, E., Houde, J.-C., and Descoteaux, M. (2013). Tractometer: Towards validation of tractography pipelines. *Medical Image Analysis*, 17(7):844 – 857. Special Issue on the 2012 Conference on Medical Image Computing and Computer Assisted Intervention.

Cousineau, M., Jodoin, P.-M., Garyfallidis, E., Côté, M.-A., Morency, F. C., Rozanski, V., Grand'Maison, M., Bedell, B. J., and Descoteaux, M. (2017). A test-retest study on Parkinson's PPMI dataset yields statistically significant white matter fascicles. *NeuroImage: Clinical*, 16:222 – 233.

Daducci, A., Dal Palù, A., Descoteaux, M., and Thiran, J.-P. (2016). Microstructure Informed Tractography: Pitfalls and Open Challenges. *Frontiers in Neuroscience*, 10:247.

Daducci, A., Dal Palù, A., Lemkaddem, A., and Thiran, J.-P. (2013). A convex optimization framework for global tractography. In *2013 IEEE 10th International Symposium on Biomedical Imaging*, pages 524–527.

Daducci, A., Dal Palù, A., Lemkaddem, A., and Thiran, J.-P. (2015). COMMIT: Convex Optimization Modeling for Microstructure Informed Tractography. *IEEE Transactions on Medical Imaging*, 34(1):246–257.

Daducci, A., Gerhard, S., Griffa, A., Lemkaddem, A., Cammoun, L., Gigandet, X., Meuli, R., Hagmann, P., and Thiran, J.-P. (2012). The Connectome Mapper: An Open-Source Processing Pipeline to Map Connectomes with MRI. *PLOS ONE*, 7(12):1–9.

Dayan, M., Monohan, E., Pandya, S., Kuceyeski, A., Nguyen, T. D., Raj, A., and Gauthier, S. A. (2016). Profilometry: A new statistical framework for the characterization of white matter pathways, with application to multiple sclerosis. *Human Brain Mapping*, 37(3):989–1004.

Delettre, C., Messé, A., Dell, L.-A., Foubet, O., Heuer, K., Larrat, B., Meriaux, S., Mangin, J.-F., Reillo, I., de Juan Romero, C., Borrell, V., Toro, R., and Hilgetag, C. C. (2019). Comparison between diffusion MRI tractography and histological tract-tracing of cortico-cortical structural connectivity in the ferret brain. *Network neuroscience (Cambridge, Mass.)*, 3(4):1038–1050.

Dell'Acqua, F. and Tournier, J.-D. (2019). Modelling white matter with spherical deconvolution: How and why? *NMR in Biomedicine*, 32(4):e3945. e3945 NBM-17-0226.R1.

Dempster, A. P., Laird, N. M., and Rubin, D. B. (1977). Maximum likelihood from incomplete data via the em algorithm. *Journal of the Royal Statistical Society. Series B (Methodological)*, 39(1):1–38.

Descoteaux, M. (2008). *High Angular Resolution Diffusion MRI: from Local Estimation to Segmentation and Tractography*. PhD dissertation, Human-Computer Interaction [cs.HC]. Université Nice Sophia Antipolis.

Descoteaux, M. (2015). *High Angular Resolution Diffusion Imaging (HARDI)*, pages 1–25. American Cancer Society.

Descoteaux, M., Deriche, R., Knosche, T. R., and Anwander, A. (2009). Deterministic and Probabilistic Tractography Based on Complex Fibre Orientation Distributions. *IEEE Transactions on Medical Imaging*, 28(2):269–286.

Desikan, R. S., Ségonne, F., Fischl, B., Quinn, B. T., Dickerson, B. C., Blacker, D., Buckner, R. L., Dale, A. M., Maguire, R. P., Hyman, B. T., Albert, M. S., and Killiany, R. J. (2006). An automated labeling system for subdividing the human cerebral cortex on MRI scans into gyral based regions of interest. *NeuroImage*, 31(3):968 – 980.

Destrieux, C., Fischl, B., Dale, A., and Halgren, E. (2010). Automatic parcellation of human cortical gyri and sulci using standard anatomical nomenclature. *NeuroImage*, 53(1):1 – 15.

Drakesmith, M., Caeyenberghs, K., Dutt, A., Lewis, G., David, A., and Jones, D. (2015). Overcoming the effects of false positives and threshold bias in graph theoretical analyses of neuroimaging data. *NeuroImage*, 118:313 – 333.

Dyrby, T. B., Søgaard, L. V., Parker, G. J., Alexander, D. C., Lind, N. M., Baaré, W. F., Hay-Schmidt, A., Eriksen, N., Pakkenberg, B., Paulson, O. B., and Jelsing, J. (2007). Validation of in vitro probabilistic tractography. *NeuroImage*, 37(4):1267–1277.

Edelstein, W. A., Glover, G. H., Hardy, C. J., and Redington, R. W. (1986). The intrinsic signal-to-noise ratio in nmr imaging. *Magnetic Resonance in Medicine*, 3(4):604–618.

Einstein, A. (1905). Investigations on the Theory of the Brownian Movement. *Courier Corporation*.

Essayed, W. I., Zhang, F., Unadkat, P., Cosgrove, G. R., Golby, A. J., and O'Donnell, L. J. (2017). White matter tractography for neurosurgical planning: A topography-based review of the current state of the art. *NeuroImage: Clinical*, 15:659–672.

Essen, D. C. V., Smith, S. M., Barch, D. M., Behrens, T. E., Yacoub, E., and Ugurbil, K. (2013). The WU-Minn Human Connectome Project: An overview. *NeuroImage*, 80:62–79.

Fan, L. (2021). Mapping the human brain: What is the next frontier? *The Innovation*, 2(1).

Fick, A. (1855). V. on liquid diffusion. *The London, Edinburgh, and Dublin Philosophical Magazine and Journal of Science*, 10(63):30–39.

Fick, R. H. J., Wassermann, D., and Deriche, R. (2019). The dmipy toolbox: Diffusion mri multi-compartment modeling and microstructure recovery made easy. *Frontiers in Neuroinformatics*, 13:64.

Fields, R. D. (2010). Neuroscience. change in the brain's white matter. *Science (New York, N.Y.)*, 330(6005):768–769. 21051624[pmid].

Fillard, P., Poupon, C., and Mangin, J.-F. (2009). A Novel Global Tractography Algorithm Based on an Adaptive Spin Glass Model. In Yang, G.-Z., Hawkes, D., Rueckert, D., Noble, A., and Taylor, C., editors, *Medical Image Computing and Computer-Assisted Intervention – MICCAI 2009*, pages 927–934, Berlin, Heidelberg. Springer Berlin Heidelberg.

Formica, D. and Silvestri, S. (2004). Biological effects of exposure to magnetic resonance imaging: an overview. *BioMedical Engineering OnLine*, 3(1):11.

Frank, L. R. (2001). Anisotropy in high angular resolution diffusion-weighted mri. *Magnetic Resonance in Medicine*, 45(6):935–939.

Frank, L. R. (2002). Characterization of anisotropy in high angular resolution diffusion-weighted MRI. *Magnetic Resonance in Medicine*, 47(6):1083–1099.

Garyfallidis, E., Brett, M., Correia, M. M., Williams, G. B., and Nimmo-Smith, I. (2012). QuickBundles, a Method for Tractography Simplification. *Frontiers in Neuroscience*.

Garyfallidis, E., Côté, M.-A., Rheault, F., and Descoteaux, M. (2016). Quickbundlesx: Sequential clustering of millions of streamlines in multiple levels of detail at record execution time.

Garyfallidis, E., Côté, M.-A., Rheault, F., Sidhu, J., Hau, J., Petit, L., Fortin, D., Cunanne, S., and Descoteaux, M. (2018). Recognition of white matter bundles using local and global streamline-based registration and clustering. *NeuroImage*, 170:283 – 295. Segmenting the Brain.

Garyfallidis, E., Ocegueda, O., Wassermann, D., and Descoteaux, M. (2015). Robust and efficient linear registration of white-matter fascicles in the space of streamlines. *NeuroImage*, 117:124 – 140.

Geyer, C. and Moller, J. (1994). Simulation procedures and likelihood inference for spatial point processes. *Scandinavian Journal of Statistics*, 21:359–373.

Giannelli, M., Cosottini, M., Michelassi, M. C., Lazzarotti, G., Belmonte, G., Bartolozzi, C., and Lazzeri, M. (2010). Dependence of brain DTI maps of fractional anisotropy and mean diffusivity on the number of diffusion weighting directions. *Journal of Applied Clinical Medical Physics*, 11(1):176–190.

Girard, G., Caminiti, R., Battaglia-Mayer, A., St-Onge, E., Ambrosen, K. S., Eskildsen, S. F., Krug, K., Dyrby, T. B., Descoteaux, M., Thiran, J.-P., and

Innocenti, G. M. (2020). On the cortical connectivity in the macaque brain: A comparison of diffusion tractography and histological tracing data. *NeuroImage*, 221:117201.

Girard, G., Fick, R., Descoteaux, M., Deriche, R., and Wassermann, D. (2015). AxTract: Microstructure-Driven Tractography Based on the Ensemble Average Propagator. In Ourselin, S., Alexander, D. C., Westin, C.-F., and Cardoso, M. J., editors, *Information Processing in Medical Imaging*, pages 675–686, Cham. Springer International Publishing.

Glasser, M. F., Smith, S. M., Marcus, D. S., Andersson, J. L. R., Auerbach, E. J., Behrens, T. E. J., Coalson, T. S., Harms, M. P., Jenkinson, M., Moeller, S., Robinson, E. C., Sotiropoulos, S. N., Xu, J., Yacoub, E., Ugurbil, K., and Van Essen, D. C. (2016). The Human Connectome Project's neuroimaging approach. *Nature neuroscience*, 19(9):1175–1187. nn.4361[PII].

Glasser, M. F., Sotiropoulos, S. N., Wilson, J. A., Coalson, T. S., Fischl, B., Andersson, J. L., Xu, J., Jbabdi, S., Webster, M., Polimeni, J. R., Essen, D. C. V., and Jenkinson, M. (2013). The minimal preprocessing pipelines for the Human Connectome Project. *NeuroImage*, 80:105 – 124. Mapping the Connectome.

Gong, G., He, Y., Concha, L., Lebel, C., Gross, D. W., Evans, A. C., and Beaulieu, C. (2009). Mapping anatomical connectivity patterns of human cerebral cortex using in vivo diffusion tensor imaging tractography. *Cerebral cortex (New York, N.Y. : 1991)*, 19(3):524–536. bhn102[PII].

Gray, H. and Lewis, W. H. (1918). *Anatomy of the human body*. Philadelphia : Lea and Febiger.

Grebenkov, D. S. (2007). Nmr survey of reflected brownian motion. *Rev. Mod. Phys.*, 79:1077–1137.

Griffa, A., Baumann, P. S., Thiran, J.-P., and Hagmann, P. (2013). Structural connectomics in brain diseases. *NeuroImage*, 80:515 – 526. Mapping the Connectome.

Grover, V. P. B., Tognarelli, J. M., Crossey, M. M. E., Cox, I. J., Taylor-Robinson, S. D., and McPhail, M. J. W. (2015). Magnetic resonance imaging: Principles and techniques: Lessons for clinicians. *Journal of clinical and experimental hepatology*, 5(3):246–255. 26628842[pmid].

Guevara, P., Duclap, D., Poupon, C., Marrakchi-Kacem, L., Fillard, P., Bihan, D. L., Leboyer, M., Houenou, J., and Mangin, J.-F. (2012). Automatic fiber bundle segmentation in massive tractography datasets using a multi-subject bundle atlas. *NeuroImage*, 61(4):1083 – 1099.

Guevara, P., Poupon, C., Rivière, D., Cointepas, Y., Descoteaux, M., Thirion, B., and Mangin, J.-F. (2011). Robust clustering of massive tractography datasets. *NeuroImage*, 54(3):1975 – 1993.

Hagmann, P. (2005). *From diffusion MRI to brain connectomics*. PhD dissertation, L'Ecole Polytechnique Fédérale de Lausanne.

Hagmann, P., Jonasson, L., Maeder, P., Thiran, J.-P., Wedeen, V. J., and Meuli, R. (2006). Understanding Diffusion MR Imaging Techniques: From Scalar Diffusion-weighted Imaging to Diffusion Tensor Imaging and Beyond. *RadioGraphics*, 26(suppl_1):S205–S223. PMID: 17050517.

Hagmann, P., Kurant, M., Gigandet, X., Thiran, P., Wedeen, V. J., Meuli, R., and Thiran, J.-P. (2007). Mapping Human Whole-Brain Structural Networks with Diffusion MRI. *PLOS ONE*, 2(7):1–9.

Hahn, E. L. (1950). Spin echoes. *Phys. Rev.*, 80:580–594.

Hastings, W. K. (1970). Monte carlo sampling methods using markov chains and their applications. *Biometrika*, 57(1):97–109. Full publication date: Apr., 1970.

Hofman, M. A. (2014). Evolution of the human brain: when bigger is better. *Frontiers in neuroanatomy*, 8:15–15. 24723857[pmid].

Hoult, D. I. and Bhakar, B. (1997). Nmr signal reception: Virtual photons and coherent spontaneous emission. *Concepts in Magnetic Resonance*, 9(5):277–297.

Huang, S. Y., Nummenmaa, A., Witzel, T., Duval, T., Cohen-Adad, J., Wald, L. L., and McNab, J. A. (2015). The impact of gradient strength on in vivo diffusion mri estimates of axon diameter. *NeuroImage*, 106:464–472.

Iglesias, J. E., Leemput, K. V., Bhatt, P., Casillas, C., Dutt, S., Schuff, N., Truran-Sacrey, D., Boxer, A., and Fischl, B. (2015). Bayesian segmentation of brainstem structures in MRI. *NeuroImage*, 113:184 – 195.

Ingalhalikar, M., Smith, A., Parker, D., Satterthwaite, T. D., Elliott, M. A., Ruparel, K., Hakonarson, H., Gur, R. E., Gur, R. C., and Verma, R. (2014). Sex differences in the structural connectome of the human brain. *Proceedings of the National Academy of Sciences*, 111(2):823–828.

Jelescu, I. O. and Budde, M. D. (2017). Design and Validation of Diffusion MRI Models of White Matter. *Frontiers in Physics*, 5:61.

Jelescu, I. O., Zurek, M., Winters, K. V., Veraart, J., Rajaratnam, A., Kim, N. S., Babb, J. S., Shepherd, T. M., Novikov, D. S., Kim, S. G., and Fieremans, E. (2016). In vivo quantification of demyelination and recovery using compartment-specific diffusion mri metrics validated by electron microscopy. *NeuroImage*, 132:104–114.

Jenatton, R., Mairal, J., Obozinski, G., and Bach, F. (2011). Proximal Methods for Hierarchical Sparse Coding. *Journal of Machine Learning Research*, 12:2297–2334.

Jeurissen, B., Descoteaux, M., Mori, S., and Leemans, A. (2017). Diffusion MRI fiber tractography of the brain. *NMR in Biomedicine*. e3785 NBM-17-0045.R2.

Jeurissen, B., Leemans, A., Tournier, J.-D., Jones, D. K., and Sijbers, J. (2013). Investigating the prevalence of complex fiber configurations in white matter tissue with diffusion magnetic resonance imaging. *Human Brain Mapping*, 34(11):2747–2766.

Jeurissen, B., Tournier, J.-D., Dhollander, T., Connelly, A., and Sijbers, J. (2014). Multi-tissue constrained spherical deconvolution for improved analysis of multi-shell diffusion MRI data. *NeuroImage*, 103:411 – 426.

Jones, D. K. (2010). *Diffusion MRI. Theory, Methods, and Applications*. Oxford University Press.

Jones, D. K., Knösche, T. R., and Turner, R. (2013). White matter integrity, fiber count, and other fallacies: The do's and don'ts of diffusion MRI. *NeuroImage*, 73:239 – 254.

Jones, D. K., Simmons, A., Williams, S. C., and Horsfield, M. A. (1999). Non-invasive assessment of axonal fiber connectivity in the human brain via diffusion tensor mri. *Magnetic Resonance in Medicine*, 42(1):37–41.

Kaden, E., Anwander, A., and Knösche, T. R. (2008). Variational inference of the fiber orientation density using diffusion mr imaging. *NeuroImage*, 42(4):1366–1380.

Kaden, E., Kelm, N. D., Carson, R. P., Does, M. D., and Alexander, D. C. (2016a). Multi-compartment microscopic diffusion imaging. *NeuroImage*, 139:346–59.

Kaden, E., Kruggel, F., and Alexander, D. C. (2016b). Quantitative mapping of the per-axon diffusion coefficients in brain white matter. *Magnetic Resonance in Medicine*, 75(4):1752–1763.

Kim, D., Sra, S., and Dhillon, I. (2013). A non-monotonic method for large-scale non-negative least squares. *Optimization Methods and Software*, 28:1012 – 1039.

Kingsley, P. B. and Monahan, W. G. (2004). Selection of the optimum b factor for diffusion-weighted magnetic resonance imaging assessment of ischemic stroke. *Magnetic Resonance in Medicine*, 51(5):996–1001.

Konopleva, L., Il'yasov, K. A., Skibbe, H., Kiselev, V. G., Kellner, E., Dhital, B., and Reisert, M. (2018). Modelfree global tractography. *NeuroImage*, 174:576 – 586.

Kreher, B., Mader, I., and Kiselev, V. (2008). Gibbs tracking: A novel approach for the reconstruction of neuronal pathways. *Magnetic Resonance in Medicine*, 60(4):953–963.

Lam, V. (2016). "We know very little about the brain": Experts outline challenges in neuroscience. [Online]. Available from: `https://scopeblog.stanford.edu/2016/11/08/challenges-in-neuroscience-in-the-21st-century/`. Stanford Medicine; accessed 05/02/2021.

Larmor, J. (1897). Lxiii. on the theory of the magnetic influence on spectra; and on the radiation from moving ions. *Philosophical Magazine Series 1*, 44:503–512.

Lauterbur, P. C. (1973). Image formation by induced local interactions: Examples employing nuclear magnetic resonance. *Nature*, 242(5394):190–191.

Le Bihan, D., Breton, E., Lallemand, D., Grenier, P., Cabanis, E., and Laval-Jeantet, M. (1986). MR imaging of intravoxel incoherent motions: application to diffusion and perfusion in neurologic disorders. *Radiology*, 161(2):401–407. PMID: 3763909.

Le Bihan, D. and Iima, M. (2015). Diffusion magnetic resonance imaging: What water tells us about biological tissues. *PLoS biology*, 13(7):e1002203–e1002203. 26204162[pmid].

Le Bihan, D., Turner, R., and Douek, P. (1993). Is water diffusion restricted in human brain white matter? an echo-planar nmr imaging study. *NeuroReport*, 4(7).

Lemkaddem, A., Skiöldebrand, D., Dal Palù, A., Thiran, J.-P., and Daducci, A. (2014). Global Tractography with Embedded Anatomical Priors for Quantitative Connectivity Analysis. *Frontiers in Neurology*, 5:232.

Lieshout, M. N. M. V. (1994). Stochastic annealing for nearest-neighbour point processes with application to object recognition. *Advances in Applied Probability*, 26(2):281–300.

Lipton, M. L. (2008). *Totally Accessible MRI*. Springer, New York, NY.

Lovinger, D. M. (2008). Communication networks in the brain: neurons, receptors, neurotransmitters, and alcohol. *Alcohol research & health : the journal of the National Institute on Alcohol Abuse and Alcoholism*, 31(3):196–214. 23584863[pmid].

Maier-Hein, K. H., Neher, P. F., Houde, J.-C., Côté, M.-A., Garyfallidis, E., Zhong, J., Chamberland, M., Yeh, F.-C., Lin, Y.-C., Ji, Q., Reddick, W. E., Glass, J. O., Chen, D. Q., Feng, Y., Gao, C., Wu, Y., Ma, J., Renjie, H., Li, Q., Westin, C.-F., Deslauriers-Gauthier, S., González, J. O. O., Paquette, M., St-Jean, S., Girard, G., Rheault, F., Sidhu, J., Tax, C. M. W., Guo, F., Mesri, H. Y., Dávid, S., Froeling, M., Heemskerk, A. M., Leemans, A., Boré, A., Pinsard, B., Bedetti, C., Desrosiers, M., Brambati, S., Doyon, J., Sarica, A., Vasta, R., Cerasa, A., Quattrone, A., Yeatman, J., Khan, A. R., Hodges, W., Alexander, S., Romascano, D., Barakovic, M., Auría, A., Esteban, O., Lemkaddem, A., Thiran, J.-P., Cetingul, H. E., Odry, B. L., Mailhe, B., Nadar, M. S., Pizzagalli, F., Prasad, G., Villalon-Reina, J. E., Galvis, J., Thompson, P. M., Requejo, F. D. S., Laguna, P. L., Lacerda, L. M., Barrett, R., Dell'Acqua, F., Catani, M., Petit, L., Caruyer, E., Daducci, A., Dyrby, T. B., Holland-Letz, T., Hilgetag, C. C., Stieltjes, B., and Descoteaux, M. (2017). The challenge of mapping the human connectome based on diffusion tractography. *Nature communications*, 8(1):1349.

Mandonnet, E., Sarubbo, S., and Petit, L. (2018). The Nomenclature of Human White Matter Association Pathways: Proposal for a Systematic Taxonomic Anatomical Classification. *Frontiers in Neuroanatomy*, 12:94.

Mangin, J.-F., Fillard, P., Cointepas, Y., Le Bihan, D., Frouin, V., and Poupon, C. (2013). Toward global tractography. *NeuroImage*, 80:290 – 296. Mapping the Connectome.

Mansfield, P. (1977). Multi-planar image formation using nmr spin echoes. *Journal of Physics C: Solid State Physics*, 10.

Martino, J. and Brogna, C. (2011). *Anatomy of the white-matter pathways*, pages 27–41. Springer Vienna, Vienna.

Mercadante, A. A. and Tadi., P. (2020). Neuroanatomy, Gray Matter. [Online]. Available from: `https://www.ncbi.nlm.nih.gov/books/NBK553239/`. In: StatPearls [Internet]; accessed 19/02/2021.

Metropolis, N., Rosenbluth, A. W., Rosenbluth, M. N., Teller, A. H., and Teller, E. (1953). Equation of state calculations by fast computing machines. *The Journal of Chemical Physics*, 21(6):1087–1092.

Mikulis, D. J. and Roberts, T. P. (2007). Neuro MR: Protocols. *Journal of Magnetic Resonance Imaging*, 26(4):838–847.

Minati, L. and Węglarz, W. P. (2007). Physical foundations, models, and methods of diffusion magnetic resonance imaging of the brain: A review. *Concepts in Magnetic Resonance Part A*, 30A(5):278–307.

Mori, S., Crain, B. J., Chacko, V. P., and Van Zijl, P. C. M. (1999). Three-dimensional tracking of axonal projections in the brain by magnetic resonance imaging. *Annals of Neurology*, 45(2):265–269.

Mori, S. and Tournier, J.-D., editors (2014). *Chapter 8 - Moving Beyond DTI: High Angular Resolution Diffusion Imaging (HARDI)*, pages 65–78. Academic Press, San Diego, second edition.

Nieuwenhuys, R., Voogd, J., and van Huijzen, C. (2008). *The Human Central Nervous System*. Springer, Berlin, Heidelberg.

Novikov, D. S., Fieremans, E., Jespersen, S. N., and Kiselev, V. G. (2019). Quantifying brain microstructure with diffusion MRI: Theory and parameter estimation. *NMR in Biomedicine*, 32(4):e3998.

Ocampo-Pineda, M. (2021). Atlas of false-positive bundles for RecobundlesX. https://doi.org/10.5281/zenodo.4563914. [Online; accessed 9-October-2021].

Ocampo-Pineda, M., Schiavi, S., Rheault, F., Girard, G., Petit, L., Descoteaux, M., and Daducci, A. (2021). Hierarchical microstructure informed tractography. *Brain Connectivity*.

O'Donnell, L. J., Golby, A. J., and Westin, C.-F. (2013). Fiber clustering versus the parcellation-based connectome. *NeuroImage*, 80:283 – 289. Mapping the Connectome.

O'Donnell, L. J. and Westin, C.-F. (2011). An introduction to diffusion tensor image analysis. *Neurosurgery clinics of North America*, 22(2):185–viii. 21435570[pmid].

Panagiotaki, E., Schneider, T., Siow, B., Hall, M. G., Lythgoe, M. F., and Alexander, D. C. (2012). Compartment models of the diffusion MR signal in brain white matter: A taxonomy and comparison. *NeuroImage*, 59(3):2241 – 2254.

Parker, G. J. M. and Alexander, D. C. (2003). Probabilistic Monte Carlo Based Mapping of Cerebral Connections Utilising Whole-Brain Crossing Fibre Information. In Taylor C., N. J., editor, *Information Processing in Medical Imaging*, volume 2732. Springer, Berlin, Heidelberg.

Pestilli, F., Yeatman, J. D., Rokem, A., Kay, K. N., and Wandell, B. A. (2014). Evaluation and statistical inference for human connectomes. *Nature Methods*, 11:1058–1063.

Pierpaoli, C., Jezzard, P., Basser, P. J., Barnett, A., and Di Chiro, G. (1996). Diffusion tensor MR imaging of the human brain. *Radiology*, 201(3):637–648. PMID: 8939209.

Poupon, C., Clark, C., Frouin, V., Régis, J., Bloch, I., Le Bihan, D., and Mangin, J.-F. (2000). Regularization of diffusion-based direction maps for the tracking of brain white matter fascicles. *NeuroImage*, 12(2):184–195.

Price, W. S. (1997). Pulsed-field gradient nuclear magnetic resonance as a tool for studying translational diffusion: Part 1. basic theory. *Concepts in Magnetic Resonance*, 9(5):299–336.

Purcell, E. M., Torrey, H. C., and Pound, R. V. (1946). Resonance absorption by nuclear magnetic moments in a solid. *Phys. Rev.*, 69:37–38.

Rabi, I. I., Zacharias, J. R., Millman, S., and Kusch, P. (1938). A new method of measuring nuclear magnetic moment. *Phys. Rev.*, 53:318–318.

Ramirez-Manzanares, A., Rivera, M., Vemuri, B. C., Carney, P., and Mareci, T. (2007). Diffusion Basis Functions Decomposition for Estimating White Matter Intravoxel Fiber Geometry. *IEEE Transactions on Medical Imaging*, 26(8):1091–1102.

Reisert, M., Kiselev, V. G., Dihtal, B., Kellner, E., and Novikov, D. S. (2014). MesoFT: Unifying Diffusion Modelling and Fiber Tracking. In Golland, P., Hata, N., Barillot, C., Hornegger, J., and Howe, R., editors, *Medical Image Computing and Computer-Assisted Intervention – MICCAI 2014*, pages 201–208, Cham. Springer International Publishing.

Reisert, M., Mader, I., Anastasopoulos, C., Weigel, M., Schnell, S., and Kiselev, V. (2011). Global fiber reconstruction becomes practical. *NeuroImage*, 54(2):955 – 962.

Rheault, F. (2020). *Analyse et reconstruction de faisceaux de la matière blanche*. PhD thesis.

Rheault, F. (2021). Population average atlas for RecobundlesX. https://doi.org/10.5281/zenodo.5165374. [Online; accessed 9-October-2021].

Rheault, F., De Benedictis, A., Daducci, A., Maffei, C., Tax, C. M. W., Romascano, D., Caverzasi, E., Morency, F. C., Corrivetti, F., Pestilli, F., Girard, G., Theaud, G., Zemmoura, I., Hau, J., Glavin, K., Jordan, K. M., Pomiecko, K., Chamberland, M., Barakovic, M., Goyette, N., Poulin, P., Chenot, Q., Panesar, S. S., Sarubbo, S., Petit, L., and Descoteaux, M. (2020a). Tractostorm: The what, why, and how of tractography dissection reproducibility. *Human Brain Mapping*, 41(7):1859–1874.

Rheault, F., Poulin, P., Caron, A. V., St-Onge, E., and Descoteaux, M. (2020b). Common misconceptions, hidden biases and modern challenges of dMRI tractography. *Journal of Neural Engineering*, 17(1):011001.

Roberts, J. D. (1959). *Nuclear Magnetic Resonance: Applications to Organic Chemistry*. McGraw-Hill Series in Advanced Chemistry.

Rockland, K. S. (2002). Axon. In Ramachandran, V., editor, *Encyclopedia of the Human Brain*, pages 349–365. Academic Press, New York.

Sairanen, V., Leemans, A., and Tax, C. (2018). Fast and accurate Slicewise OutLIer Detection (SOLID) with informed model estimation for diffusion MRI data. *NeuroImage*, 181:331–346.

Sammet, S. (2016). Magnetic resonance safety. *Abdominal radiology (New York)*, 41(3):444–451. 26940331[pmid].

Sarwar, T., Ramamohanarao, K., and Zalesky, A. (2019). Mapping connectomes with diffusion MRI: deterministic or probabilistic tractography? *Magnetic Resonance in Medicine*, 81(2):1368–1384.

Savadjiev, P., Campbell, J. S., Descoteaux, M., Deriche, R., Pike, G. B., and Siddiqi, K. (2008). Labeling of ambiguous subvoxel fibre bundle configurations in high angular resolution diffusion MRI. *NeuroImage*, 41(1):58 – 68.

Schiavi, S., Ocampo-Pineda, M., Barakovic, M., Petit, L., Descoteaux, M., Thiran, J.-P., and Daducci, A. (2020). A new method for accurate in vivo mapping of human brain connections using microstructural and anatomical information. *Science Advances*, 6(31).

Schilling, K. G., Nath, V., Hansen, C., Parvathaneni, P., Blaber, J., Gao, Y., Neher, P., Aydogan, D. B., Shi, Y., Ocampo-Pineda, M., Schiavi, S., Daducci, A., Girard,

G., Barakovic, M., Rafael-Patino, J., Romascano, D., Rensonnet, G., Pizzolato, M., Bates, A., Fischi, E., Thiran, J. P., Canales-Rodríguez, E. J., Huang, C., Zhu, H., Zhong, L., Cabeen, R., Toga, A. W., Rheault, F., Theaud, G., Houde, J. C., Sidhu, J., Chamberland, M., Westin, C. F., Dyrby, T. B., Verma, R., Rathi, Y., Irfanoglu, M. O., Thomas, C., Pierpaoli, C., Descoteaux, M., Anderson, A. W., and Landman, B. A. (2019). Limits to anatomical accuracy of diffusion tractography using modern approaches. *NeuroImage*, 185:1 – 11.

Sherbondy, A. J., Dougherty, R. F., Ananthanarayanan, R., Modha, D. S., and Wandell, B. A. (2009). Think Global, Act Local; Projectome Estimation with BlueMatter. In *International Conference on Medical Image Computing and Computer-Assisted Intervention. MICCAI 2009;12(Pt 1):861-868.*

Siless, V., Chang, K., Fischl, B., and Yendiki, A. (2018). AnatomiCuts: Hierarchical clustering of tractography streamlines based on anatomical similarity. *NeuroImage*, 166:32 – 45.

Smith, K., Bastin, M. E., Cox, S. R., Valdés Hernández, M. C., Wiseman, S., Escudero, J., and Sudlow, C. (2019). Hierarchical complexity of the adult human structural connectome. *NeuroImage*, 191:205 – 215.

Smith, R. E., Tournier, J.-D., Calamante, F., and Connelly, A. (2012). Anatomically-constrained tractography: Improved diffusion MRI streamlines tractography through effective use of anatomical information. *NeuroImage*, 62(3):1924 – 1938.

Smith, R. E., Tournier, J.-D., Calamante, F., and Connelly, A. (2013). SIFT: Spherical-deconvolution informed filtering of tractograms. *NeuroImage*, 67:298 – 312.

Smith, R. E., Tournier, J. D., Calamante, F., and Connelly, A. (2015a). SIFT2: Enabling dense quantitative assessment of brain white matter connectivity using streamlines tractography. *NeuroImage*, 119:338–351.

Smith, R. E., Tournier, J.-D., Calamante, F., and Connelly, A. (2015b). The effects of SIFT on the reproducibility and biological accuracy of the structural connectome. *NeuroImage*, 104:253 – 265.

Sotiropoulos, S. N. and Zalesky, A. (2019). Building connectomes using diffusion MRI: why, how and but. *NMR in Biomedicine*, 32(4):e3752. e3752 NBM-16-0139.R1.

Sporns, O., Tononi, G., and Kötter, R. (2005). The Human Connectome: A Structural Description of the Human Brain. *PLOS Computational Biology*, 1(4).

Stejskal, E. O. and Tanner, J. E. (1965). Spin Diffusion Measurements: Spin Echoes in the Presence of a Time-Dependent Field Gradient. *The Journal of Chemical Physics*, 42(1):288–292.

Szafer, A., Zhong, J., and Gore, J. C. (1995). Theoretical model for water diffusion in tissues. *Magnetic Resonance in Medicine*, 33(5):697–712.

Szczepankiewicz, F., Lasič, S., van Westen, D., Sundgren, P. C., Englund, E., Westin, C.-F., Ståhlberg, F., Lätt, J., Topgaard, D., and Nilsson, M. (2015). Quantification of microscopic diffusion anisotropy disentangles effects of orientation dispersion from microstructure: Applications in healthy volunteers and in brain tumors. *NeuroImage*, 104:241–252.

Szczepankiewicz, F., van Westen, D., Englund, E., Westin, C.-F., Ståhlberg, F., Lätt, J., Sundgren, P. C., and Nilsson, M. (2016). The link between diffusion mri and tumor heterogeneity: Mapping cell eccentricity and density by diffusional variance decomposition (divide). *NeuroImage*, 142:522–532.

Telesford, Q. K., Simpson, S. L., Burdette, J. H., Hayasaka, S., and Laurienti, P. J. (2011). The brain as a complex system: using network science as a tool for understanding the brain. *Brain connectivity*, 1(4):295–308. 22432419[pmid].

Thomas, C., Ye, F. Q., Irfanoglu, M. O., Modi, P., Saleem, K. S., Leopold, D. A., and Pierpaoli, C. (2014). Anatomical accuracy of brain connections derived from diffusion MRI tractography is inherently limited. *Proceedings of the National Academy of Sciences*, 111(46):16574–16579.

Tibshirani, R. (1996). Regression Shrinkage and Selection via the Lasso. *Journal of the Royal Statistical Society. Series B (Methodological)*, 58(1):267–88.

Tompa, R. (2019). 5 unsolved mysteries about the brain. [Online]. Available from: `https://alleninstitute.org/what-we-do/brain-science/news-press/articles/5-unsolved-mysteries-about-brain`. Allen Institute for Brain Science; accessed 05/02/2021.

Tournier, J.-D., Calamante, F., and Connelly, A. (2007). Robust determination of the fibre orientation distribution in diffusion MRI: Non-negativity constrained super-resolved spherical deconvolution. *NeuroImage*, 35(4):1459 – 1472.

Tournier, J.-D., Calamante, F., and Connelly, A. (2010). Improved probabilistic streamlines tractography by 2nd order integration over fibre orientation distributions. volume 18.

Tournier, J.-D., Calamante, F., and Connelly, A. (2012). MRtrix: Diffusion Tractography in Crossing Fiber Regions. *Int. J. Imaging Syst. Technol.*, 22(1):53–66.

Tournier, J.-D., Calamante, F., Gadian, D. G., and Connelly, A. (2004). Direct estimation of the fiber orientation density function from diffusion-weighted MRI data using spherical deconvolution. *NeuroImage*, 23(3):1176 – 1185.

Tournier, J.-D., Mori, S., and Leemans, A. (2011). Diffusion tensor imaging and beyond. *Magnetic resonance in medicine*, 65(6):1532–1556. 21469191[pmid].

Tournier, J.-D., Smith, R., Raffelt, D., Tabbara, R., Dhollander, T., Pietsch, M., Christiaens, D., Jeurissen, B., Yeh, C.-H., and Connelly, A. (2019). MRtrix3: A fast, flexible and open software framework for medical image processing and visualisation. *NeuroImage*, 202:116137.

Tsai, L. L., Grant, A. K., Mortele, K. J., Kung, J. W., and Smith, M. P. (2015). A practical guide to mr imaging safety: What radiologists need to know. *RadioGraphics*, 35(6):1722–1737.

Tuch, D. S. (2004). Q-ball imaging. *Magnetic Resonance in Medicine*, 52(6):1358–1372.

Tuch, D. S., Reese, T. G., Wiegell, M. R., Makris, N., Belliveau, J. W., and Wedeen, V. J. (2002). High angular resolution diffusion imaging reveals intravoxel white matter fiber heterogeneity. *Magnetic Resonance in Medicine*, 48(4):577–582.

Udin, S. B. and Fawcett, J. W. (1988). Formation of topographic maps. *Annual Review of Neuroscience*, 11(1):289–327. PMID: 3284443.

Valk, S. L., Di Martino, A., Milham, M. P., and Bernhardt, B. C. (2015). Multicenter mapping of structural network alterations in autism. *Human Brain Mapping*, 36(6):2364–2373.

van den Berg, E. and Friedlander, M. P. (2008). Probing the pareto frontier for basis pursuit solutions. *SIAM J. Sci. Comput.*, 31(2):890–912.

van den Heuvel, M. P., de Reus, M. A., Feldman Barrett, L., Scholtens, L. H., Coopmans, F. M. T., Schmidt, R., Preuss, T. M., Rilling, J. K., and Li, L. (2015). Comparison of diffusion tractography and tract-tracing measures of connectivity strength in rhesus macaque connectome. *Human Brain Mapping*, 36(8):3064–3075.

Veraart, J., Nunes, D., Rudrapatna, U., Fieremans, E., Jones, D. K., Novikov, D. S., and Shemesh, N. (2020). Noninvasive quantification of axon radii using diffusion mri. *eLife*, 9:e49855.

Veraart, J., Sijbers, J., Sunaert, S., Leemans, A., and Jeurissen, B. (2013). Weighted linear least squares estimation of diffusion MRI parameters: Strengths, limitations, and pitfalls. *NeuroImage*, 81:335–346.

von dem Hagen, E. A. and Henkelman, R. M. (2002). Orientational diffusion reflects fiber structure within a voxel. *Magnetic Resonance in Medicine*, 48(3):454–459.

Vázquez, A., López-López, N., Sánchez, A., Houenou, J., Poupon, C., Mangin, J.-F., Hernández, C., and Guevara, P. (2020). Ffclust: Fast fiber clustering for large tractography datasets for a detailed study of brain connectivity. *NeuroImage*, 220:117070.

Wang, H. and Leng, C. (2008). A note on adaptive group Lasso. *Computational Statistics and Data Analysis*, pages 5277–5286.

Weishaupt, D., Köchli, V. D., and Marincek, B. (2006). *How does MRI work?* Springer-Verlag Berlin Heidelberg, second edition.

Wende, T., Hoffmann, K.-T., and Meixensberger, J. (14.08.2020). Tractography in neurosurgery: A systematic review of current applications. *J Neurol Surg A Cent Eur Neurosurg*, 81(05):442–455. 442.

Wickens, A. P. (2014). *A History of the Brain: From Stone Age surgery to modern neuroscience*. Psychology Press.

Wycoco, V., Shroff, M., Sudhakar, S., and Lee, W. (2013). White matter anatomy: What the radiologist needs to know. *Neuroimaging Clinics of North America*, 23(2):197–216. Pediatric Demyelinating Disease and its Mimics.

Yeatman, J. D., Dougherty, R. F., Myall, N. J., Wandell, B. A., and Feldman, H. M. (2012). Tract Profiles of White Matter Properties: Automating Fiber-Tract Quantification. *PLOS ONE*, 7(11):1–15.

Yeh, C.-H., Jones, D. K., Liang, X., Descoteaux, M., and Connelly, A. (2020). Mapping Structural Connectivity Using Diffusion MRI: Challenges and Opportunities. *Journal of Magnetic Resonance Imaging*, n/a(n/a).

Yuan, M. and Lin, Y. (2006). Model selection and estimation in regression with grouped variables. *Journal of the Royal Statistical Society: Series B (Statistical Methodology)*, 68(1):49–67.

Zalesky, A., Fornito, A., Cocchi, L., Gollo, L. L., van den Heuvel, M. P., and Breakspear, M. (2016). Connectome sensitivity or specificity: which is more important? *NeuroImage*, 142:407 – 420.

Zhang, H., Schneider, T., Wheeler-Kingshott, C. A., and Alexander, D. C. (2012). NODDI: Practical in vivo neurite orientation dispersion and density imaging of the human brain. *NeuroImage*, 61(4):1000 – 1016.

Zhang, Y., Brady, M., and Smith, S. (2001). Segmentation of brain MR images through a hidden Markov random field model and the expectation-maximization algorithm. *IEEE Transactions on Medical Imaging*, 20(1):45–57.

Zhao, P., Rocha, G., and Yu, B. (2009). The composite absolute penalties family for grouped and hierarchical variable selection. *Ann. Statist.*, 37(6A):3468–3497.